Numerical Prediction of Ship Manoeuvring Performance in Waves

vorgelegt von
M. Sc.
Sebastian Alexander Uharek

Von der Fakultät V - Verkehrs- und Maschinensysteme
der Technischen Universität Berlin
zur Erlangung des akademischen Grades

Doktor der Ingenieurwissenschaften
- Dr.-Ing. -

genehmigte Dissertation

Promotionsausschuss:

Vorsitzender:	Prof. Dr.-Ing. Gerd Holbach
Gutachter:	Prof. Dr.-Ing. Andrés Cura Hochbaum
Gutachter:	Prof. Dr. Hironori Yasukawa

Tag der wissenschaftlichen Aussprache: 29.03.2019

Berlin 2019

Acknowledgement

I would like to express my gratitude to all the people without whom this work would not have been possible. First of all, I would like to thank Prof. Andrés Cura Hochbaum for his professional and personal support and encouragement throughout the last years. His guidance and inspiration contributed greatly to my academic development. Also, I would like to thank Prof. Hironori Yasukawa, not only for being my second supervisor but also for the helpful comments I received from him during the last years as well as for providing the experimental data for the validation. I am also grateful to Prof. Gerd Holbach for being the chairman of the doctoral committee.

Further, I would like to express my thanks to all my colleagues of the department Dynamics of Maritime Systems for their support, fruitful discussions and the pleasant time I had as a research assistant at the Technical University Berlin. In particular, I would like to mention Lars Koopmann, Jan Löhrmann and Friederike Reisch for their input regarding not only numerical and manoeuvring related questions, Antonio Lengwinat for performing the experiments in the research project PERSEE, which allowed the validation and improvement of the numerical computations and Kornelia Tietze for the administrative support and her bright and sunny spirit.

I would like to thank my friends and family for their support and the encouragement I received from them to finish this work. Especially, I would like to mention Bernd Peukert and Nicolas Häberle for the many inspiring discussions, which extended beyond the scope of this work.

Abstract

This thesis presents a method to predict rudder manoeuvres of ships in waves, which is purely based on numerical simulations. For this purpose, a mathematical model of Abkowitz type has been expanded to take the forces and moments due to waves into account. Under the assumption that oscillating wave forces and moments of first order do not influence the trajectory of the manoeuvring ship, only mean wave forces and moments are considered here. The coefficients of this extended mathematical model are determined by Reynolds-averaged Navier-Stokes (RANS) simulations of virtual captive model tests in calm water and waves. In order to get an estimation of the required mean power during the manoeuvre, the propeller torque is modelled as well.

This method has been applied to the S175 container ship and the results were compared to experimental measurements performed by Yasukawa and Nakayama (2009). The RANS simulations are performed with the in-house finite volume code Neptuno, which uses the SIMPLE method for pressure-velocity coupling, the standard k-ω turbulence model and a two-phase level set method. The effect of the propeller on the flow was captured using a body force model, which is based on RANS simulations performed in advance.

The effect of non-hydrodynamic mean inertial forces was investigated during the evaluation of the numerical captive model tests for the determination of the mean wave forces and moments. It was shown that it is crucial to consider these non-hydrodynamic forces when comparing results from numerical simulations and experimental measurements. Further, the influence of forward speed, drift angle, wave amplitude and moment of inertia about the transverse axis on the mean forces and moments was numerically investigated.

To validate the method, turning circle tests in calm water and waves have been simulated and compared to the experimental measurements. In general a good agreement was achieved for trajectories and mean added power. Three different starting conditions were compared for one manoeuvre, namely starting all manoeuvres with the same propeller revolution rate as in calm water, the same forward speed as in calm water or the same power as in calm water. It was shown, that for the development of rules regarding the minimum required power for manoeuvring in waves the starting condition plays an important role and the times t_{90} and t_{180} might be a more valuable indicator for manoeuvrability than the advance or tactical diameter.

Zusammenfassung

Diese Dissertation präsentiert eine rein numerische Methode zur Vorhersage von Rudermanövern von Schiffen in Wellen. Hierfür wurde ein Abkowitz-Modell um die Berücksichtigung der von den Wellen induzierten Kräfte und Momente erweitert. Unter der Annahme, dass die oszillierenden Wellenkräfte und -momente erster Ordnung keinen Einfluss auf die Trajetorie des manövrierenden Schiffes haben, wurden nur die mittleren Wellenkräfte und -momente im Modell berücksichtigt. Die Koeffizienten dieses erweiterten mathematischen Modells wurden mit Hilfe von Reynolds-averaged Navier-Stokes (RANS) Simulationen von virtuellen gefesselten Modellversuchen in Glattwasser und Wellen bestimmt. Zur Prognose der erforderlichen mittleren Zusatzleistung während des Manövers wurde das Propellerdrehmoment ebenfalls modelliert.

Das Verfahren wurde am Beispiel des S175 Containerschiffes angewandt und die Ergebnisse mit Messungen von Yasukawa und Nakayama (2009) verglichen. Die RANS-Simulationen wurden mit dem Finite-Volumen-Code Neptuno durchgeführt, welcher das SIMPLE-Verfahren für die Druck-Geschwindigkeitskopplung, das Standard k-ω Turbulenzmodell und eine zweiphasige Level-Set-Methode verwendet. Der Einfluss des Propellers auf die Strömung wurde mit einem Bodyforcemodell approximiert, welches auf im Vorfeld durchgeführten RANS-Simulationen basiert.

Bei der Auswertung der numerischen gefesselten Modellversuche zur Bestimmung der mittleren Wellenkräfte und -momente wurde der Effekt der nicht hydrodynamischen mittleren Trägheitskräfte untersucht. Es konnte gezeigt werden, dass für einen Vergleich von numerischen Simulationen und Messungen die Berücksichtigung dieser Trägheitskräfte essentiell ist. Darüber hinaus wurden der Einfluss der Vorausgeschwindigkeit, des Driftwinkels, der Wellenamplitude und des Trägheitsmomentes entlang der Querachse auf die mittleren Wellenkräfte und -momente numerisch untersucht.

Zur Validierung der Methode wurden Drehkreisversuche in Glattwasser und Wellen simuliert und mit Messungen verglichen. In den meisten Fällen wurde eine gute Übereinstimmung der Trajektorie des Schiffes und der mittleren Zusatzleistung erzielt. Darüber hinaus wurden Manöver mit drei unterschiedlichen Startbedingungen – gleiche Drehzahl, Geschwindigkeit oder Leistung wie im Glattwasser – durchgeführt. Es konnte gezeigt werden, dass die Startbedingung für die Entwicklung von Regeln bezüglich der erforderlichen Mindestleistung zum Manövrieren in Wellen eine sehr große Rolle spielt und die Zeiten t_{90} und t_{180} ein besseres Maß zur Beurteilung der Manövrierfähigkeit darstellen könnten als beispielsweise der Vorausweg oder taktische Durchmesser.

Contents

List of Figures

List of Tables

1. Introduction

1.1. Motivation

The prediction of ship motions has been an important field of ship hydrodynamic research for over 100 years. Traditionally, ship motions are split into two classes: manoeuvring and seakeeping. Manoeuvring describes ship motions initiated for example by the rudder, propeller or other control surfaces, whereas seakeeping is the motion behaviour of the ship in waves. During most of the 20th century, these two fields were investigated separately. The first paper on the prediction of ship manoeuvres in waves known to the author was published by Hirano et al. (1980). In recent years – supported by the International Maritime Organisation (IMO) lead discussion on minimum power requirements in waves – the increased number of publications on this subject shows the increasing interest in this field. Due to the growing computational capabilities of modern computer systems, it seems preferable to develop a prediction method solely based on numerical simulations and not depending on expensive and time consuming experimental model tests. In the following sections, an overview of the current state of prediction methods for motions of ships in waves and mean wave forces is presented.

1.2. State of the art

The following section is partially based on the literature reviews done by Hutchison (1990), Tello Ruiz et al. (2012) and Skejic (2013) and gives a rather brief, non exhaustive overview on different prediction methods for ship motions in waves and for manoeuvring.

1.2.1. Seakeeping prediction

According to Saunders (1965) and Hutchison (1990), pioneering work in the field of seakeeping was initiated by John Scott Russell in 1830, followed by contributions from William Froude in 1861 and A. N. Krylov in 1896, who performed analytic studies to describe the motions of a ship in waves. Around the beginning of the 20th century, wavemakers were installed in ship model basins to experimentally measure the forces acting on fixed ships and the motion behaviour of free sailing ship models in a controlled environment. One of the first experimental investigation of the longitudinal mean wave force – or added resistance – was done by Fujii and

Takahashi (1975). They performed experimental measurements and numerical predictions of the added resistance in waves for different wave encounter angles.

Yasukawa and Adnan (2006) and Yasukawa et al. (2010) performed experiments with the S175 container ship in head an beam waves combined with oblique inflow conditions. In this experiments a sub carriage with nested slides has been attached to the main carriage. These slides are weakly coupled to the sub carriage using springs. On the ship three load cells are installed, which are connected to the slides via guide rods, see Figure 1.1. This allows the ship to freely heave, pitch and roll, while the mean surge, sway and yaw motion is weakly prescribed by the springs.

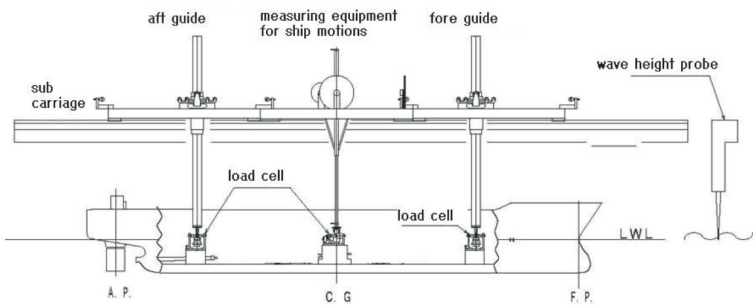

Figure 1.1.: Experimental setup from Yasukawa and Adnan (2006)

More recently in the scope of the German research project PERSEE and the European research project SHOPERA, the resistance and power increase in waves were measured for different ship types. For this purpose, special measurement devices were constructed at the Hamburg Ship Model Basin (HSVA) and the Technical University Berlin (TUB), see Valanto and Hong (2015) and Lengwinat and Cura Hochbaum (2018).

In addition to experimental measurements of the ship motions and mean wave forces, numerous tools for the prediction of such motions and forces were developed in the last century. They can be separated into four different categories, sorted by increasing complexity:

Empirical formulas are based on theoretical assumptions and observations and can be applied quickly in an early stage of design. Examples of formulas for added resistance and their application can be found for example in Gerritsma and Beukelmann (1972) and Liu and Papanikolaou (2016). The application of such formulas is limited to similar shaped hulls and even though they are a very good tool for the initial design stage, their accuracy is usually limited.

Potential flow theory may be employed if the flow is assumed to be irrotational, which is a good assumption for inviscid flows. In this case, the velocity field can be

described as the spatial gradient of a scalar field called velocity potential. Together with the assumption of an incompressible fluid, the continuity equation gets reduced to the Laplace equation, for which – due to its linearity – the superposition principle can be applied, e.g. Faltinsen (1990).

The strip method developed by Korvin-Kroukovski and Jacobs (1957) is based on the assumption that for ship motions of higher frequency, where dynamic effects are of interest, waves are mostly propagated in the transversal direction, allowing to split the three dimensional problem into multiple two dimensional problems, e.g. Söding (1982). This drastically simplifies computations, since the each section of the ship may be treated as independent from the others. The first solutions for the two dimensional potential flow problem of an oscillating circular or ship section were published by Ursell (1948); Grim (1953). This method is also quite fast, but limited to slender bodies with no rapid changes in their sectional contours. Also due to the linearised Bernoulli equation, no mean forces can be computed without further assumptions. Boese (1970) has developed a method to estimate the mean longitudinal wave force (or added resistance) based on the linearised ship motions.

For the computation of the three dimensional potential flow around a ship, boundary element methods (BEMs) are used, which are based on a panel discretisation of the ship hull and free water surface. BEMs can be split into two classes: time domain and frequency domain methods.

For the computations in time domain, impulse response functions are used to compute the ship motions in time, see Cummins (1962). An example application of a 3D time domain panel method can be found in Yasukawa (2002), where the method was applied to compute the motions of the S175 benchmark container ship.

In contrast to time domain computations, frequency domain computations are based on translating sources of pulsating strength. Green functions are used to implement the boundary conditions into the Laplace equation. Chang (1977) was one of the first to use the BEM for the computation of the three dimensional flow around a ship in the frequency-domain (Noblesse and Hendrix, 1992). Other examples for numerical methods using this approach are Newdrift (Papanikolaou and Zaraphonitis, 2001) and WAMIT (WAMIT, 2016).

Alternatively to Green functions, Rankine sources may be employed to satisfy the boundary conditions of the Laplace equation and the first application known to the author was by Bai and Yeung (1974) to oscillating ship sections. Another example is the work by Yasukawa (1990), who applied this method to compute the hydrodynamic forces acting on a ship hull. A current numerical tool that employs the Rankine source method is GLRankine, with the possibility to take the steady flow around the ship in calm water into account (Söding et al., 2012).

While linear potential flow methods in general yield rather accurate predictions for ship motions in long waves, no higher order wave forces can be directly computed due to the linearity of the method. To overcome this problem, either the near or far field method can be used.

In the near field method, the second order term in the Bernoulli equation is considered to determine the mean wave forces by direct pressure integration, Pinkster and van Oortmerssen (1977). The far field method presented by Maruo (1960, 1963), uses an integral over a far-field control surface and the conservation of energy to obtain the mean wave forces (Clauss et al., 1988; Amini Afshar, 2014).

Although both methods allow the computation of mean forces and moments in waves, the underlying method is still linear and a limited accuracy is to be expected. It should be noted that in short waves, e.g. shorter than half of the ship length, especially linear potential methods are not able to yield accurate results due to the increasing wave steepness and thus the increasing non-linearity of the problem. But even the fully non-linear solution of the potential flow problem does not consider the frictional contribution to the added resistance. Sigmund and el Moctar (2018) investigated the influence of the frictional resistance for four different ship types and reported a frictional added resistance of more than 15% of the total added resistance in very short waves.

Field methods The forces acting on a ship as well as the resulting motions can also be computed by solving the Reynolds-averaged Navier-Stokes (RANS) equations inside a computational domain surrounding the ship. This method has proven to yield good results even for short non-linear waves, in which the potential methods show poor results, and for the prediction of the mean wave forces. Example applications of this method can be found in Cura Hochbaum and Pierzynski (2005), Sigmund and el Moctar (2018) or Uharek and Cura Hochbaum (2018b).

1.2.2. Manoeuvring prediction

With regards to the prediction of ship manoeuvring, according to Saunders (1965), the Swedish naval architect F. H. de Chapman was the first to approach the manoeuvring problem using scientific methods in the 1760's by investigating the influence of point of application of the pressure force on the projected underwater body on the ships manoeuvring characteristics. Around the 1860's an era of experimental investigations of the manoeuvring capabilities of ships began (Saunders, 1965). During that time, mostly free running model tests were used to derive empirical formulas or to directly obtain the manoeuvring characteristics from the model tests.

A disadvantage of the identification of the manoeuvring characteristics from free running model tests is the needed size of the model basins. As an alternative,

a semi-analytical prediction method was developed by M. A. Abkowitz during his sabbatical leave at the Technical University of Denmark (Abkowitz, 1964). This method is based on a mathematical model with coefficients derived from captive model tests and allowed a deeper insight on the hydrodynamic phenomena involved in manoeuvring. Strøm-Tejsen and Chislett (1966) used a planar motion mechanism (PMM) to perform the required static and dynamic captive tests to determine the hydrodynamic coefficients of the ship. Smitt and Chislett (1974) showed a successful application of the coefficient based manoeuvring prediction method by the comparison of its results to full scale measurements.

In the scope of the *Sonderforschungsbereich 98* in Germany, the computerised planar motion carriage (CPMC) was installed at the HSVA, allowing for a thorough investigation of manoeuvring characteristics of different ships (Grim et al., 1976; Wolff, 1981). During that time the indirect system identification method for the prediction of manoeuvres was developed. The indirect system identification method (Oltmann, 1973, 1978) is based on free running model tests that are used to identify the manoeuvring characteristics. After the successful system identification, any rudder manoeuvre can be simulated. The method has been further refined and is still applied at the HSVA, Weede (2000).

There are three different kinds of numerical prediction methods for manoeuvring.

Empirical formulas are a rather simple approach to predict the manoeuvring capabilities in an early stage of design. Usually they are not capable of accurately predicting arbitrary rudder manoeuvres and are typically tuned for one application case, see Quadvlieg et al. (2018).

Methods based on mathematical modelling of external forces are more sophisticated and can be subdivided into system based and modular methods. The first approach considers the flow for all three components, namely the flow around the ship hull, propeller and rudder, together and the second considers each component individually and possibly add interaction terms later. A common example for the system based approach is the above mentioned mathematical model from Abkowitz (1964). The forces and moments acting on the whole system required to determine the hydrodynamic coefficients can be determined by means of captive model tests. Cura Hochbaum (2006) has shown, that these captive model tests can be replaced by virtual captive tests, which allow a determination of the required forces and moments with high accuracy.

A common example for the modular approach are the simulation models based on the Manoeuvring Model Group (MMG) model, which are especially common in Japan. The concept of this prediction method was proposed by the MMG research group of the Japanese Towing Tank Conference in 1977, but no detailed simulation model was included. Over the years, concrete simulation models were developed by

many researchers, see for example Matsumoto and Suemitsu (1980). Because many different simulation models developed from the original MMG method, Yasukawa and Yoshimura (2014) proposed the MMG standard method for manoeuvring prediction in order to ensure a common basic part for the models.

For each component different prediction methods exist. Hull forces can for example be determined by the slender body (potential) theory, e.g. Söding (1995). Although this method is quite fast, it is not possible to accurately predict the separation of the flow for a ship sailing at high drift angle. There are some suggestions for corrections (Schumann, 2017) and good results have been attained. However, due to the semi-empirical nature of this corrections and the need for RANS computations or experimental results to calibrate, this method cannot be seen as a purely potential flow prediction method. For the rudder and propeller forces potential theory can be used as well. However, methods based on the assumption of an irrotational and thus inviscid fluid lack the possibility of accurately predicting the wake field of the ship. As a consequence, the inflow to the propeller is not captured correctly and the wrong operating point leads to a significantly different rudder efficiency. Further problems are the detection of stall at the rudder. All three above mentioned force contributions can also be determined by viscous RANS computations with very high accuracy and moderate computational times as shown for example by Cura Hochbaum et al. (2008); Cura Hochbaum and Uharek (2014). Especially for oblique inflow conditions, where the wake field of the ship and thus the propeller inflow is influenced by the separation of the flow at the hull, RANS are superior to potential flow methods.

Time domain simulations are based on the computation of the forces acting on the ship hull, propeller and rudder, which are from here on referred to as components of the model, in each time step of the simulation for the given motion state. These simulations can also either be performed using a potential code or by RANS simulations as shown for example by Carrica and Stern (2008); Mofidi and Carrica (2014). el Moctar et al. (2014) showed the prediction of the required power for a manoeuvring ship using a RANS method.

There are two main approaches for the treatment of the forces required

Despite the variety of numerical prediction methods available, the results of the workshops on verification and validation of ship manoeuvring simulation methods (SIMMAN) held in 2008 and 2014 have shown, that in general the numerical prediction of ship motions is still challenging today.

1.2.3. Prediction of Manoeuvring in Waves

The Manoeuvring Committee (2014) splits wave manoeuvring prediction methods into four classes: experimental methods, unified methods, two-time-scale methods

and time domain RANS computations. A comprehensive list of current applications of these methods is provided in The Manoeuvring Committee (2017) and thus only a brief summary is included here.

Experimental investigations of ship manoeuvring characteristics in waves were performed by Ueno et al. (2003). They performed straight running, zigzag, turning circle and stopping tests for a VLCC at full and ballast condition. It was concluded that for the considered ship the speed loss is largest in head waves of the same length as the ship. Further they showed that during a turning circle in waves the ship is not shifted in the direction of the incoming wave, but the direction of the drift is turned relative to the direction of the incoming wave. Yasukawa (2006) has performed a series of turning circle tests for the S175 container ship, which is the most extensive validation campaign for ship manoeuvring in waves known to the author.

Two-time-scale methods split the problem into a prediction of high frequency motions mainly caused by the first order component of the hydrodynamic wave force and a low frequency component mainly due to the second order contributions of the wave force and the calm water manoeuvring motion. To the authors knowledge, they were first applied by Yasukawa (2006). The predicted traces are in good agreement with the measurements, except for short waves. The original paper is in Japanese, but the results were later published in English as well (Yasukawa and Nakayama, 2009), but no details on the prediction of the hydrodynamic forces were given there, since that paper is focused on the experiments.

Skejic and Faltinsen (2008) and Skejic and Faltinsen (2013) have also shown simulations of turning circle tests for the S175 container ship in regular and irregular waves. They approximated the global hydrodynamic hull forces using cross flow coefficients, which were tuned for the application case. For the propeller forces they used experimental data. The wave forces are obtained by a potential flow approach using direct pressure integration. The obtained results showed in general a good agreement.

Papanikolaou et al. (2016) predicted turning circles of the Duisburg test case (DTC) container ship. They used RANS computations to determine the calm water manoeuvring forces and potential flow theory for the wave forces.

Schoop-Zipfel (2016) also simulated turning circles in regular waves. He compared a two-time-scale approach using a slender body theory for the hull forces and potential theory (PDSTRIP) to obtain mean second order wave forces. Good predictions were obtained for most situations with the assumed horizontal drag coefficient for cross flow forces, but for some manoeuvres the simulations could not be finished.

Unified methods consider the total wave induced and manoeuvring forces and moments on the ship hull together. They use of impulse response functions to compute the wave induced forces and moments in time domain and add low frequency manoeuvring forces using ramp functions. Schoop-Zipfel (2016) has shown that for the unified theory tuning was necessary to obtain similar results as with the two-time-scale approach.

Time domain RANS simulations compute the hydrodynamic forces and moments acting on the ship hull in each timestep and thus consider wave forces and forces due to manoeuvring together. After the forces for the current time step are determined the motion equations are being solved and the boundary conditions and if necessary apparent forces are updated. The computations are very challenging and require a lot of resources.

1.3. Shortcomings of current approaches and objective of the thesis

As shown above, there are several methods for the numerical prediction of ship manoeuvres in waves. However, due to the lack of experimental data most of them are not thoroughly validated. Most prediction models are based on mean wave forces obtained from computations with a linear potential code, which usually shows a poor accuracy in short and steep waves. As shown in the SHOPERA international benchmark study (Shigunov et al., 2018), the current capabilities of the numerical prediction methods for manoeuvring in waves available at the current time are insufficient. Regarding the calm water coefficients, potential flow computations cannot be used to predict the separation point of the flow and are therefore useless without additional empirical assumptions. Although it is possible to compute the manoeuvres in waves using a RANS code, as demonstrated for example by Carrica et al. (2012); Zhang et al. (2017), the computational times are relatively high compared to potential code computations and therefore not suitable if a high number of manoeuvres needs to be predicted.

Therefore, a new approach is proposed in this work, which allows the prediction of rudder manoeuvres in arbitrary long crested harmonic waves. It uses a coefficient based approach for modelling the external hydrodynamic forces acting on the ship during the manoeuvre, which allows – after determination of these hydrodynamic coefficients – for a fast computation of the manoeuvres by time integration of the rigid body motion equations. The coefficients are determined by RANS simulations of captive model tests in calm water and in waves, but it would be also possible to obtain the coefficients by means of experiments. All computations in this thesis are performed with the in-house code Neptuno, Cura Hochbaum (1993), which has proven to yield very accurate results for diverse applications in the field of ship hydrodynamics. Since the coefficients are determined with RANS simulations rather than using a linear potential code, no empirical formulas nor

experiments are necessary to tune the prediction method to a specific application case. Further, it is shown that the mostly neglected non-hydrodynamic inertial forces which act on the moving ship may play a significant role when computing or measuring mean wave forces and moments. The proposed method also aims at predicting the required power during the manoeuvre. Since after the determination of the hydrodynamic coefficients, arbitrary rudder manoeuvres can be predicted in fractions of a second, the present method represents a more accurate but still practicable way for predicting manoeuvres in waves and for identifying critical manoeuvres with respect to the required power.

2. Method

The following chapter describes the chosen numerical approach to compute rudder manoeuvres in calm water and waves. The first section presents the rigid body dynamics and fundamental equations of motion. In the next section, the mathematical model of the external hydrodynamic forces and moments for calm water and waves is presented. For the sake of brevity, 'forces and moments' are just referred to as 'forces' from here on. The necessary hydrodynamic forces are computed using the in-house RANS code Neptuno. The governing equations and the numerical solution procedure is described. The procedure is then applied to the S175 container ship. The notation used in this work is the one proposed by DIN (1987). Whenever appropriate the index notation and the Einstein summation convention is used. In equations where the index notation is not used $x_1 = x$, $x_2 = y$, $x_3 = z$, $\xi_1 = \xi$, $\xi_2 = \eta$, $\xi_3 = \zeta$ and $u_1 = u$, $u_2 = v$, $u_3 = w$ holds.

2.1. Rigid body dynamics

This section defines the coordinate systems that are used in this work as well as the transformation relations between these systems. Further the equations of motion that are solved to predict the manoeuvres as well as the motion of the ship during the RANS simulations are presented.

2.1.1. Coordinate systems and transformations

For the description of the ship motions in six degrees of freedom, it is convenient to introduced three coordinate systems. The first coordinate system is the earth fixed coordinate system (inertial frame) with the Cartesian coordinates ξ, η, ζ (or ξ_i in case of index notation). Since the position vector of the centre of gravity and the moments of inertia are not given for this frame of reference, a ship fixed coordinate system with the Cartesian coordinate x, y, z (or x_i) is introduced. If the manoeuvres of a surface ship are described, it is convenient to introduce the hybrid coordinate system, which follows the ship motions except for roll, pitch and heave.

The origin of the ship fixed coordinate system (O) is defined midships at the centre plane on the design waterline with the earth fixed coordinates ξ_O, η_O and ζ_O (or ξ_i^O). The positive x-coordinate axis is directed towards the bow, the positive y-coordinate axis is directed to starboard and the positive z-coordinate axis is

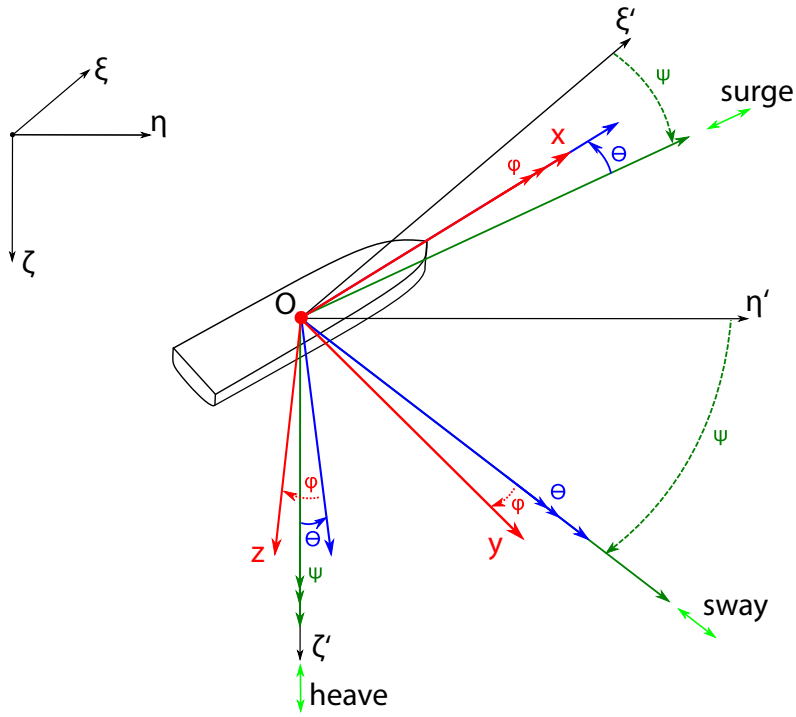

Figure 2.1.: Used coordinate systems

directed downwards, see Figure 2.1. The Euler angles φ (roll), θ (pitch) and ψ (yaw) are used to describe the rotation of the ship fixed coordinate system with respect to the earth fixed coordinate system. The angle φ is defined as a rotation about the ship fixed longitudinal axis, θ about the Eulerian line of nodes and ψ about the vertical axis of the earth fixed coordinate system shifted to the ships origin. It should be noted that one drawback of using Euler angles is the singularity at $\pm 90°$ pitch angle (gimbal lock), which however is very unlikely to occur when describing the motions of a surface ship.

The coordinates of an arbitrary point can be transformed between these coordinate systems using a transformation matrix:

$$\xi_i = \xi_i^O + T_{ij} x_j \tag{2.1}$$

T_{ij} are the elements of the transformation matrix T for the transformation between the earth fixed and ship fixed coordinate system and is defined as [1]:

[1] c_φ is short for $\cos(\varphi)$, $s_\varphi = \sin(\varphi)$

$$T = \begin{pmatrix} c_\psi c_\theta & -c_\varphi s_\psi + s_\varphi s_\theta c_\psi & s_\varphi s_\psi + c_\varphi s_\theta c_\psi \\ s_\psi c_\theta & c_\varphi c_\psi + s_\varphi s_\theta s_\psi & -s_\varphi c_\psi + c_\varphi s_\theta s_\psi \\ -s_\theta & s_\varphi c_\theta & c_\varphi c_\theta \end{pmatrix} \tag{2.2}$$

The transformation matrix T can also be used to transform vector components. The components ω_i of the angular velocity vector in the ship fixed coordinate system are:

$$\omega_1 = \dot{\varphi} - \dot{\psi} \sin\theta \tag{2.3}$$

$$\omega_2 = \dot{\psi} \cos\theta \sin\varphi + \dot{\theta} \cos\varphi \tag{2.4}$$

$$\omega_3 = \dot{\psi} \cos\theta \cos\varphi - \dot{\theta} \sin\varphi \tag{2.5}$$

The drift angle β of the ship is defined as:

$$\beta = \arctan\left(\frac{-v}{u}\right) \tag{2.6}$$

2.1.2. Motion equations

The second law of Newtons states that the total time derivative of the momentum of a body is equal to the sum of all external forces which act on it. Under the assumption that the ship is a rigid body with a constant mass m and x_i^G are the constant Cartesian components of the position vector of the centre of gravity in the ship fixed coordinate system, the motion equations read (Cura Hochbaum and Vogt, 2002):

$$m\left[\dot{u}_i + \epsilon_{ijk}\dot{\omega}_j x_k^G + \epsilon_{ijk}\omega_j u_k + \omega_i\omega_j x_j^G - x_i^G \omega_j \omega_j\right] = F_i \tag{2.7}$$

where ω_i are the ship fixed components of the angular velocity vector and $\dot{\omega}_i$ its time derivative, u_i the ship fixed Cartesian components of the velocity vector of the origin O and $\dot{u}_i$ its time derivative and F_i are the ship fixed components of the total external force. ϵ_{ijk} is the Levi-Civita symbol, which is 1 for an even permutation of ijk, -1 for an odd permutation of ijk and 0 otherwise.

The angular momentum equation in the ship fixed coordinate system reads (Cura Hochbaum and Vogt, 2002):

$$I_{ij}\dot{\omega}_j + \epsilon_{ijk}\omega_j I_{kl}\omega_l + m\left(\epsilon_{ijk} x_j^G \dot{u}_k + \omega_i x_j^G u_j - u_i x_j^G \omega_j\right) = M_i \tag{2.8}$$

where I_{ij} are the elements of the tensor of inertia and M_i are the components of the total external moment in the ship fixed coordinate system. If each component of (2.7) and (2.8) is written out, the motion equations in six degrees of freedom stated in the ship fixed coordinate system are:

$$
\begin{aligned}
&m\left[(\dot{u}+\omega_2\,w-\omega_3\,v)-x_G\left(\omega_2^2+\omega_3^2\right)-y_G\left(\dot{\omega}_3-\omega_1\omega_2\right)+z_G\left(\dot{\omega}_2+\omega_1\omega_3\right)\right]=F_x\\
&m\left[(\dot{v}-\omega_1\,w+\omega_3\,u)+x_G\left(\dot{\omega}_3+\omega_1\omega_2\right)-y_G\left(\omega_1^2+\omega_3^2\right)-z_G\left(\dot{\omega}_1-\omega_2\omega_3\right)\right]=F_y\\
&m\left[(\dot{w}+\omega_1\,v-\omega_2\,u)-x_G\left(\dot{\omega}_2-\omega_1\omega_3\right)+y_G\left(\dot{\omega}_1+\omega_2\omega_3\right)-z_G\left(\omega_1^2+\omega_2^2\right)\right]=F_z\\
&\qquad I_{xx}\dot{\omega}_1-\left(I_{yy}-I_{zz}\right)\omega_2\omega_3-I_{xy}\left(\dot{\omega}_2-\omega_1\omega_3\right)-I_{yz}\left(\omega_2^2-\omega_3^2\right)\\
&-I_{xz}\left(\dot{\omega}_3+\omega_1\omega_2\right)+m\left[y_G\left(\dot{w}+\omega_1 v-\omega_2 u\right)\right]-m\left[z_G\left(\dot{v}-\omega_1 w+\omega_3 u\right)\right]=M_x\\
&\qquad I_{yy}\dot{\omega}_2-\left(I_{zz}-I_{xx}\right)\omega_1\omega_3-I_{xy}\left(\dot{\omega}_1+\omega_2\omega_3\right)-I_{yz}\left(\dot{\omega}_3-\omega_1\omega_2\right)\\
&-I_{xz}\left(\omega_3^2-\omega_1^2\right)+m\left[z_G\left(\dot{u}+\omega_2 w-\omega_3 v\right)\right]-m\left[x_G\left(\dot{w}+\omega_1 v-\omega_2 u\right)\right]=M_y\\
&\qquad I_{zz}\dot{\omega}_3-\left(I_{xx}-I_{yy}\right)\omega_1\omega_2-I_{xy}\left(\omega_1^2-\omega_2^2\right)-I_{yz}\left(\dot{\omega}_2+\omega_1\omega_3\right)\\
&-I_{xz}\left(\dot{\omega}_1-\omega_2\omega_3\right)+m\left[x_G\left(\dot{v}-\omega_1 w+\omega_3 u\right)\right]-m\left[y_G\left(\dot{u}+\omega_2 w-\omega_3 v\right)\right]=M_z
\end{aligned}
\tag{2.9}
$$

For surface ships, it is common to reduce the problem to four degrees of freedom, since the heave and the pitch motion has only a negligible influence on the trajectory of a manoeuvring ship and the corresponding motions are small and thus not of interest in this case. Stated in the hybrid coordinate system for a ship with a symmetry at $y = 0$ they read:

$$
\begin{aligned}
&m\left[\dot{U}-\dot{\psi}V-x_G\dot{\psi}^2+z_G\left(2\dot{\psi}\dot{\varphi}\cos\varphi+\ddot{\psi}\sin\varphi\right)\right]=X\\
&m\left[\dot{V}+\dot{\psi}U+x_G\ddot{\psi}+z_G\left(\left(\dot{\psi}^2+\dot{\varphi}^2\right)\sin\varphi-\ddot{\varphi}\cos\varphi\right)\right]=Y\\
&I_{xx}\ddot{\varphi}-I_{xz}\ddot{\psi}\cos\varphi+\left(I_{zz}-I_{yy}\right)\dot{\psi}^2\sin\varphi\cos\varphi+\\
&\qquad -mz_G\cos\varphi\left(\dot{V}+U\dot{\psi}\right)=K\\
&\left(I_{yy}\sin^2\varphi+I_{zz}\cos^2\varphi\right)\ddot{\psi}+\\
&2\left(I_{yy}-I_{zz}\right)\dot{\psi}\dot{\varphi}\sin\varphi\cos\varphi-I_{xz}\left(\ddot{\varphi}\cos\varphi-\dot{\varphi}^2\sin\varphi\right)+\\
&mx_G\left(\dot{V}+U\dot{\psi}\right)+mz_G\sin\varphi\left(\dot{U}-V\dot{\psi}\right)=N
\end{aligned}
\tag{2.10}
$$

F_x, F_y, F_z, M_x, M_y and M_z in (2.9) are the external forces acting on the ship stated in the ship fixed coordinate system. Contrary, X, Y, K and N in (2.10) are the external forces stated in the hybrid coordinate system and U and V the hybrid components of the velocity vector of the ship. The forces contain the hydrodynamic forces acting on the hull F_H, the weight F_W and restoring forces F_R where applicable.

2.1.3. Modelling of restoring forces and moments for RANS simulations

In contrast to heave, pitch and roll motion, there are no hydrodynamic restoring forces for the surge, sway and yaw motion. Therefore external (restoring) forces are needed in order to enforce a desired average position, for instance at a certain mean encounter angle in oblique incoming waves. In the present case a linear restoring force (or retention force if applicable) F_R is added to the corresponding motion equations (2.9). This force models in the present application the effect of a spring system that was used in the experimental set up from Yasukawa and Adnan (2006) which is used for validation in this work, see Figure 2.2.

The total restoring force added to the right hand side of each motion equation are the sum of the contributions of each spring l:

$$F_i^R = \sum_l F_{i,l}^R \tag{2.11}$$

and the restoring moment with respect to the ships origin:

$$M_i^R = \sum_l \epsilon_{ijk} x_{j,l}^R F_{k,l}^R \tag{2.12}$$

Here $x_{i,l}^R$ are the three constant ship fixed coordinates of the application point of the force, which is also identical to the end point of the spring, and $F_{i,l}^R$ are the components of the force in the ship fixed coordinate system for each spring l. For the computation of these force components, it is necessary to know the coordinates of the point where the spring is attached. Since this point moves with the 'virtual towing carriage', it is convenient to introduce a new coordinate system attached to the 'virtual towing carriage', which is rotated relative to the earth fixed frame by the heading angle ψ_C, which is in general not identical to the ships heading. The origin C of this coordinate system with the earth fixed coordinates ξ_i^C moves with the constant carriage velocity u_i^C, which is expressed in the carriage fixed coordinate system:

$$\xi_i^C = T_{ij}^C u_j^C t \tag{2.13}$$

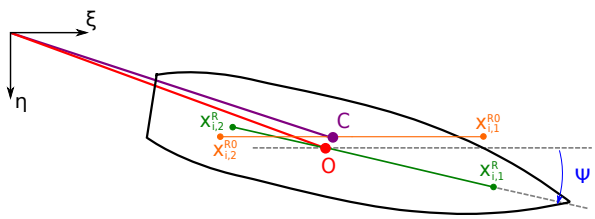

Figure 2.2.: Numerical spring system

For straight towing the only non-zero component of the carriage velocity is u_1^C, for oblique towing both u_1^C and u_2^C are chosen different to zero. T_{ij}^C are the components of the transformation matrix T_C between earth fixed coordinates and carriage fixed coordinates:

$$T_C = \begin{pmatrix} \cos(\psi_C) & -\sin(\psi_C) & 0 \\ \sin(\psi_C) & \cos(\psi_C) & 0 \\ 0 & 0 & 1 \end{pmatrix} \tag{2.14}$$

The earth fixed coordinates of the springs endpoint at rest $\xi_{i,l}^{R0}$ can be computed for each spring from its given (constant) ship fixed coordinates $x_{i,l}^R$ using the transformation matrix T of the carriage (2.2) at the time $t = 0\,\mathrm{s}$ and by adding the carriage motion:

$$\xi_{i,l}^{R0} = \xi_i^C + T_{ij}^C(t=0)\, x_{j,l}^R \tag{2.15}$$

The earth fixed coordinates of the current position ξ_l^R of the spring l is computed using the transformation matrix at the current time and adding the ship position:

$$\xi_l^R = \xi_i^O + T_{ij} x_{j,l}^R \tag{2.16}$$

Thus, the carriage fixed components of the 'virtual elongation vector' of the spring l can be computed:

$$\left(T_C^{-1}\right)_{mn} \left(\xi_{n,l}^R - \xi_{n,l}^{R0}\right) \tag{2.17}$$

Assuming that the springs are aligned with the coordinate axes of the virtual carriage, each components of this vector can be multiplied with the restoring component for the corresponding direction:

$$c_{km,l}^R \left(T_C^{-1}\right)_{mn} \left(\xi_{n,l}^R - \xi_{n,l}^{R0}\right) \tag{2.18}$$

where c_{ij}^R are the components of the restoring coefficient matrix c_R stated in the carriage fixed coordinate system for each spring l:

$$c_R = \begin{pmatrix} c_{x,l} & 0 & 0 \\ 0 & c_{y,l} & 0 \\ 0 & 0 & 0 \end{pmatrix} \tag{2.19}$$

This yields the components of the restoring forces in the carriage fixed coordinate system, which can then be converted back to the ship fixed coordinates: The resulting spring force is computed from the :

$$F_{i,l}^{R} = -\left(T^{-1}\right)_{ij} T_{jk}^{C} c_{km,l}^{R} \left(T_{C}^{-1}\right)_{mn} \left(\xi_{n,l}^{R} - \xi_{n,l}^{R0}\right) \tag{2.20}$$

2.2. Modelling of hydrodynamic external forces and moments for manoeuvring prediction

In order to predict rudder manoeuvres of a ship in waves, the hydrodynamic forces which act on the ship hull are needed to be known. Although it would be possible to use a viscous flow solver to directly simulate a manoeuvre by computing these forces in every new time step of the numerical simulation, such simulations are rather time consuming due to the fact, that for each manoeuvre an unsteady RANS computation has to be performed. To allow for a quick simulation of ship manoeuvres in waves and in calm water, the forces are approximated by a mathematical model. As a consequence the motion equations (2.10) can be solved by an explicit Euler time integration with negligible computational time.

The calm water manoeuvring model used for the whole system including hull, rudder and propeller forces is of Abkowitz type and has proven to yield very satisfactory results (Abkowitz (1964); Cura Hochbaum et al. (2008); Cura Hochbaum and Uharek (2014)). This model uses hydrodynamic coefficients depending on the change in longitudinal velocity Δu, sway velocity v, yaw rate r, rudder angle δ. The model includes terms up to third order in individual parameters and additional coupling terms to account for interactions between these parameters.

For the simulation of manoeuvres in waves, an approach based on the two-time-scale theory as presented in Skejic and Faltinsen (2008) is used. This approach is based on the assumption, that hydrodynamic forces as well as the resulting motions can be separated into a rapidly varying and a slowly varying contribution.

If the encounter frequency of the incoming wave is high and the ship is only turning with a moderate yaw rate, it has several encounters with the same wave. Due to the high inertia of the ship, the motions due to first order wave forces are relatively small and have only a negligible effect on the resulting trajectories. Thus they can be disregarded for the prediction of manoeuvres, resulting in a quasi-static situation.

This allows to compute the manoeuvres by including only the mean wave forces on the right hand side of the motion equations. Thus, in the present application, only the slowly varying component of the two-time-scale approach is considered.

2.2.1. Calm water case

The model used for the calm water coefficients in this work is thoroughly described in Abkowitz (1964) and will only be briefly recalled in the following section.

To model the hull, rudder and propeller forces in calm water, an equilibrium condition of a ship at constant forward speed u_0 with a fixed propeller revolution rate n is considered. For the current application, the revolution rate at the equilibrium condition is chosen at the model self propulsion point (MSPP), where the propeller thrust balances the longitudinal force acting on the ships hull and appendages. All motion parameters are defined as a deviation from the equilibrium situation, with the values at the equilibrium denoted by the subscript 0:

$$\Delta u = u - u_0 \quad ; \quad \Delta v = v - v_0 \quad ; \quad \Delta r = r - r_0 \tag{2.21}$$

The forces are then approximated with a Taylor series at this equilibrium point:

$$X(0, \Delta u, \Delta v, \Delta r, \ldots) = X_0 + \left(\frac{\partial X}{\partial u}\right)_0 \Delta u + \left(\frac{\partial X}{\partial v}\right)_0 \Delta v + \left(\frac{\partial X}{\partial r}\right)_0 \Delta r + \ldots \tag{2.22}$$

Writing the derivative of a function X taken at the equilibrium situation by using a subscript and by omitting the Δ, the following formulation is obtained:

$$X(u, v, r, \ldots) = X_0 + X_u u + X_v v + X_r r + \ldots + X_{uu} u^2 + X_{uuu} u^3 + \ldots \tag{2.23}$$

The derivatives $X_u, X_v, \ldots$ are called hydrodynamic coefficients. It should be noted that $v_0 = r_0 = 0$ and thus $\Delta v = v$ and $\Delta r = r$, but $u_0 \neq 0$ and thus the velocity u in (2.23) needs to be considered as a deviation from the initial condition u_0. The modelling of the side force, roll and yaw moments are performed in a similar fashion.

Since the hull forces during a rudder manoeuvre are almost proportional to the current longitudinal speed u squared, the influence of the hull-speed on these forces is modelled implicitly by making the forces and thus the corresponding hydrodynamic coefficients non-dimensional with u^2. Thus the coefficients depending on v, r, $\dot{v}$, $\dot{r}$ and combinations of those only need to be determined at one velocity, whereas for the rudder dependent coefficients, coupling terms with u exist. It is important to note, that the forces are made non-dimensional with the current longitudinal velocity u of the ship and not the one at the equilibrium condition u_0:

$$X' = \frac{X}{\frac{\rho}{2} L_{PP}^2 u^2} \quad Y' = \frac{Y}{\frac{\rho}{2} L_{PP}^2 u^2} \quad K' = \frac{K}{\frac{\rho}{2} L_{PP}^3 u^2} \quad N' = \frac{N}{\frac{\rho}{2} L_{PP}^3 u^2} \tag{2.24}$$

The hydrodynamic coefficients are often determined using captive model tests, during which the motion of the ship (and the deflection of its rudder) is prescribed and the

resulting global hydrodynamic forces are measured. Examples for such model tests are given by Grim et al. (1976) and Wolff (1981). Cura Hochbaum (2006) has shown that such model tests can be replaced by viscous flow simulations, so called virtual CPMC (or PMM) tests. These tests include static and dynamic variation of all relevant parameters (δ, Δu, v, r, $\Delta\dot{u}$, $\dot{v}$, $\dot{r}$).

The dynamic tests considered in this work are the so called pure surge (u), pure sway (v), pure yaw (r) and combined sway/yaw (v/r) tests. The harmonic motions are prescribed using sine and cosine functions to allow for arbitrary phase shifts for combined sway-yaw motions:

$$u = u_0 + \hat{u}\cos(\omega t) \tag{2.25}$$
$$v = \hat{v}_1\cos(\omega t) + \hat{v}_2\sin(\omega t) \tag{2.26}$$
$$r = \hat{r}_1\cos(\omega t) + \hat{r}_2\sin(\omega t) \tag{2.27}$$
$$\tag{2.28}$$

The choice of the motion period T_P with the respective frequency $\omega = \frac{2\pi}{T_P}$ and amplitudes $(\hat{u}, \hat{v}_1, \hat{v}_2, \hat{r}_1, \hat{r}_2)$ depends on the application case.

After all hydrodynamic forces have been obtained, the corresponding hydrodynamic coefficients are determined by solving the linear equation system:

$$A_{ij}x_j = q_i \tag{2.29}$$

where x_i are the unknown hydrodynamic coefficients, q_i are the forces for static and Fourier coefficients for dynamic tests and A_{ij} are the elements of the system matrix A.

In the following, the evaluation of the dynamic tests is explained for the pure sway test. All other tests are evaluated in the same way. In the pure sway test, the only non zero coefficients of the side force Y for a completely symmetric ship are:

$$Y_0 + Y_{\dot{v}}\dot{v}(t) + Y_v v(t) + Y_{vvv}v(t)^3 = Y(t) \tag{2.30}$$

A Fourier transformation is applied to the time trace of the obtained side force $Y(t)$, by which the Fourier coefficients a_i and b_i are obtained. The following formulation is obtained after substitution of the corresponding motion functions for $v(t)$ and $\dot{v}(t)$:

$$\begin{aligned} &Y_0 + Y_{\dot{v}}\left(-\hat{v}_1\omega\sin(\omega t) + \hat{v}_2\omega\cos(\omega t)\right) + Y_v\left(\hat{v}_1\cos(\omega t) + \hat{v}_2\sin(\omega t)\right) \\ &+Y_{vvv}\left(\hat{v}_1\cos(\omega t) + \hat{v}_2\sin(\omega t)\right)^3 = a_0 + \sum_i a_i\cos(i\omega t) + b_i\sin(i\omega t) \end{aligned} \tag{2.31}$$

This allows the determination of the entries A_{ij} for each Fourier coefficient a_i and b_i by comparison of the unknown left hand side and known right hand side coefficients:

$$\begin{aligned} Y_0 &+ \left(-\hat{v}_1\omega Y_{\dot{v}} + \hat{v}_2 Y_v + \frac{3}{4}\left(\hat{v}_2^3 + \hat{v}_1^2\hat{v}_2\right) Y_{vvv}\right)\sin(\omega t) \\ &+ \left(\hat{v}_2\omega Y_{\dot{v}} + \hat{v}_1 Y_v + \frac{3}{4}\left(\hat{v}_1^3 + \hat{v}_1\hat{v}_2^2\right) Y_{vvv}\right)\cos(\omega t) \\ &+ \left(\frac{\hat{v}_1^3 - 3\hat{v}_1\hat{v}_2^2}{4} Y_{vvv}\right)\cos(3\omega t) + \left(\frac{3\hat{v}_1^2\hat{v}_2 - \hat{v}_2^3}{4} Y_{vvv}\right)\sin(3\omega t) \\ &= a_0 + a_1\cos(\omega t) + b_1\sin(\omega t) + a_3\cos(3\omega t) + b_3\sin(3\omega t) \end{aligned} \tag{2.32}$$

An analogous analysis is carried out for the pure surge, pure yaw and combined sway/yaw tests. For the static tests the motion parameters are directly inserted into A and the corresponding forces are added on the right hand side. Solving this single system of equations for each force and moment allows to determine all needed hydrodynamic coefficients at once.

In order to determine the required power during a manoeuvre, the propeller torque is modelled as well. The mathematical model for the propeller torque is identical to the one used for the calm water forces, see Equation (2.23) and for the current case Table 3.1.

After determination of the coefficient set, a check of the mathematical model is performed by reconstructing the traces of all forces and comparing the modelled and the calculated values. Since the error is expressed relative to the computed value of forces or moments, only cases where the value differs significantly from zero are considered in the evaluation. For this purpose, the following limits were chosen for the current case: $|F_x| > 0.2\,\mathrm{N}$, $|F_y| > 3\,\mathrm{N}$, $|M_z| > 5\,\mathrm{Nm}$, $|Q_1| > 0.02\,\mathrm{Nm}$.

2.2.2. Wave case

To approximate the mean wave forces, a new mathematical model was developed in this work. The model makes use of the periodicity of the mean forces in the encounter angle α to model this functional relationship with a Fourier series including coefficients up to 6th order, see Uharek and Cura Hochbaum (2015):

$$F = \frac{a_0}{2} + \sum_{n=1}^{6}\{a_n\cos(n\alpha) + b_n\sin(n\alpha)\} \tag{2.33}$$

The influence of the wave length λ on the mean forces is captured by wave length dependent Fourier coefficients:

$$F = \frac{a_0}{2} + \sum_{n=1}^{6}\{a_n(\lambda)\cdot\cos(n\alpha) + b_n(\lambda)\cdot\sin(n\alpha)\} \tag{2.34}$$

A polynomial approach is used to approximate the dependence of these coefficients on the wave length:

$$\begin{aligned} a_n(\lambda) &= a_{n3}\lambda^3 + a_{n2}\lambda^2 + a_{n1}\lambda + a_{n0} = \sum_{i=0}^{3} a_{ni}\lambda^i \\ b_n(\lambda) &= b_{n3}\lambda^3 + b_{n2}\lambda^2 + b_{n1}\lambda + b_{n0} = \sum_{i=0}^{3} b_{ni}\lambda^i \end{aligned} \tag{2.35}$$

The coefficients a_{ni} and b_{ni} are obtained for four different forward speeds and a linear interpolation is used for the calculation of forces during the manoeuvre.

It should be noted that due to the used polynomial approach, this procedure should not be used for extrapolation. To simplify the problem, it is assumed that no coupling between calm water manoeuvring and wave dependent hydrodynamic forces exists and thus the motion of the ship (e.g. the drift angle) has no influence on the mean wave forces.

Under the assumption of a quadratic dependence of the mean wave forces on the squared wave amplitude (ζ_A^2), the mean forces in waves are made non-dimensional as follows:

$$F'_x = \frac{F_x}{\rho g L_{PP} \zeta_A^2} \quad F'_y = \frac{F_y}{\rho g L_{PP} \zeta_A^2} \quad M'_z = \frac{M_z}{\rho g L_{PP}^2 \zeta_A^2} \tag{2.36}$$

Please note that the validity of this assumption is discussed in Section 3.2.3.

According to the linear wave theory, the mean wave force in a irregular seaway can be considered as a superposition of its regular contributions. In addition to this mean value there is the so called slowly varying drift force with a long period resulting from a difference in frequency between two wave components. The mean value of this slowly varying drift force is zero, see Faltinsen (1990).

2.2.3. Modelling of propeller revolution rate dependent forces and moments

In order to simulate manoeuvres in waves with different power settings during the approach phase, the dependence of the global hydrodynamic forces on the propeller revolution rate is needed. This dependence could be captured by performing additional captive tests in calm water with a varying propeller revolution rate. However, due to the strong coupling between the rudder angle, forward speed and propeller revolution rate, this approach would increase the number of virtual captive model tests significantly.

Under the assumption, that not only the propeller forces but also the global hydrodynamic forces only depend on the advance ratio, simulation of manoeuvres with changing propeller revolution rates can be simulated without the need of any additional tests.

With v_A being defined as the average inflow velocity in the propeller plane, n the propeller revolution rate and D the diameter of the propeller, the advance ratio is defined as:

$$J = \frac{v_A}{nD} \tag{2.37}$$

This relation shows, that for the advance ratio – and thus the global hydrodynamic forces – an increase of the propeller revolution rate is expected to have the same effect as a reduction of the ship velocity u, assuming that the effective wake field does not change. This assumption seems valid for moderate changes of n or u.

This assumption allows to interpret forward speed dependent coefficients (as for example X_u) of the hydrodynamic coefficient set as coefficients describing a specific propeller operating point. To include this in the mathematical model of the calm water forces the revolution rate factor n^* is introduced, which is equal to the ratio between the requested propeller revolution rate n and the propeller revolution rate n_0 used to determine the hydrodynamic coefficient set:

$$n^* = \frac{n}{n_0} \tag{2.38}$$

Since an increase of 20% of the propeller revolution rate $n^* = 1.2$ is then equivalent to a reduction of the forward speed of $u^* = \frac{1}{n^*}u$, the effective Δu is:

$$\Delta u = u^* - u_0 = \frac{1}{n^*}u - u_0 \tag{2.39}$$

This parameter is made non-dimensional using u^*:

$$\Delta u' = \frac{\Delta u}{u^*} = \frac{\frac{1}{n^*}u - u_0}{\frac{1}{n^*}u} = 1 - \frac{u_0}{u}n^* \tag{2.40}$$

All other parameters including the hydrodynamic forces for calm water manoeuvring are still made non-dimensional as defined in (2.24), using u rather than u^*.

2.3. Computation of viscous flow forces and moments

In this work, the hydrodynamic forces that are needed to determine the coefficients of the mathematical model are obtained numerically. The viscous flow around the ship hull is described by the Navier-Stokes and continuity equations.

2.3.1. Governing equations

The Navier-Stokes equation for an incompressible fluid is derived from the conservation of momentum (Spurk, 1996). Stated in an inertial Cartesian coordinate system using index notation it reads:

$$\frac{\partial\left(\rho\, v_i\right)}{\partial t}+\frac{\partial\left(\rho\, v_i\, v_j\right)}{\partial \xi_j}=\rho b_i-\frac{\partial p}{\partial \xi_i}+\frac{\partial}{\partial \xi_j}\left[\mu\left(\frac{\partial v_i}{\partial \xi_j}+\frac{\partial v_j}{\partial \xi_i}\right)\right] \tag{2.41}$$

where ρ is the density of the fluid, v_i are the Cartesian components of the fluid velocity, b_i are the components of external body forces (as for example the gravitational force), p is the pressure, and μ is the dynamic viscosity of the fluid. Although the Navier-Stokes equation describes turbulent flows as well, the required spatial and temporal resolution for numerical solutions make it at the moment impossible to compute the turbulent flow around a ship directly by using (2.41). Thus the velocity is decomposed into a mean part $\overline{v}_i$ and a fluctuating part v_i' and only the ensemble averaged solution is obtained by solving the Reynolds-averaged Navier-Stokes (RANS) equations:

$$\frac{\partial\left(\rho\, \overline{v}_i\right)}{\partial t}+\frac{\partial\left(\rho\, \overline{v}_i\, \overline{v}_j\right)}{\partial \xi_j}=\rho b_i-\frac{\partial \overline{p}}{\partial \xi_i}+\frac{\partial}{\partial \xi_j}\left[\mu\left(\frac{\partial \overline{v}_i}{\partial \xi_j}+\frac{\partial \overline{v}_j}{\partial \xi_i}\right)\right]-\frac{\partial\left(\rho\overline{v_i' v_j'}\right)}{\partial \xi_j} \tag{2.42}$$

The additional term $\rho\overline{v_i' v_j'}$ is called the Reynolds stress tensor, which contains the unknown fluctuations of the turbulent flow. The introduction of these additional unknowns leads to the so called closure problem of the RANS equations. Since from here on only the mean flow is considered, the bar over the variables is omitted.

By introducing the Reynolds number defined as:

$$\mathrm{Rn}=\frac{u_r L_r}{\nu} \tag{2.43}$$

and the Froude number defined as:

$$\mathrm{Fn}=\frac{u_r}{\sqrt{g L_r}} \tag{2.44}$$

a non-dimensional formulation of (2.42) is obtained by dividing the whole equation by $\rho u_r^2 L_r^2$ with u_r and L_r being an arbitrary reference velocity and length respectively.

In addition to the Navier-Stokes equation, just the mass conservation needs to be satisfied when computing an incompressible flow. The continuity equation reads in this case:

$$\frac{\partial v_j}{\partial \xi_j}=0 \tag{2.45}$$

This equations are used to derive a solution procedure for the computation of the pressure field, as will be outlined in Section 2.3.4.

Turbulence modelling

A significant step to the solution of the closure problem mentioned above was proposed by Boussinesq, who introduced the concept of an eddy viscosity μ_t to replace the Reynolds stress tensor, see for example Wilcox (1993):

$$-\rho\overline{v_i'v_j'} = \mu_t\left(\frac{\partial\overline{v}_i}{\partial\xi_j} + \frac{\partial\overline{v}_j}{\partial\xi_i}\right) - \frac{2}{3}\delta_{ij}\rho k \tag{2.46}$$

where $k = \frac{1}{2}\overline{v_i'v_j'}$ is the turbulent kinetic energy. A widely accepted model for the turbulent kinetic energy and the eddy viscosity was proposed by Wilcox (1993) and is based on the solution of two additional differential equations for the turbulent kinetic energy k and the specific rate of dissipation ω. The eddy viscosity can then be computed using the following relationship:

$$\mu_t = \frac{\rho k}{\omega} \tag{2.47}$$

The differential equations for k and ω are:

$$\frac{\partial\rho k}{\partial t} + \frac{\partial\rho v_j k}{\partial\xi_j} = \mu_t\left(\frac{\partial v_j}{\partial\xi_i} + \frac{\partial v_i}{\partial\xi_j}\right)\frac{\partial v_i}{\partial\xi_j} - \rho\beta^* k\omega + \frac{\partial}{\partial\xi_j}\left[(\mu + \sigma^*\mu_t)\frac{\partial k}{\partial\xi_j}\right] \tag{2.48}$$

$$\frac{\partial\rho\omega}{\partial t} + \frac{\partial\rho v_j\omega}{\partial\xi_j} = \rho\gamma\left(\frac{\partial v_j}{\partial\xi_i} + \frac{\partial v_i}{\partial\xi_j}\right)\frac{\partial v_i}{\partial\xi_j} - \rho\hat{\beta}\omega^2 + \frac{\partial}{\partial\xi_j}\left[(\mu + \sigma\mu_t)\frac{\partial\omega}{\partial\xi_j}\right] \tag{2.49}$$

with the additional constants:

$\gamma = \frac{5}{9}$, $\hat{\beta} = 0.075$, $\beta^* = 0.09$ and $\sigma^* = \sigma = 0.5$.

Wall functions are used at the no slip boundaries to bypass the near-wall region of the boundary layer. The used wall functions are valid in the range of $30 < y^+ < 200$, where y^+ is a non-dimensional wall distance (Wilcox, 1993).

Free surface modelling

To capture the position of the interface between the two fluids, water and air, the level set technique (Osher and Sethian, 1988; Sussman et al., 1994) is used. It is based on a signed distance function ϕ to define the interface, located at $\phi = 0$, between both fluids. This function is transported using the following differential equation:

$$\frac{\partial \phi}{\partial t} + \frac{\partial v_j \phi}{\partial \xi_j} = 0 \tag{2.50}$$

For the numerical solution procedure, water and air are treated as two phases of the same fluid with corresponding density and viscosity. For numerical reasons it is preferable to have a smooth transition of these properties at the interface, rather than a discontinuity. Therefore a transition region of width 2α is defined at the interface. The fluid properties can then be computed using an interpolation factor c_ϕ:

$$c_\phi = \begin{cases} 1 & \phi > \alpha \\ \frac{1}{2}\left(1 + \sin\frac{\pi\phi}{2\alpha}\right) & \alpha \leq \phi \geq -\alpha \\ 0 & \phi < -\alpha \end{cases} \tag{2.51}$$

This interpolation factor is 1 for water and 0 for air. The density of the fluid can then be computed as:

$$\rho = \rho_A + c_\phi \left(\rho_W - \rho_A\right) \tag{2.52}$$

where ρ_A is the density of air and ρ_W is the density of water. The computation of the viscosity is analogous.

The disadvantage of the level set method is that it is not intrinsically mass conservative and that after solving the transport equation, the updated level set function ϕ is not a signed distance function any more and thus there is a spreading of the transition region. This is countered by solving the reinitialisation equation:

$$\frac{\partial \hat{\phi}}{\partial \tau} + S(\phi)\left(\sqrt{\frac{\partial \hat{\phi}}{\partial \xi_i}\frac{\partial \hat{\phi}}{\partial \xi_i}} - 1\right) = 0 \tag{2.53}$$

where τ is an pseudo time step required to solve the differential equation and $S(\phi)$ is the smoothed sign function:

$$S(\phi) = \frac{\phi}{\sqrt{\phi^2 + \epsilon^2}} \tag{2.54}$$

The smoothing factor ϵ determines the region where the reinitialisation is suppressed in order to ensure that the interface is not moved during the reinitialisation. Subsequently, the level set function ϕ is replaced by the reinitialised level set function $\hat{\phi}$.

Non inertial formulation and treatment of ship motions

If the RANS equations (2.42) are stated in a moving, non inertial coordinate system, additional terms containing the apparent forces that seem to act on the fluid are added to the RANS equations.

$$\frac{\partial v_i}{\partial t} + \frac{\partial \left(v_i\, v_j\right)}{\partial x_j} = b_i - \frac{1}{r_1}\frac{\partial p + 2/3 r_1 k}{\partial x_i} + \frac{\partial}{\partial x_j}\left[\left(\frac{r_2}{\mathrm{Rn}} + \nu_t\right)\left(\frac{\partial v_i}{\partial x_j} + \frac{\partial v_j}{\partial x_i}\right)\right] + \frac{\cos\alpha_i}{\mathrm{Fn}^2}$$
$$- \left(\dot{u}_i + \epsilon_{ijk}\omega_j u_k\right) - \epsilon_{ijk}\omega_j\epsilon_{kmn}\omega_m x_n - 2\epsilon_{ijk}\omega_j v_k - \epsilon_{ijk}\dot{\omega}_j x_k \tag{2.55}$$

In this equation u_i is the considered ship fixed velocity component of the ships origin, $\dot{u}_i$ its time derivative, ω_i the ship fixed components of the angular velocity vector, $\dot{\omega}_i$ its time derivative and x_i the ship fixed coordinates of an arbitrary point. Further, the gravitational force has been separated from the body force term b_i, where α_i denotes the direction cosine of the gravitation vector.

It should be noted that (2.55) is stated for a two phase flow, with the density ratio $r_1 = \rho/\rho_W$ and the viscosity ratio $r_2 = \nu/\nu_W$ with the suffix W for water. Strictly, this is mathematically not correct, since a constant density was assumed for the division of the equation by ρ. However, the region where this assumption is invalid – namely at the interface – is small and the fluid properties in this region are artificial anyway and thus the error introduced by this formulation is negligible.

If the RANS equations are solved in a moving frame of reference, the computation of a moving ship is possible without much additional effort. The ship motions can either be prescribed or computed by solving (2.9) in each time step. In addition to adding the apparent forces, the boundary conditions need to be changed to consider the transport velocities due to the rigid body motion and the direction cosines of the gravitation vector need to be updated in every time step.

2.3.2. Numerical wave generation and damping

The original wave generation and damping strategy implemented in Neptuno (Cura Hochbaum and Vogt, 2002) has been extended and improved during this thesis. Waves are prescribed at the inlet borders – in the case of an oblique incoming wave for example the front and starboard boundary – and now also inside the computational domain by prescribing the velocities to the sum of the orbital velocity components of the wave and

the transport velocities resulting from the rigid body motion. At the inlet boundaries the free surface elevation is prescribed as well. The waves are damped towards the outlets of the computational domain – e.g. the boundaries at the port side and behind the ship – and the hydrostatic pressure of the undisturbed flow is prescribed there.

The velocity components of the undisturbed wave are computed using the linear (Airy) wave theory. A detailed description can be found for example in Söding (1982) and therefore only the used equations are briefly recalled here. The surface elevation at time t and position ξ of a harmonic wave with the amplitude ζ_A with a phase shift ϵ is:

$$\zeta_W(t,\xi) = -\zeta_A \sin(k\xi + \omega t + \epsilon) \tag{2.56}$$

where k is the wave number and ω is the wave frequency:

$$k = \frac{2\pi}{\lambda} \tag{2.57}$$

$$\omega = \sqrt{gk \tanh(kH)} \tag{2.58}$$

where λ is the wave length and H is the water depth. The wave velocity components u_W and w_W at the depth ζ are derived from the velocity potential Φ:

$$u_W(t,\xi,\zeta) = -\omega\zeta_A \frac{\cosh(k(\zeta - H))}{\sinh(kH)} \sin(k\xi + \omega t + \epsilon) \tag{2.59}$$

$$w_W(t,\xi,\zeta) = \omega\zeta_A \frac{\sinh(k(\zeta - H))}{\sinh(kH)} \cos(k\xi + \omega t + \epsilon) \tag{2.60}$$

The generated wave propagates in the negative direction of the earth fixed ξ-axis. To generate beam and following waves, the ship fixed coordinate system is turned relative to the earth fixed system by the wave encounter angle α as defined in Figure 2.3.

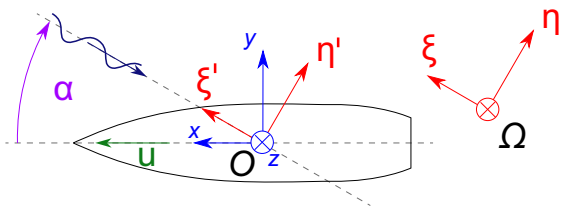

Figure 2.3.: Definition of the wave encounter angle α

Since the ship is moving with a forward speed u, the wave encounter frequency ω_e at the ship differs from the wave frequency ω:

$$\omega_e = \omega - ku\cos\mu \tag{2.61}$$

where μ is the wave encounter angle, which is equal to $\mu = 180° - \alpha$. For situations where a drifting ship encounters waves, the commonly used expression for ω_e needs to be extended:

$$\omega_e = \omega + k\sqrt{u^2 + v^2}\cos(\alpha + \beta) \tag{2.62}$$

To improve the quality of the generated wave inside the computational domain as well as to damp the wave before reaching the outlet of the computational domain, additional body force source terms have been added on the right hand side of the RANS equations. The approach used here is based on the work of Schumann (2015). In addition to this „numerical beach“, an expansion of the cells toward the outlet supports the damping by the introduction of numerical diffusion.

The additional source terms b_i that have been added to the right hand side of the RANS equation are:

$$b_i = c_b k_r(x_i)(u_i - u_{S,i}) \tag{2.63}$$

where c_b is a constant which controls the strength of the numerical beach. If this factor is too small, the waves are not damped efficiently and if it is too large, the numerical beach itself leads to reflections in the domain. Current work by Perić and Abdel-Maksoud (2016) showed, that the optimal damping factor can be estimated in advance. The factor k_r is position dependent and controls the range in which the numerical beach is active. In the vicinity of the ship k_r is zero and in the region where the beach should be fully active, it takes the value of one, see Figure 2.4a. To avoid prescribing pressure and velocity at the outlet boundaries of the computational domain, the factor k_r is set to zero again before reaching the boundary. The value $u_{S,i}$ is the target value of the velocity and is defined as:

$$u_{S,i} = u_T + k_W(x_i)u_{W,i} \tag{2.64}$$

where u_T is the transport velocity in the ship fixed coordinate system and $u_{W,i}$ is the orbital velocity of the wave. The position dependent factor k_W controls the area in which the wave should be present. Since the grid is expanded towards the outlet, the wave should not be prescribed in regions with coarse resolution. In addition, a conflicting boundary condition exists in the corners of the computational domain. Thus a cosine ramp is used to damp the prescribed wave amplitude towards the edges as described in Uharek (2013). The region in which the wave is prescribed is shown in Figure 2.4b. Figure 2.4c shows the product of k_W and k_r, being the region in which the waves are generated by the numerical beach.

The model has proven to work well and significantly increased the convergence in calm water simulations by reducing the reflections inside the computational domain, see for example Uharek et al. (2016).

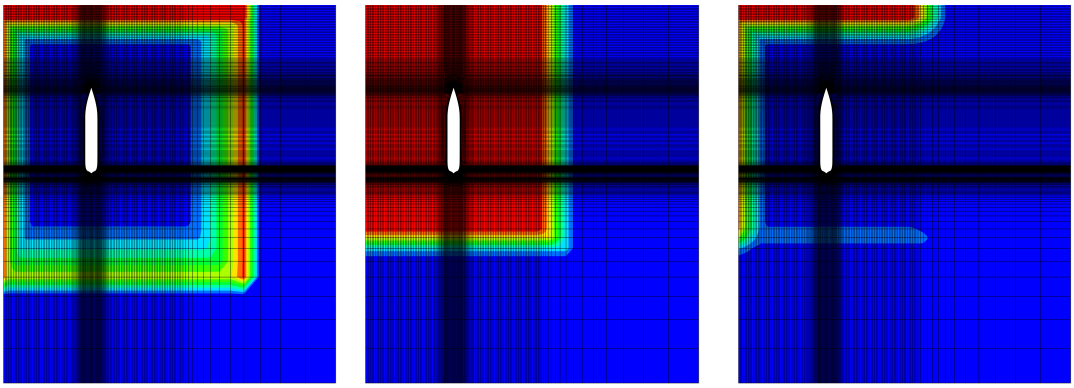

(a) Region of numerical beach k_r in red (b) Region of wave k_W in red (c) Product of k_W and k_r

Figure 2.4.: Parameters of the numerical beach

2.3.3. Body force model

The computed inflow to the rudder and thus the resulting forces are strongly influenced by the effect of the operating propeller. Although it would be possible to include the rotating propeller in the computations using for example a sliding interface technique, it would drastically increase the computational time, since the static test could no longer be computed as a steady case, but would require a temporal discretisation at a very small time scale. A commonly used alternative method is to model the effect of the propeller using body forces. As Cura Hochbaum (2006) and Yao (2015) has shown, a sophisticated body force model is capable of replacing the effect of the propeller in all static and dynamic tests. The body force model used in this work is based on RANS computations of the propeller in homogeneous oblique inflow conditions, which do consider different propeller revolution rates and inflow angles. The forces per unit area acting on the blade are averaged over one propeller revolution and then mapped onto a circular grid. The resulting force distributions for each condition are then stored in a database. During the RANS simulation of the flow around the ship, the forces corresponding to the current local inflow conditions are then determined and added to the right hand side of the momentum equations in each volume cell in the body force region of the computational grid, see Figure 2.5. Further details can be found in Yao (2015); Koopmann et al. (2015).

2.3.4. Numerical solution procedure

Since no analytical solution of the Navier-Stokes equations is known for the current application case, the corresponding equations are solved numerically. This is done using the RANS code Neptuno, which employs the finite volume method to discretise the differential expressions in the governing equations in a finite computational domain. A detailed description of the implementation can be found in Cura Hochbaum (1993) and

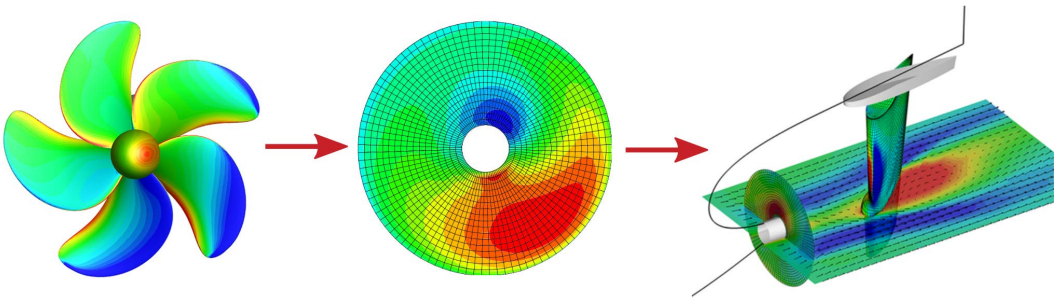

Figure 2.5.: Concept of the body force model

therefore only a brief summary of the main characteristics is given. The code uses the SIMPLE method introduced by Patankar and Spalding (1972) to couple pressure and velocity. In this method at first the RANS equations are used to compute the three fluid velocity components in each cell using the pressure from the previous time step. In a second step, a pressure correction equation – derived from the continuity equation – is used to solve for a pressure correction to obtain a divergence free velocity field. This method needs some iterations in each time step to converge. In order to simplify the numerical solution, the non-linearity in the convection term is eliminated using the so called Picard linearisation, taking the transport velocity (flux) from the last SIMPLE iteration.

In the used code, the fluxes and diffusive terms are approximated using a central differencing scheme (CDS), and the transported variables using a linear upwind differencing scheme (LUDS), except for k and ω, for which an upwind differencing scheme (UDS) is used. Only the values in the six adjacent cells of the used block structured grid are treated implicitly, the other values are taken to the right hand side of the respective transport equation and treated explicitly. The linear algebraic equation system that results from this discretisation is then solved using the TDMA algorithm on alternating grid lines. The solution of the equation system is underrelaxated in order to ensure a stable numerical solution. Further details can be found in Cura Hochbaum (1993).

2.3.5. Verification procedure

The iterative convergence of each individual computation is checked using the L1 norm of the residual for the momentum equation and the sum of the absolute values of the right hand side of the pressure correction equation, which are equal to the violation of the mass conservation in the considered cell. Since all three momentum equations need to converge, only the largest of the three residuals is shown in the plots. In case of stationary and pseudo-instationary computations of a steady flow case, a computation is found to be converged if the solved variables become constant while the residuals keep dropping. For practical reasons in the current application, the observed variables were the forces acting on the hull and appendages. Figure 2.6 shows the residuals normalised

by the respective initial value and the side force on the ship as an example for a converged steady flow computation.

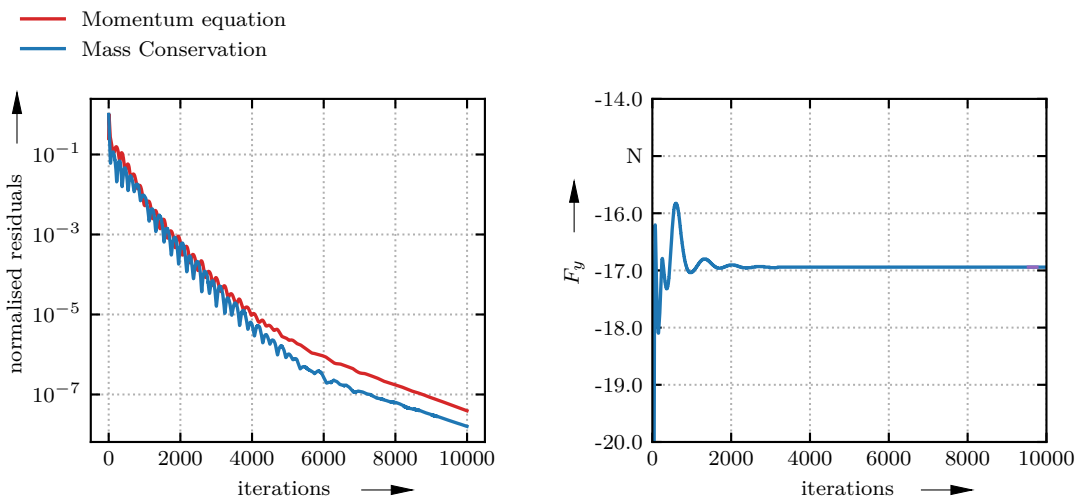

Figure 2.6.: Check of iterative convergence for a stationary case

It should be noted that pseudo-instationary computations that include a free surface often show reflections (at least to some extent) at the boundaries of the computational domain. Due to this fact, the resulting forces might oscillate, resulting in a weaker convergence or even stagnation of the residuals. The computation is still found to be converged if the force oscillates around a constant mean value and the amplitude is being reduced in the course of the computation. Figure 2.7 shows an example for a converged pseudo-instationary solution with reflections.

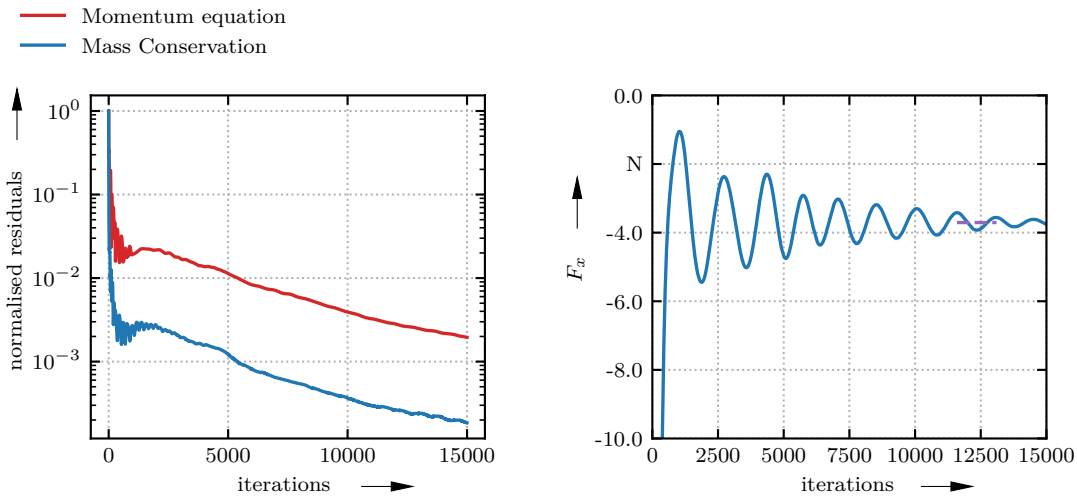

Figure 2.7.: Check of iterative convergence for a pseudo-instationary case

Since for unsteady flow computations the solved variables don't become constant, the convergence of such computations can only be observed for each individual time step. For this purpose, the maximum of the L1 norm of the residuals of the momentum equations and the sum of the absolute values of the right hand side of the pressure correction equation is plotted at the beginning and the end of each time step.

Figure 2.8 shows an example for a converged instationary solution. The thick lines denote the residuals at the beginning of each time step, whereas the thin lines denote the residuals at the end of each time step. The difference between those two lines is the drop in the residual in each time step. Because most instationary computations are restarted from the converged solution of a stationary computation, e.g. from the steady straight ahead motion in calm water before incoming waves reach the ship, the drop in the residuals is less pronounced than in the static case, since the initial solution is already a relatively good approximation.

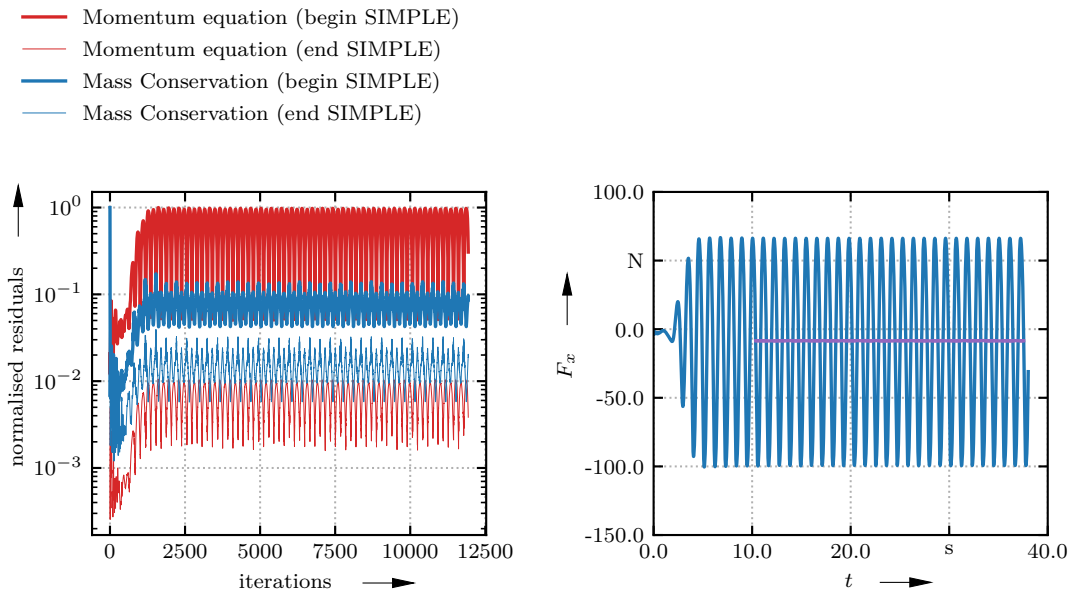

Figure 2.8.: Check of iterative convergence for a instationary case

In addition to the error of the iterative solution, the spacial and temporal discretisation error is investigated. For this purpose a systematic variation of the parameters Δt and Δx is performed. The investigation of spacial and temporal convergence for both grids considered in this work as well as a description of the procedure can be found in the Appendix B.2.1.

2.4. Application case – S175 ship

The procedure described above is applied to the benchmark ship S175, a single screw container ship. The container ship has classical lines with a cruiser stern, as can be seen

in the body plan in Figure 2.9. This ship has been selected, since experimental data is available for mean forces and manoeuvres from Yasukawa and Adnan (2006); Yasukawa and Nakayama (2009); Yasukawa et al. (2010). The model tests were performed at model scale of 1:50 at Mitsubishi Heavy Industries. The main particulars for the full scale ship and model are listed in Table 2.1. Three springs were used to provide the restoring forces, resembling the experimental setup as described in Section 1.2.1.

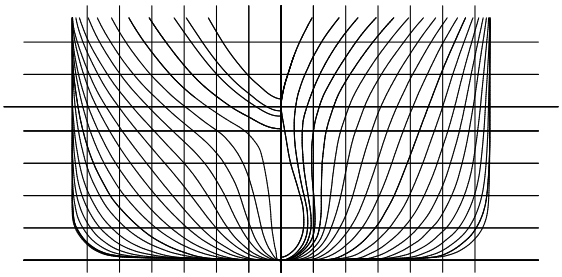

Figure 2.9.: Body plan of S175 ship

Table 2.1.: Main dimensions of S175 ship

	full scale	model scale
L_{pp}	175.0 m	3.500 m
B_{wl}	24.5 m	0.508 m
T	9.5 m	0.190 m
V	24172 m^3	0.1934 m^3
x_G	−2.545 m	−0.051 m
z_G	0 m	0 m
k_{yy}/L_{pp}	0.269	
k_{zz}/L_{pp}	0.269	
c_B	0.572	
U	12.1 kn	0.879 m/s
GM	1.0 m	0.02 m
Fn	0.15	
Rn	1.1 10^9	3.1 10^6

For the cases in waves, the experimental setup from Yasukawa was resembled. It consisted of one longitudinal spring with a stiffness of $c_x = 529.74\,\mathrm{N/m}$ attached at the centre of gravity and two transversal springs attached at force gauges 1.15 m before and 1.22 m behind the centre of gravity with a stiffness of 313.92 N/m each.

During the free running experiments, the propeller 1280 from the Mitsubishi Experimental Tank was used. Since no 3D model of the propeller could be obtained, an existing body force database of a propeller with a similar open water curve has been used, which is a common practice for the determination of manoeuvring derivatives.

Figure 2.10 shows the open water curve of the used stock propeller (Koopmann et al., 2015) compared to the open water curve of the propeller 1280 (Taniguchi, 1966) used during the model tests. It can be seen that despite the different values of K_T and K_Q curves, their slope are very similar. Thus the operating point of the propeller and the required torque will be different to the one in the model test, but the changes in thrust and torque will be similar. Details on the performed computations for the determination of the body force database can be found in Yao (2015) and Koopmann et al. (2015).

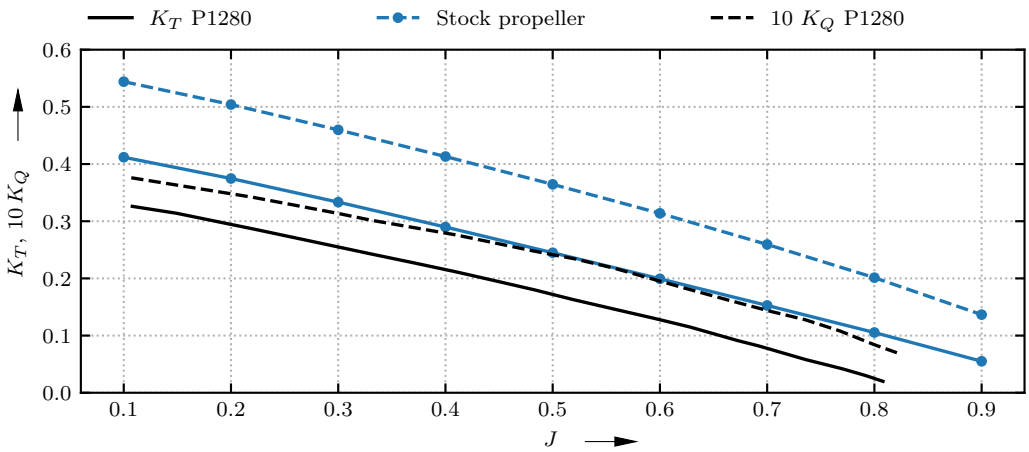

Figure 2.10.: Comparison of open water curves for propeller used in the experiment (Taniguchi, 1966) and stock propeller used in the simulations (Koopmann et al., 2015)

It should be noted that the procedure for the prediction of manoeuvres in waves has already been applied to and partially validated for other ships as well, see for example Cura Hochbaum and Uharek (2014); Lengwinat et al. (2016); Cura Hochbaum and Uharek (2016); Uharek and Cura Hochbaum (2018b).

2.4.1. Computational setup for calm water cases

All computations were performed simultaneously on a PC cluster using a single core each. The average computation time was 8 hours for a static case and 50 hours per motion period for a dynamic test.

Computational grid Due to the low Froude number of the considered case, the wave field generated by the ship is expected to have a negligible influence on the hull forces. Thus only the underwater part of the hull was considered for the computation of forces in calm water. The grid has been created using the `GridPro` meshing program and is shown in Figure 2.11. At the stern of the ship, a cylindrical region for the body forces was included as indicated in blue in Figure 2.12. The semi balanced rudder was meshed without any simplifications for the rudder angles $\delta = 0°, \pm 10°, \pm 20°, \pm 25°, \pm 30°, \pm 35°$. The rudder grid is included in a rudder box, indicated in red in Figure 2.12, which has

non matching interfaces with the other blocks of the grid. This allows considering all rudder angles without modifying the ship grid. The boundaries of the computational domain are located 1.2 L_{PP} in front, 1 L_{PP} to the side and 1.5 L_{PP} behind the ship.

The results of the performed grid convergence study including an uncertainty analysis can be found in Appendix B.2.1. The computations for the determination of hydrodynamic coefficients were performed on the medium grid with 1.2 Million cells.

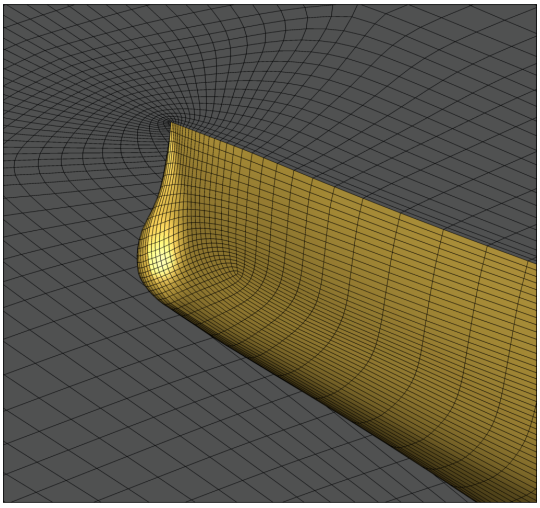

(a) Bow region

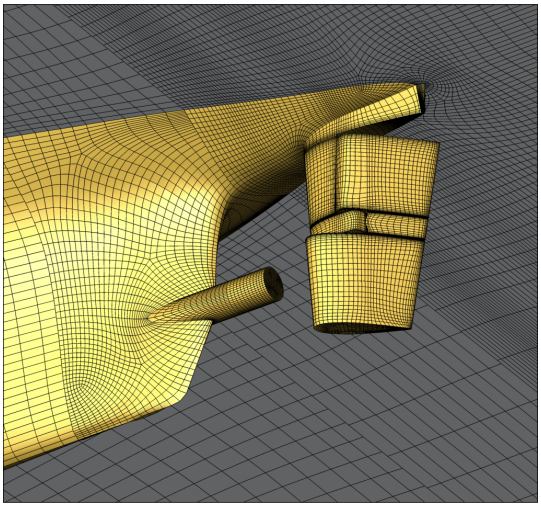

(b) Stern region

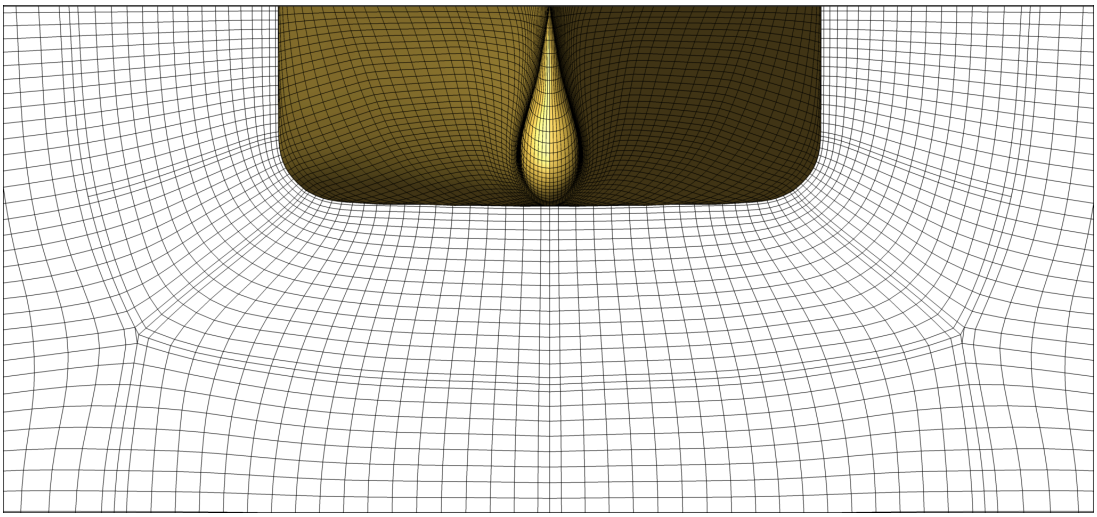

(c) Slice midships

Figure 2.11.: Grid without free surface

Boundary conditions For all computations without free surface the transport velocity of the fluid for the moving ship as well as the turbulent kinetic energy k and dissipation rate ω are prescribed at the inlet and sides of the computational domain. At the outlet

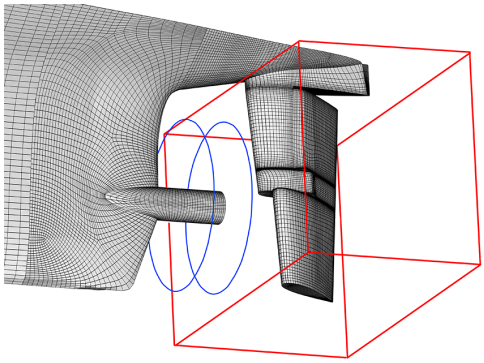

Figure 2.12.: Rudder box and body force region

of the computational domain the pressure is prescribed. Wall functions are used at the hull of the ship and a symmetry boundary condition (free slip wall) is applied at the top and bottom of the computational domain.

Solver settings The static computations were performed for 10000 SIMPLE iterations with an underrelaxation factor for the RANS equations of $\alpha_v = 0.4$, for the pressure correction equation $\alpha_p = 0.05$ and for the turbulence model equations $\alpha_t = 0.15$. The strong underrelaxation factors were chosen to guarantee a convergence of the equations in every case and allowed a fully automated computation of all cases. For the computations of dynamic cases, 2500 time steps per motion period and 10 SIMPLE iterations per time step were performed. To ensure a convergence in each time step, the underrelaxation factors were chosen to be $\alpha_v = 0.6$, $\alpha_p = 0.2$ and $\alpha_t = 0.3$.

2.4.2. Computational setup for wave cases

For the computation of mean wave forces the viscous flow around ship is computed. During the computations the ship is free to heave and pitch, while the surge, sway and yaw motion is weakly prescribed using the virtual spring system as explained above. The roll motion of the ship is suppressed. All computations are performed with the RANS code Neptuno.

Computational grid For the computation of mean wave forces a grid including the free surface has been created using the `GridPro` meshing program. A simplified rudder geometry without gaps is used for these computations. Five mesh refinement levels were considered to check for grid convergence, which is included in the Appendix B.3.1. As shown there, the medium grid with a total of 1.6 million cells is sufficient for all computations and will be the only grid used from here on.

Figure 2.13 shows the cells at the initial free surface level and the naming convention of the boundaries of the computational domain. The inlet is located 1 L_{PP} upstream

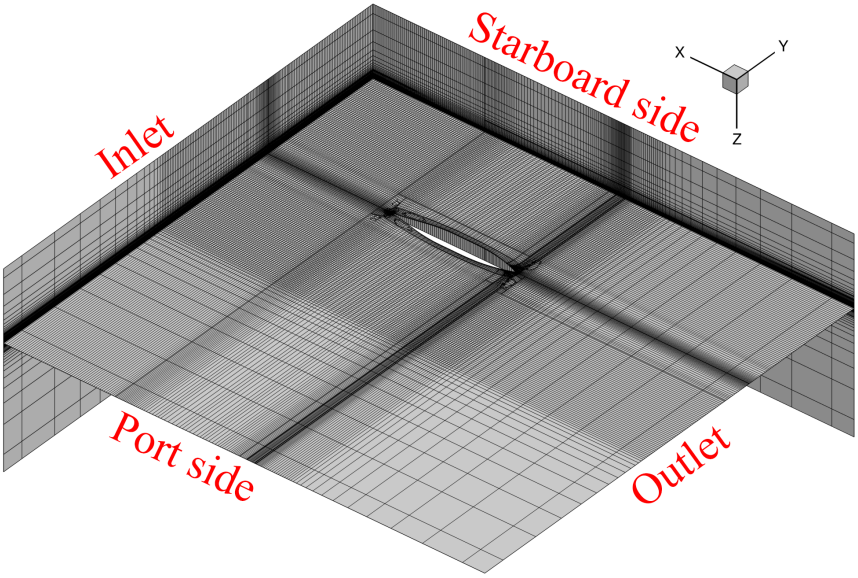

Figure 2.13.: Naming of the boundaries

of the bow, the outlet 2.4 L_{PP} behind the stern. The cells toward the outlet have been strongly expanded to provide additional numerical damping of the waves after passing the ship. The starboard boundary is located 1 L_{PP} away from the centre plane and has no expansion zone to allow the computation of oblique incoming waves. The port boundary is located 2.7 L_{PP} away from the centre plane and has an expansion zone. The bottom boundary is 1 L_{PP} below and the top boundary 0.6 L_{PP} above the free surface. All cases are computed on the same grid and the resolution was chosen high enough to maintain a satisfactory quality for all considered waves. The cell spacing in longitudinal and transversal direction in the free surface region is $\Delta x/L_{PP} = \Delta y/L_{PP} = 0.016$ and in vertical direction $\Delta z/L_{PP} = 0.0022$, see Figure 2.14.

To account for the movement of the free surface in the ship fixed computational domain due to the heave and pitch motion of the ship, the cells are spread out towards the inlet and outlet within a certain region. Figure 2.15 shows a slice at the centre plane of the ship. The red lines show the position of the (undisturbed) free surface for pitch angles $\theta = \pm 1°$.

Boundary conditions On the inlet, the starboard side, the top and bottom side of the computational domain the inflow velocity, consisting of the velocities due to the ship motion superposed with the orbital velocities of the incoming wave, and the free surface elevation according to the linear wave theory is prescribed. At the hull of the ship the no slip boundary condition is ensured using wall functions and at the outlet, the undisturbed hydrostatic pressure is prescribed.

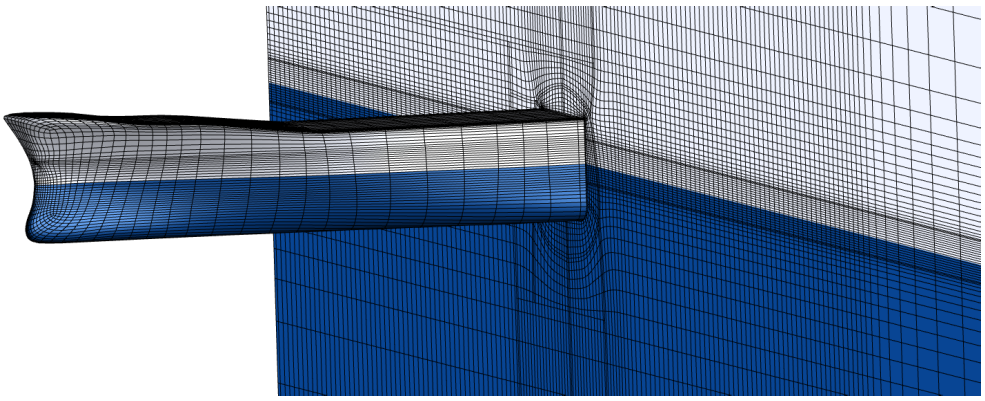

Figure 2.14.: Resolution of free surface area

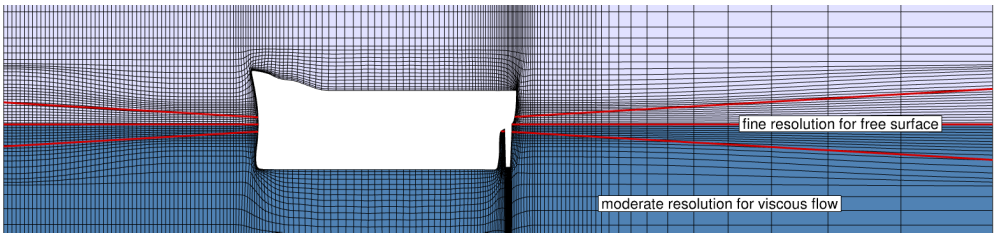

Figure 2.15.: Spreading of the cells to account for pitch motion in waves

Solver settings The computations are performed with a non-dimensional time step of $\delta t' = \delta t u_r / L_{PP} = 0.0008$ for Fn $= 0.15$, $\delta t' = 0.0006$ for Fn $= 0.1$ and $\delta t' = 0.0003$ for Fn $= 0.05$, corresponding roughly to 400 time steps per wave period for a head wave with $\lambda' = \lambda / L_{PP} = 1.0$. In each time step 10 SIMPLE iterations are performed. The underrelaxation factors for the velocity and pressure were chosen to $\alpha_v = 0.65$ and $\alpha_p = 0.15$ respectively. The domain was equipped with wave damping zones as described in Section 2.3.2. Since the computations are performed using only one processor core, the computation time varies greatly between different hardware, a typical computational time being 15 hrs per wave period.

3. Results and discussion

3.1. Calm water manoeuvring

The following section describes the results of the RANS simulations of the viscous flow around the ship during forced motions tests, performed to determine the hydrodynamic coefficient set for manoeuvring in calm water.

3.1.1. Determination of viscous flow forces and moments

In order to determine the calm water hydrodynamic coefficients, virtual CPMC tests are performed as described in section 2.2.1. At first, the self propulsion point of the model in calm water was determined. Figure 3.1 shows the results of computations for different propeller revolution rates to identify this point by linear interpolation between adjacent values. The resulting propeller revolution rate is $n_{\mathrm{MSPP}} = 8.135\,\mathrm{Hz}$. Due to the different propellers used, this value is not identical to the one reported by Yasukawa and Nakayama (2009), which was $n_{\mathrm{EXP}} = 10.05\,\mathrm{Hz}$.

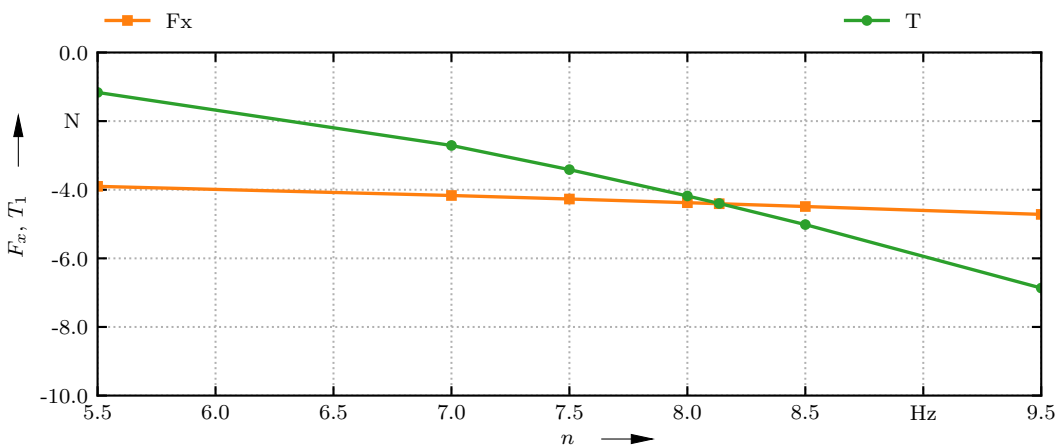

Figure 3.1.: Determination of model self propulsion point

An overview of the parameters of all performed static and dynamic tests can be found in Table A.1 and A.2 in the appendix.

In the following some interesting flow details obtained from the RANS computations are presented. Figure 3.2 shows the results of a computation with $\beta = 20°$ and $\delta = -35°$. At the top, the pressure distribution on the hull and a large vortex structure arising

from the bow of the ship is shown. This vortex can also be seen in a cutplane at the main section of the ship shown below.

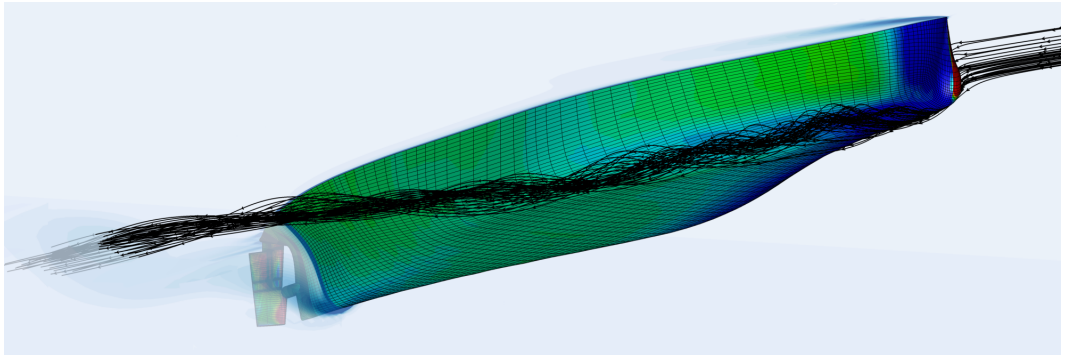

(a) Pressure distribution on the hull and leeward vortex system.

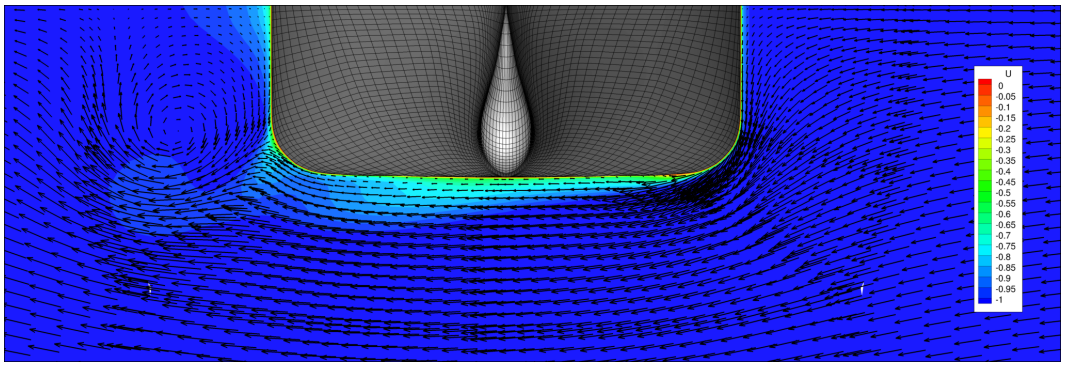

(b) Velocity in a cutplane at the main section.

Figure 3.2.: Snapshots of the flow around the hull at 20° drift angle

Additional computations have been performed with and without the operating body force model. To check the results obtained by the body force model, the computation for a straight ahead motion at 0.879 m/s and MSPP is performed and evaluated like a classical propulsion test as originally desribed in the 1978 ITTC Performance Prediction Methoded (ITTC, 2017; Lewis, 1988). It should be noted that due to the rather coarse resolution in the stern region, the missing consideration of the free surface and the use of a body force model this analysis is just performed for validation purposes and does not claim to provide the same accuracy as a numerically performed propulsion test.

For the case without operating body force model a resistance of 3.66 N was computed with friction coefficient $C_F = 3.679 \cdot 10^{-3}$ and a viscous pressure coefficient of $C_{VP} = 5.299 \cdot 10^{-4}$ leading to a form factor $k = \frac{C_{VP}}{C_F} = 0.144$, which is in the expected range for a slender container ship, see Schneekluth (1988). The friction coefficient from the ITTC-1957 frictional correlation line, which incorporates a form factor, is $C_F = 3.72 \cdot 10^{-3}$ (ITTC, 2017). For the computations with operating body force model, the thrust at MSPP is 4.4 N, leading to a thrust deduction factor $t = 1 - \frac{R_T}{T} = 0.17$. The computed propeller torque is 0.084 Nm.

Figure 3.3 shows the comparison between nominal (left) and total (right) wake field, with the nominal wake number being $w_{\text{nom}} = 0.34$ and the total wake number being $w_{\text{total}} = 0.183$. After subtraction of the induced velocities obtained using the actuator disk theory, an effective wake number of $w_{\text{eff}} = 0.383$ is predicted.

Skejic (2013) reported that the evaluation of Yasukawas measurement yielded a total wake of $w_{\text{total}} = 0.168$ and a thrust deduction factor of $t = 0.175$. When evaluating the effective wake number like a classical propulsion test using the thrust identity method, the resulting advance coefficient obtained from the open water curve of the propeller is $J_{TM} = 0.51$, leading to an effective wake number of 0.39. Thus it can be concluded that the used body force model yields reasonable results.

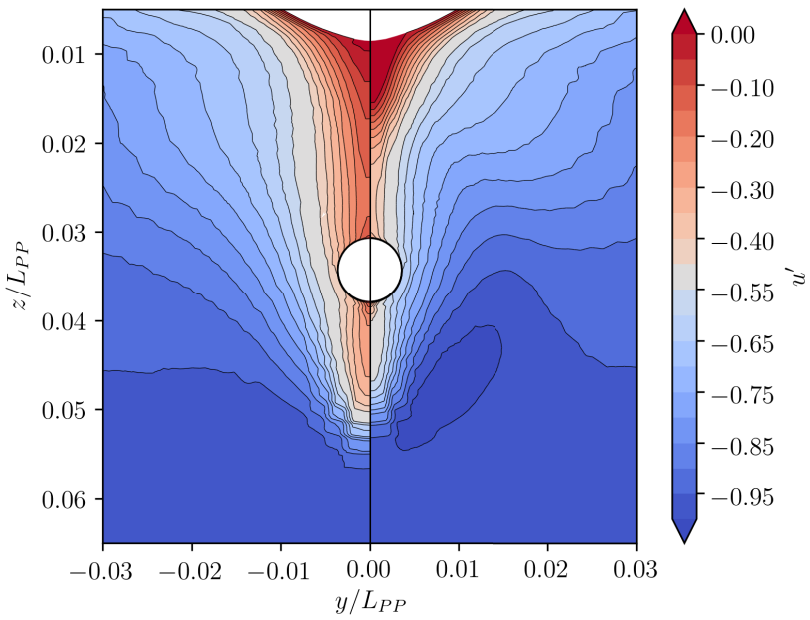

Figure 3.3.: Nominal (left) and total (right) wake field for straight ahead motion

Since all computations converged very well monotonically and no oscillations are observed in the time traces of the forces for the static tests, no averaging is performed but simply the value at the last iteration is used. After the forces for all situations are obtained, the hydrodynamic coefficients are determined as described in Section 2.2. The resulting coefficient set is shown in Table 3.1.

Figure 3.4 shows the dependence of the global longitudinal F_x and transversal F_y force and yaw moment M_z as well as the propeller torque Q_1 on the the drift angle β together with the traces reconstructed using the mathematical model. The symbols represent the results of the computations. As can be seen, the reconstruction of the global forces is very good, but the chosen model for the propeller torque is not able to capture all details of the dependence of propeller torque and longitudinal force on β due to its simplicity. The

Table 3.1.: Hydrodynamic coefficients for the S175 ship

	X	Y	N	Q
	10^{-3}	10^{-3}	10^{-3}	10^{-6}
0		0.075	−0.036	5.197
δ	−0.026	3.168	−1.522	0.029
$\delta\delta$	−1.327	−0.096	0.046	0.513
$\delta\delta\delta$	0.227	−3.128	1.500	−0.094
u	−2.716			−13.816
uu	1.293			8.716
uuu				0.471
$\dot{u}$	−0.424			
v	0.006	−15.948	−4.525	−0.073
vv	−1.366	−0.025	0.020	−4.179
vvv	−0.432	−97.918	−5.247	−0.763
$\dot{v}$		−8.375	0.104	
r	0.013	4.083	−2.912	0.139
rr	−0.442	−0.027	0.010	−0.638
rrr	0.026	0.633	−1.914	−0.068
$\dot{r}$		−0.248	−0.352	

	X	Y	N	Q
	10^{-3}	10^{-3}	10^{-3}	10^{-6}
vr	7.747	0.117	−0.033	4.988
vrr	−0.025	−35.313	−0.210	0.168
vvr	0.224	−17.546	−29.571	0.255
$v\delta$	0.607	0.277	−0.132	0.068
$vv\delta$	0.266	4.687	−2.119	0.316
$v\delta\delta$	−0.225	1.654	−0.697	−0.153
$r\delta$	−0.374	−0.104	0.050	0.097
$rr\delta$	0.034	0.755	−0.338	0.080
$r\delta\delta$	0.068	−1.033	0.581	−0.012
$u\delta$	−0.178	−4.195	2.061	−0.427
$u\delta\delta$	3.157	−0.683	0.322	−0.158
$u\delta\delta\delta$		5.892	−2.900	1.073
$uu\delta$		0.608	−0.302	0.010

absolute values of the relative errors of all considered computations are then averaged, the corresponding mean values are shown in Table 3.2. It should be noted that the longitudinal force during oblique towing tests is rather small and thus the relative error is large. The reason for a total positive longitudinal force at small drift angles is due to an increased thrust (and torque) of the propeller due to the changed inflow condition. Despite this, the general trends are captured very well. Due to the complexity of the propeller torque behaviour, a more accurate reconstruction would require to include more complex functions into the mathematical model and thus seems infeasible at the moment. The corresponding plots for the variation of the rudder angle δ, yaw rate r and forward speed change Δu can be found in the Appendix C.1.

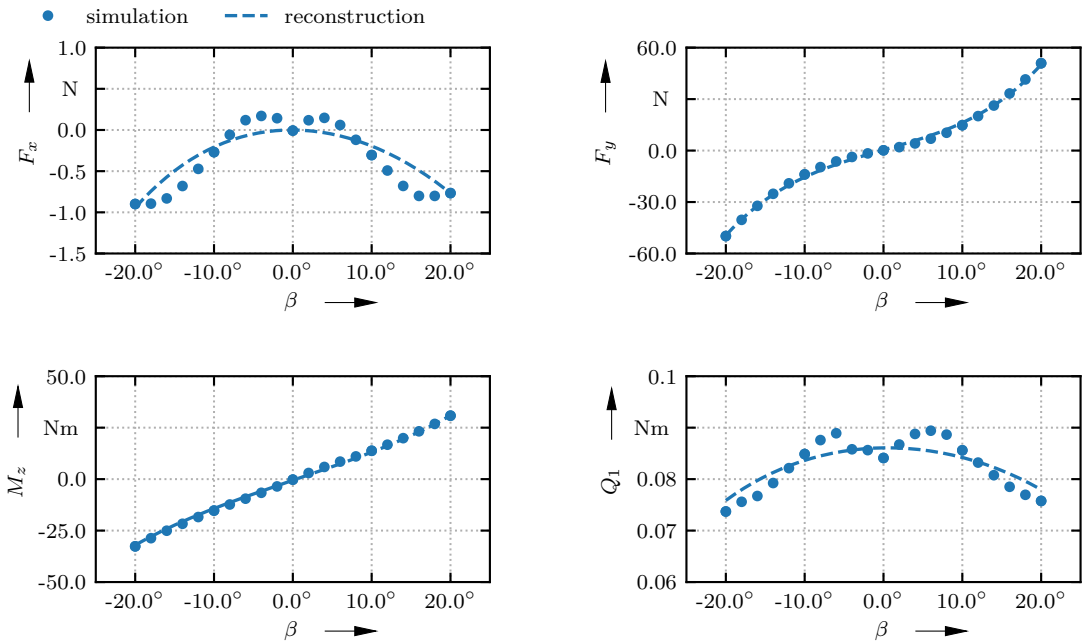

Figure 3.4.: Reconstruction of forces during static drift tests

Figure 3.5 shows analogous reconstructions for combined static sway / yaw tests. As can be seen, except for some situations where the reconstructed traces of the propeller torque deviate, most situations are also captured very well.

The reconstruction of the forces during a dynamic pure sway test can be found in Figure 3.6. For the dynamic tests, the absolute value of the difference between computed and reconstructed value is computed for every time step and averaged over one motion period. This average difference is shown in Table 3.3. The results of the other dynamic tests are shown in Appendix C.1. The reconstructions for all cases show a satisfactory agreement with the computed traces.

It can be concluded that the chosen mathematical model is capable of reconstructing the global forces in every situation with an average relative error of less than 10%.

Table 3.2.: Differences between computed and reconstructed values for forces during steady calm water captive model tests

varied parameter	F_x	F_y	M_z	Q_1
rudder ange	13%	5%	5%	2%
forward speed	4%			1%
drift angle	25%	10%	6%	2%
yaw rate	20%	7%	7%	2%
yaw rate / drift angle combined	12%	5%	6%	5%
rudder angle / drift angle combined	14%	6%	3%	2%
rudder angle / yaw rate combined	17%	4%	5%	2%
rudder angle / forward speed combined	8%	4%	4%	1%

Table 3.3.: Time averaged differences between computed and reconstructed values for forces during dynamic calm water captive model tests

test type	F_x	F_y	M_z	Q_1
pure surge	16%			4%
pure sway	56%	8%	6%	4%
pure yaw	80%	16%	19%	3%
combined sway/yaw	35%	12%	10%	4%
combined yaw/sway	33%	7%	26%	16%

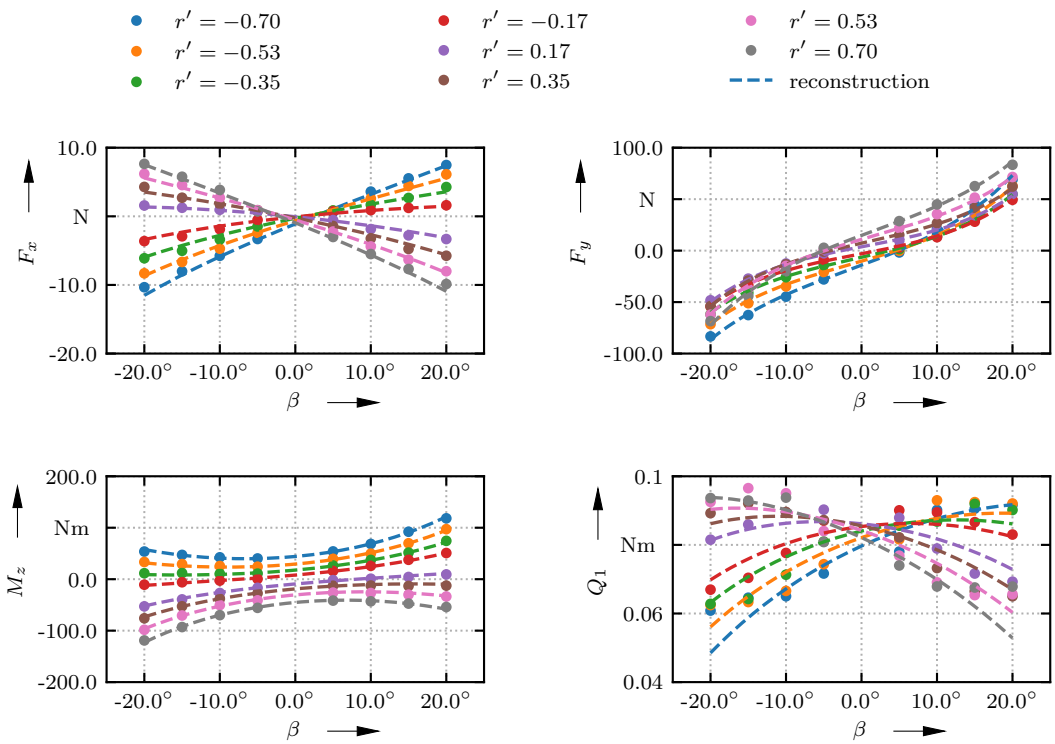

Figure 3.5.: Reconstruction of static combined sway-yaw tests

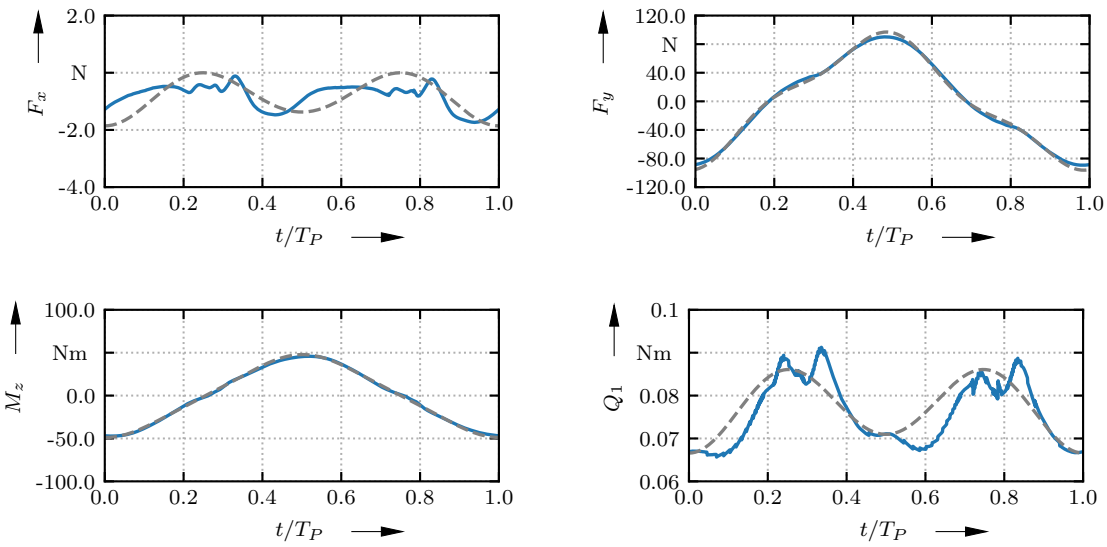

Figure 3.6.: Reconstruction of dynamic pure sway test

3.1.2. Validation of viscous flow computations

During the tests for the determination of the influence of the drift angle on mean wave forces, Yasukawa and Adnan (2006) have conducted oblique towing tests and measured the side force and yaw moment. The comparison of the numerically obtained results with this data can be found in Figure 3.7. As can be seen the agreement is quite good, however the range of drift angles covered by the experimental data is rather small.

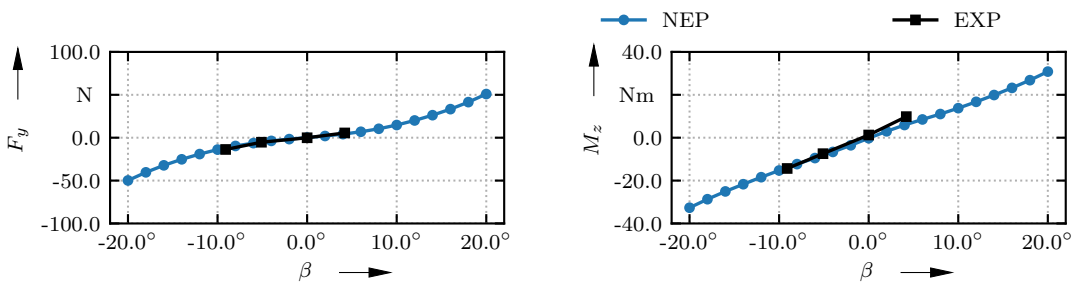

Figure 3.7.: Comparison of side force and yaw moment at steady drift motion with experimental data from Yasukawa and Adnan (2006)

Unfortunately no further public available validation data for calm water manoeuvring is known to the author. There are two more papers containing experimental data for the S175 manoeuvring in calm water, but they are for a condition trimmed to the stern, see Matsumoto and Suemitsu (1980) and Son and Nomoto (1981).

3.1.3. Validation of propeller revolution rate modelling

Additional computations for different (constant) propeller revolution rates n have been performed, to check the proposed approach of capturing the dependence of global forces on the propeller revolution rate by using coefficients determined for different forward speeds, see Section 2.2.3.

The symbols in Figure 3.8 show the total longitudinal F_x and transversal F_y force, the yaw moment M_z and propeller torque Q_1 computed for different propeller revolution rates ranging from 5.5 Hz to 9.5 Hz. The reconstructions (dashed lines) are obtained with the existing coefficient set without including any of these computations.

As can be seen, except for the longitudinal force at 5.5 Hz, which lies outside the valid range of the model, and some slight discrepancies at small rudder angles in side force and yaw moment, a satisfactory agreement is achieved for all considered situations. The average percentage difference is 16% for F_x, 5% for F_y, 5% for M_z and 3% for Q_1 and thus the accuracy is comparable to the whole mathematical model, see Table 3.2.

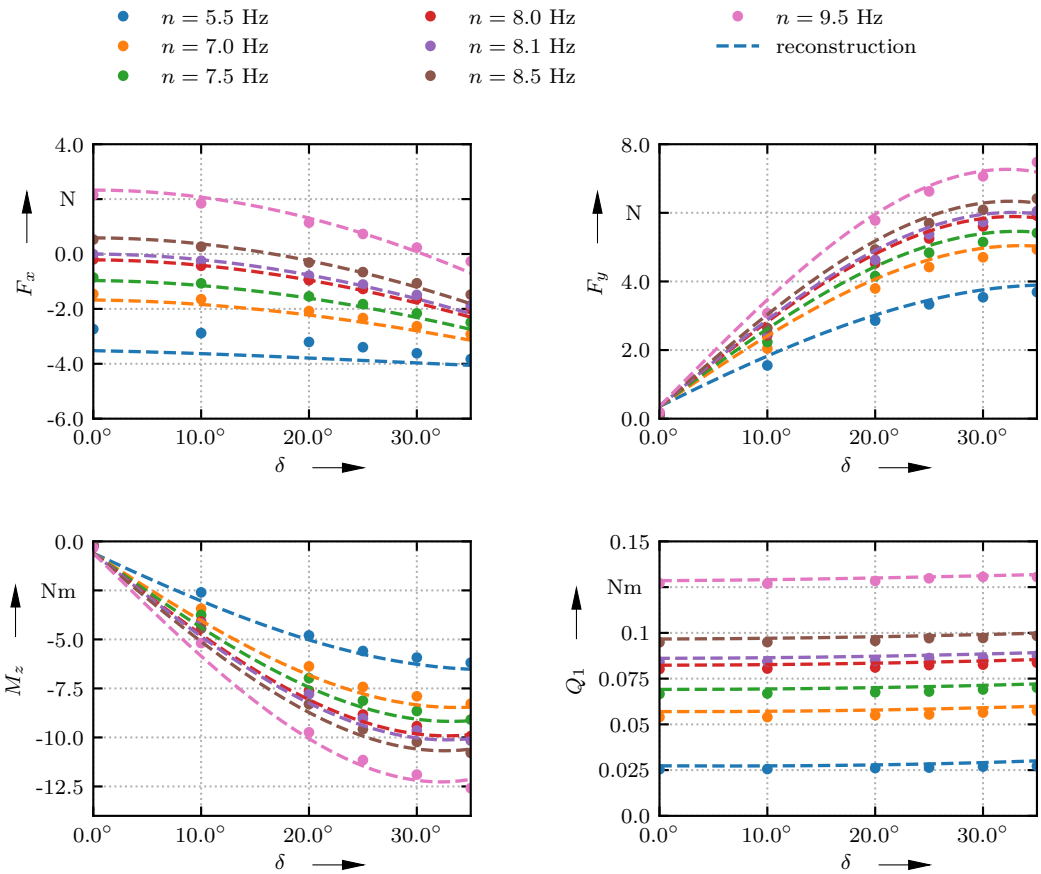

Figure 3.8.: Global side force due to rudder deflection at different propeller rates

3.2. Mean forces and moments on the S175 ship in waves

In this section the results of the computations for the ship in waves are presented and discussed. At first, the evaluation technique for obtaining the mean wave forces from the computed time histories is explained and the influence of the mean non hydrodynamic inertial forces is discussed. The results from selected computations are then validated using experimental data from Yasukawa et al. (2010) and Fujii and Takahashi (1975). Additional computations for the determination of the influence of forward speed, drift angle, wave amplitude and radius of gyration are presented and discussed. Finally a set of hydrodynamic wave force coefficients as described in Section 2.2.2 is obtained.

3.2.1. Evaluation Technique

Head wave

This section explains in detail how the computations have been evaluated using two representative cases. All other cases have been evaluated using the same procedure. The considered case is the S175 travelling at 15 knots in head waves with a non-dimensional wave length of $\lambda' = 1.2$ and a non-dimensional amplitude of $\zeta'_A = \zeta_A/L_{PP} = 0.012$. The ship is free to heave and pitch, the mean surge, sway and yaw motion is weakly prescribed using a virtual spring system as explained in Section 2.1.3. For selected computations an extended analysis, including an evaluation of the y^+ distribution on the hull, the spreading of the level set transition region and the wave quality, is included in Appendix B.3 together with a grid and timestep dependence analysis.

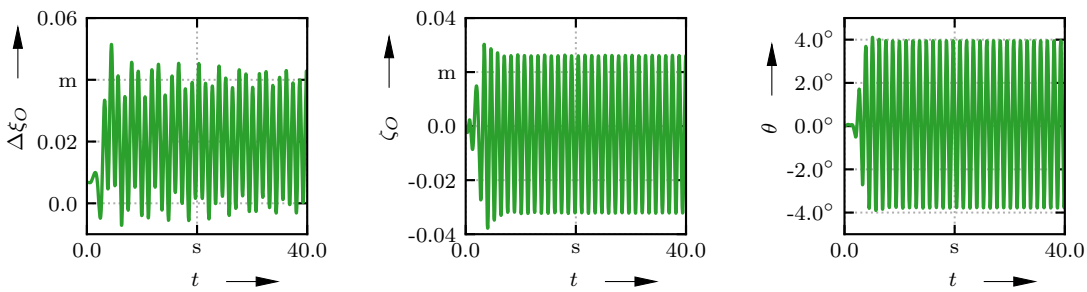

(a) surge motion (b) heave motion (c) pitch motion

Figure 3.9.: Computed motions for Fn = 0.15, $\lambda' = 1.2$, $\zeta'_A = 0.012$, $\alpha = 0°$

Figure 3.9 shows the surge, heave and pitch motion of the ship. In this case more than 30 wave periods have been computed to ensure a good convergence of the mean wave force. As can be seen, there is no significant change in the motion amplitudes after 10 s. Due to the relatively low stiffness of the springs employed and the weak damping in

longitudinal direction, the natural frequency of the system is visible as a superimposed second (lower) frequency in the surge motion.

The left side of Figure 3.10 shows the computed pure hydrodynamic force and its average, obtained by integration of pressure and shear stresses on the ship. The right side shows the restoring force added to the right hand side of the motion equation by the virtual spring system. In case of an experimental investigation of this case, this force would be equal to the measured force signal.

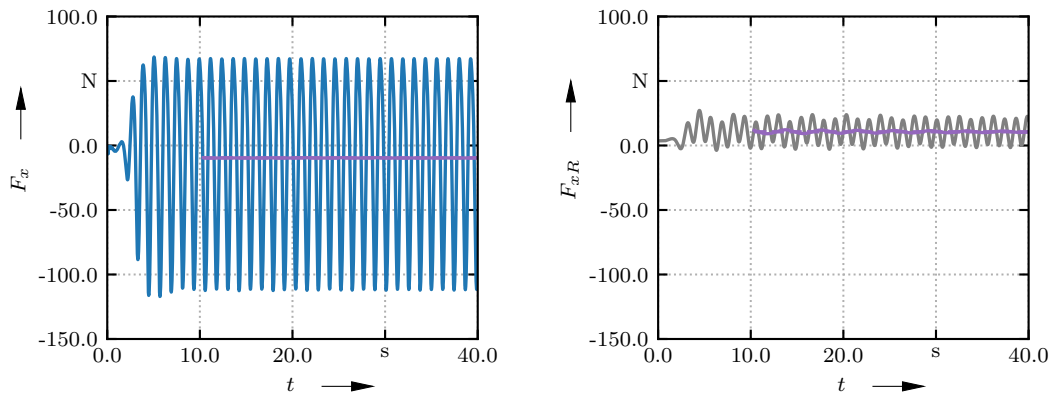

(a) pure hydrodynamic force

(b) virtual spring force

Figure 3.10.: Computed longitudinal force for Fn = 0.15, $\lambda' = 1.2$, $\zeta'_A = 0.012$, $\alpha = 0°$

To explain the difference between these forces, a detailed look at each individual term of the motion equation (2.9) is necessary. Since only head waves are considered, which means that there is almost no sway velocity ($v \approx 0$) and since the centre of gravity is at the centre plane ($y_G = 0$), some terms can be eliminated. The terms on the right hand side are the pure hydrodynamic force F_{xH} (from the direct integration of pressure and shear stresses), a contribution of the ships weight in longitudinal direction due to the pitch motion $F_{xW} = -\rho g \forall \sin\theta$ and the force applied by the virtual springs F_{xR}:

$$m\left[\dot{u} + \omega_2\, w - x_G\left(\omega_2^2 + \omega_3^2\right) + z_G\left(\dot{\omega}_2 + \omega_1\omega_3\right)\right] = F_{xH} + F_{xW} + F_{xR} \tag{3.1}$$

Figure 3.11 shows the contribution of each individual term of the motion equation over four wave periods. The time averaged values are shown in Table 3.4. It should be noted that the mean value of the left hand side is not zero, but needs to be considered, when computing the mean wave forces. Even though the left hand side is dominated by the term $m\,\dot{u}$, its mean value is not significant and in theory equal to zero. It can be seen on the other hand that the term $m\,\omega_2\,w$, which stems from the coupling of the heave and the pitch motion, has a significant influence. This fact is most often ignored, but has been also verified by simulations for a twin screw passenger ship (Uharek and Cura Hochbaum, 2018b), the DTC container ship (Cura Hochbaum and Uharek, 2016) and

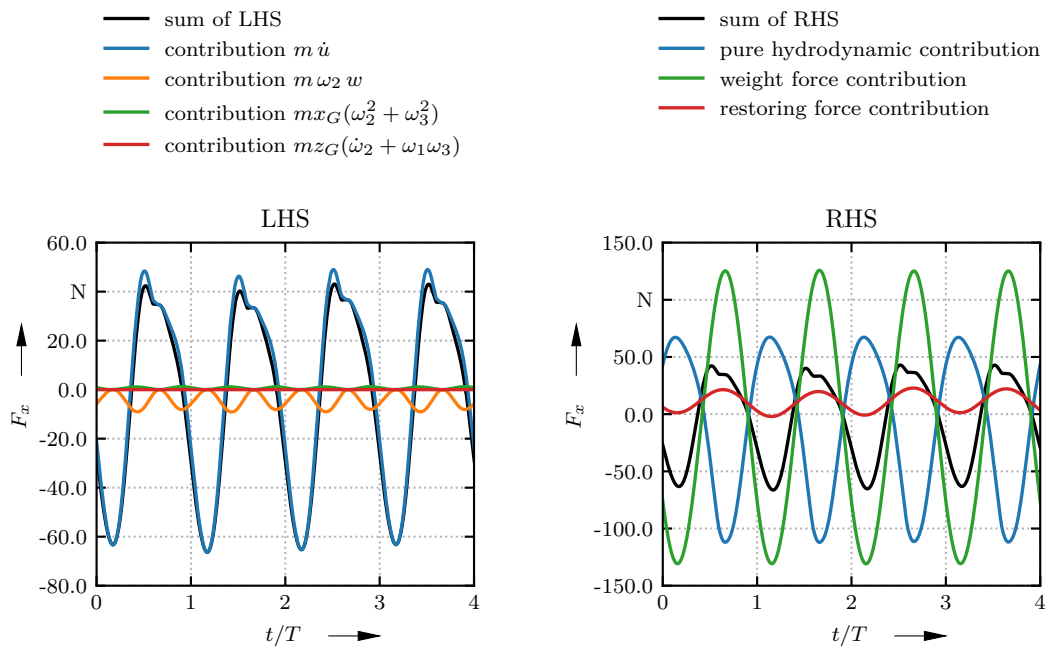

Figure 3.11.: Contributions to motion equation for a head wave

confirmed during experiments with a dedicated experimental device performed at the Technical University of Berlin (Lengwinat and Cura Hochbaum, 2018).

Since the heave and pitch motions – and all motions of first order due to waves – will be disregarded in the manoeuvring simulations, these 'mean inertial forces' need to be included in the mean force that is being modelled and used to simulate the manoeuvres. Figure 3.12 shows the final trace of the longitudinal force, including the weight contribution as well as all inertial contributions. Further a moving average over the last two wave periods is plotted, with a zoomed view on the right hand side of the figure. It can be seen that the mean value is not dependent on wave periods evaluated, but instead is very stable with a maximum variation of $\pm 1\%$ of the mean value. In diagrams containing mean wave forces, the maximum and minimum value of the moving average is shown as an error bar to depict the range of uncertainty.

Table 3.4.: Computed mean values of individual components of the motion equation

LHS		**RHS**	
$m\,\dot{u}$	$-0.03\,\mathrm{N}$	hydrodynamic force	$-9.63\,\mathrm{N}$
$m\,\omega_2\,w$	$-4.30\,\mathrm{N}$	weight force	$-4.73\,\mathrm{N}$
$m\,x_G\,(\omega_2^2+\omega_3^2)$	$0.60\,\mathrm{N}$	spring force	$10.62\,\mathrm{N}$
Total	$-3.74\,\mathrm{N}$		$-3.74\,\mathrm{N}$

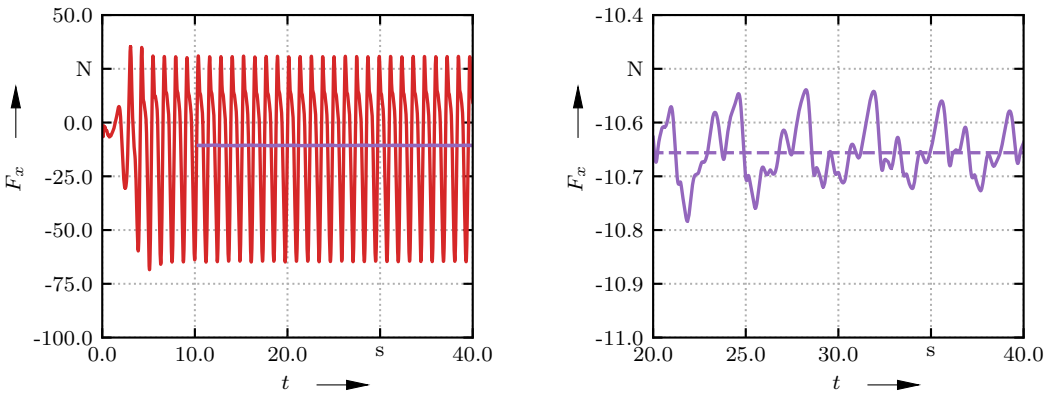

(a) timetrace of force

(b) zoom on the moving average

Figure 3.12.: Computed force in longitudinal direction with inertial terms for Fn = 0.15, $\lambda' = 1.2$, $\zeta'_A = 0.012$, $\alpha = 0°$

Oblique Wave

In case of oblique incoming waves, the motion equations for sway and yaw (2.9) need to be considered as well. Under the assumption that the centre of gravity is at the midship plane ($y_G = 0$) and the deviation moments are negligible ($I_{xy} \approx I_{yz} \approx I_{xz} \approx 0$) they read:

$$\begin{aligned} m\left[(\dot{v} - \omega_1\,w + \omega_3\,u) + x_G\,(\dot{\omega}_3 + \omega_1\omega_2) - z_G\,(\dot{\omega}_1 - \omega_2\omega_3)\right] &= F_{yH} + F_{yW} + F_{yR} \\ I_{zz}\dot{\omega}_3 - (I_{xx} - I_{yy})\,\omega_1\omega_2 + m\left[x_G\,(\dot{v} - \omega_1 w + \omega_3 u)\right] &= M_{zH} + M_{zW} + M_{zR} \end{aligned} \tag{3.2}$$

The contribution of non hydrodynamic inertial effects to the side force and yaw moment due to the weight force F_{yW} and M_{zW} is zero for the case of no roll and $y_G = 0$.

For oblique incoming waves there is another important effect when analysing the forces (from virtual as well as from real tests) for the determination of hydrodynamic coeffi-

cients. Since the motions are only weakly prescribed, the mean yaw moment due to the incoming wave leads to a change of the mean yaw angle, as shown in Figure 3.13 for an incoming beam wave. Since the ship is still pulled in its original direction by the attached springs, an oblique inflow results. This effect may be much more pronounced for other cases (especially to the mean side force and yaw moment) an must be subtracted from the mean forces.

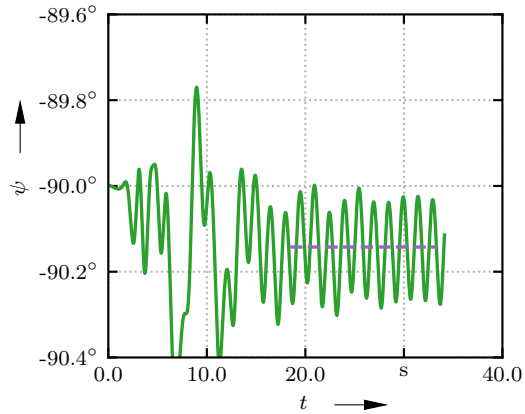

Figure 3.13.: Time history of yaw motion for Fn = 0.15, $\lambda' = 1.0$, $\zeta'_A = 0.01$, $\alpha = 90°$

To remove this contribution, the side force and yaw moment due to the oblique inflow condition are determined using the calm water hydrodynamic coefficient set and subtracted from the computed mean values. This correction is based on the assumption, that the mean side force and yaw moment due to the oblique inflow condition is not significantly affected by the heave and pitch motion of the ship. This assumption is required anyway for all subsequent manoeuvre simulations and seems reasonable, since the average value of these motions is rather small.

In addition, this mean yaw angle changes the encounter angle α. Since the used Fourier analysis required equidistant α values and the changes are relatively small with a maximum of 0.5° and an average of 0.1°, this second effect has been neglected in the Fourier analysis.

Figure 3.14 shows the contributions for the case of the S175 ship travelling with Fn=0.15 in beam waves from starboard ($\alpha = 90°$) of $\lambda' = 1.0$ and $\zeta'_A = 0.01$. Due to the sway motion of the ship the amplitudes of the oblique flow contributions to side force and yaw moment are large, but the resulting mean value only stems from the mean drift angle.

In this case, no significant inertial contribution was observed in the mean side force and yaw moment. The contribution due to the unwanted oblique inflow condition to the side force was however $-0.22\,\mathrm{N}$, which is equal to 23% of the hydrodynamic force and $-0.24\,\mathrm{Nm}$ (10%) to the mean yaw moment.

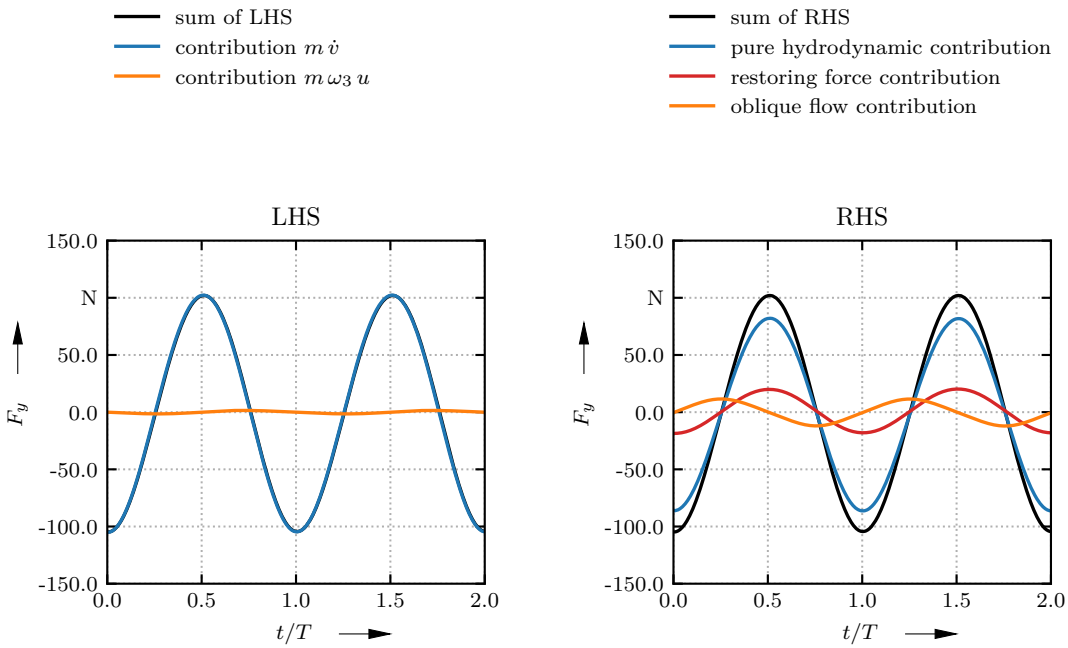

(a) sway

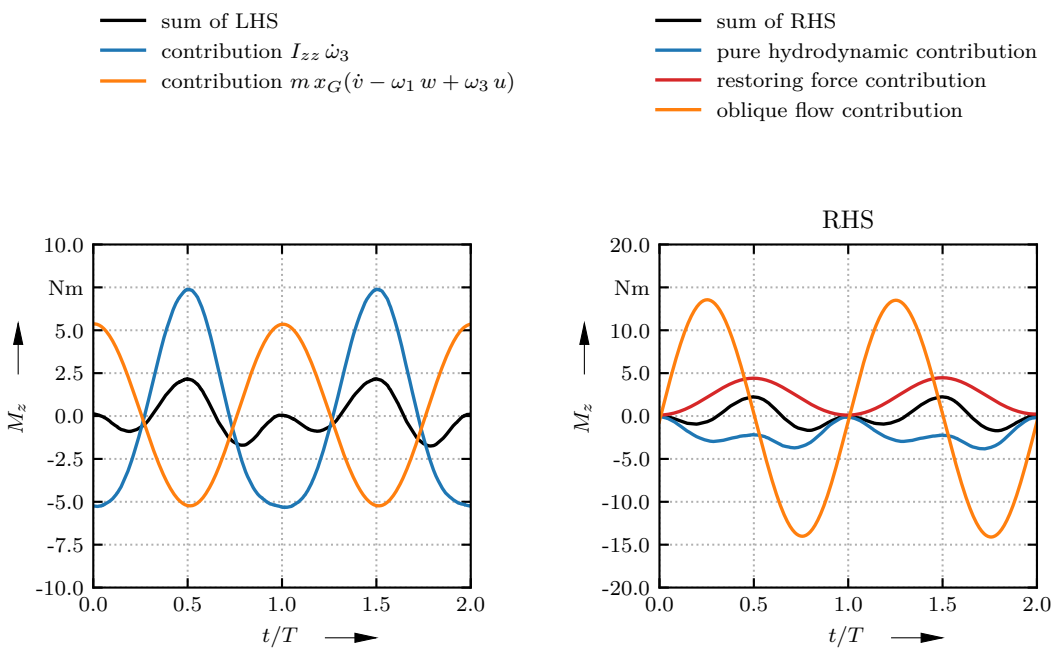

(b) yaw

Figure 3.14.: Contributions to motion equations for a beam wave

In Figure 3.15 the wave patterns for an oblique incoming wave with an encounter angle of $\alpha = 45°$ are shown for two different wave lengths and three different Froude numbers, where green indicates a wave crest and blue a wave trough. As expected, a significant change of the disturbed wave system at the bow of the ship can be seen for the different forward speeds considered. In short waves (left hand side), a strong reflection of the incoming wave at the ship can be observed. This reflection results in a pronounced wave pattern at the windward side, whereas on the leeward side the shadow of the ship can be seen. In longer waves (right hand side), radiation effects are clearly visible and influence the wave pattern on the leeward side. For slow forward speeds, the radiation waves propagate upstream. Yasukawa et al. (2018) stated, that the upstream propagation occurs for cases with $\tau = u\,\omega_e/g < 1/4$, which agrees with the findings in this work. The values of τ in the captions of Figure 3.15 are time averaged values.

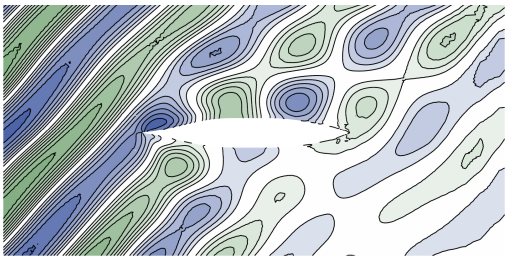

(a) Fn 0.05, $\lambda' = 0.5$, $\tau = 0.20$

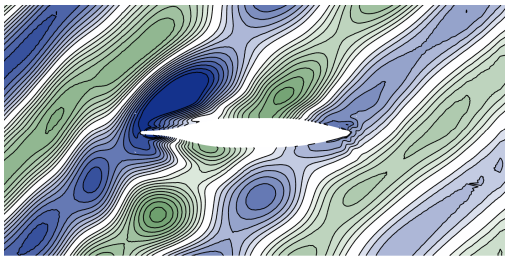

(b) Fn 0.05, $\lambda' = 0.7$, $\tau = 0.17$

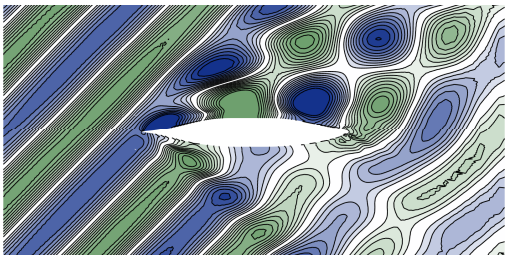

(c) Fn 0.1, $\lambda' = 0.5$, $\tau = 0.44$

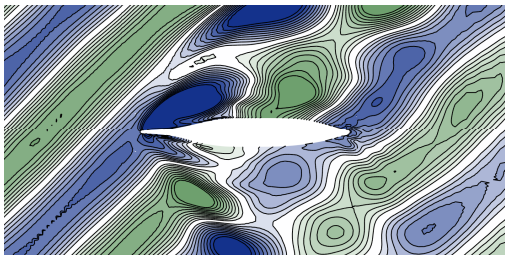

(d) Fn 0.1, $\lambda' = 0.7$, $\tau = 0.36$

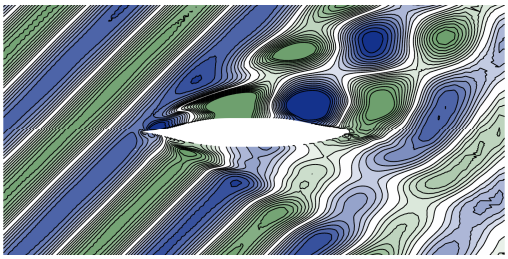

(e) Fn 0.15, $\lambda' = 0.5$, $\tau = 0.73$

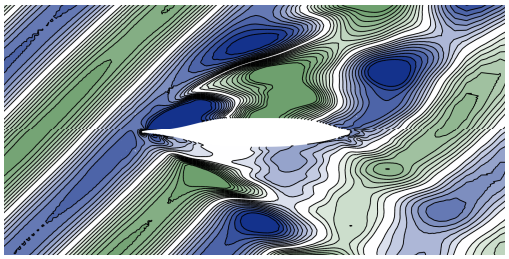

(f) Fn 0.15, $\lambda' = 0.7$, $\tau = 0.59$

Figure 3.15.: Wave patterns for an oblique wave with $\alpha = 45°$ and $\zeta'_A = 0.01$

3.2.2. Validation

The computational setup was validated using experiments performed by Yasukawa and Adnan (2006) and Yasukawa et al. (2010). As described in Section 2.1.3, the numerical simulations resemble their experimental setup. The computed wave length was in the range of $\lambda' = 0.5$ to 1.5, the wave steepness was constant at $H/L_{PP} = 0.02$.

Figure 3.16 shows the computed non dimensional added resistance on the left and the absolute value (or modulus) of the heave and pitch response amplitude operators (RAOs) on the right side. The RAO is a frequency dependent complex function, which is defined as quotient of the motion response of the ship θ or ζ_G and the amplitude of the incoming wave ζ_A. Note that the pitch RAO is divided by the wave slope $k\zeta_A$ in order to obtain non-dimensional values. The green traces show the pure hydrodynamic forces and the red traces are obtained by adding the mean non hydrodynamic inertial forces. As can be seen, the agreement between computed and measured mean wave forces is very satisfactory, after inertial effects are taken into account. The pitch RAO shows a very good agreement as well. No explanation was found yet for the differences observed in the RAO for the heave motion.

The results of the validation computations in beam seas from starboard compared to the measured values are shown in Figure 3.17. The unwanted contributions due to the oblique inflow have been subtracted from the side force and the yaw moment. After the correction, a satisfactory agreement can be seen for both. It should be noted that the disagreement in the longitudinal force for longer waves is relatively large, but the absolute values are rather small – especially when being compared to the mean longitudinal force in head waves.

For the validation of the oblique incoming waves, experimental data from Fujii and Takahashi (1975) is used. It should be noted, that the radius of gyration about the transverse axis of the ship in this experiments was $i_{yy}/L_{PP} = 0.24$ and therefore the results are not comparable to those obtained by Yasukawa. Fujii only measured the longitudinal force F_x and thus no comparison for the side force and yaw moment is possible. Unfortunately no details on the used measurement device (for example the used spring stiffness) are available and therefore the setup from Yasukawa was used. The results of these computations are shown in Figure 3.18. A satisfactory agreement can be observed for most of the considered cases.

Also in this case the comparison is only correct after the inertial effects are taken into account. In this case, a satisfactory agreement is achieved in general. One exception is the beam wave case, for which the difference can not be explained. It should be noted though that even for this case there is a significant inertial effect due to the coupled heave and pitch motion.

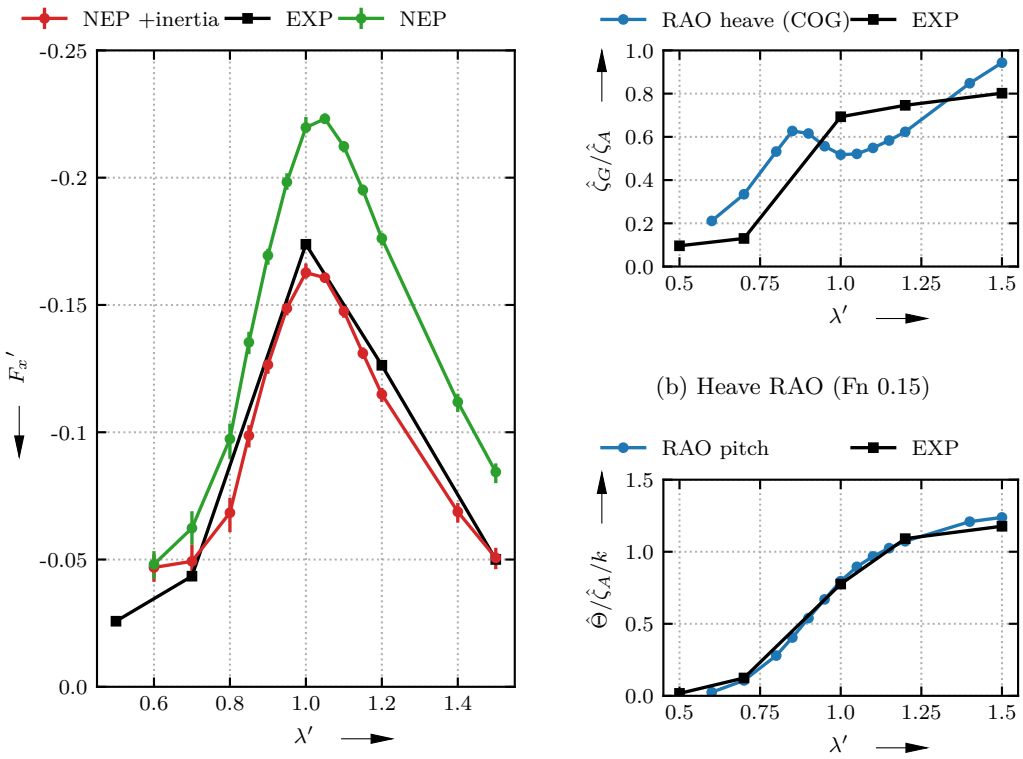

(a) Added resistance (Fn 0.15)

(b) Heave RAO (Fn 0.15)

(c) Pitch RAO (Fn 0.15)

Figure 3.16.: Results for head wave case compared with experimental data from Yasukawa and Adnan (2006)

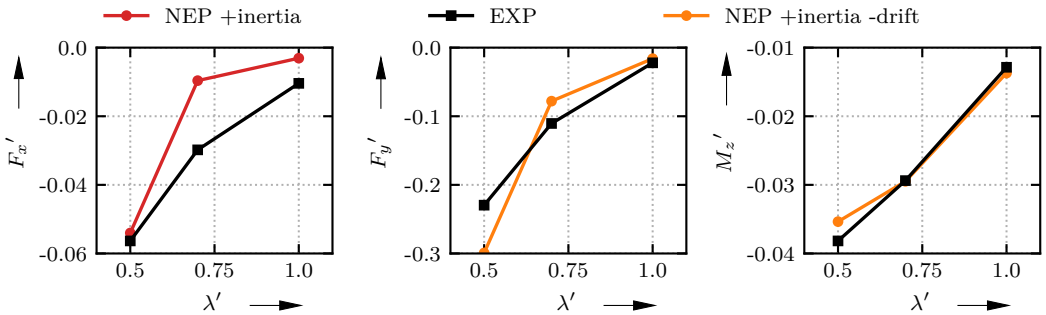

Figure 3.17.: Results for beam wave case compared with experimental data from Yasukawa and Adnan (2006)

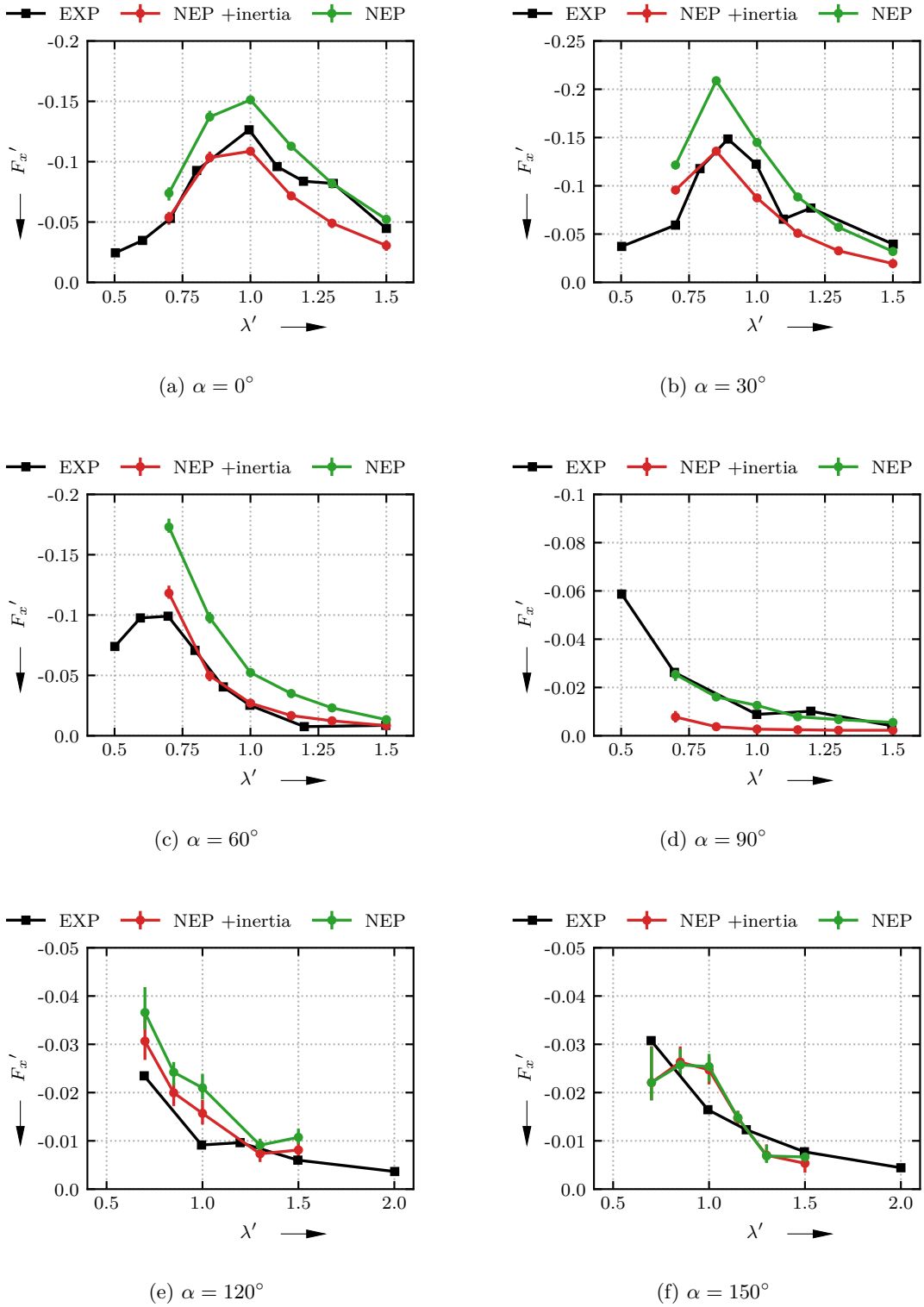

(a) $\alpha = 0°$

(b) $\alpha = 30°$

(c) $\alpha = 60°$

(d) $\alpha = 90°$

(e) $\alpha = 120°$

(f) $\alpha = 150°$

Figure 3.18.: Results for head and beam wave cases compared to experimental data from Fujii and Takahashi (1975)

3.2.3. Influence of wave steepness

In order to check the dependence of mean wave forces on the wave amplitude, the computations have been performed for different wave steepness (H/λ) values. The results of these computations are shown in Figures 3.19 and 3.20. The mean forces were made non-dimensional using the squared wave amplitude as in (2.36). Therefore, if the mean wave forces would be dependent on the squared wave amplitude, the value should be constant for a given wave steepness.

It can be observed that in the case of head waves, this is in fact the case for waves with $\lambda' = 0.5$ and 0.7. For $\lambda' = 1.0$ however, the quadratic dependence is not given. This effect was already observed in the past, see for example Sibul (1971); Nakamura and Naito (1977); Lengwinat and Cura Hochbaum (2018).

In oblique incoming waves a significant influence of the wave steepness on the non-dimensional mean side force and mean yaw moment can be observed especially in shorter waves. For some cases, e.g. $\lambda' = 0.5$ and $\alpha = 30°$, even though a quadratic dependence of the mean longitudinal force on the wave amplitude is clearly visible, the mean side force shows a completely different trend.

This observations lead to the conclusion, that in general it is necessary to consider the correct wave steepness when computing the coefficients for the mean wave forces. However, it should be kept in mind that in this case both numerical and model errors play a role, and especially for smaller waves the non-dimensional forces are extremely sensitive to a change in the wave amplitude, which is nearly inevitable due to numerical errors.

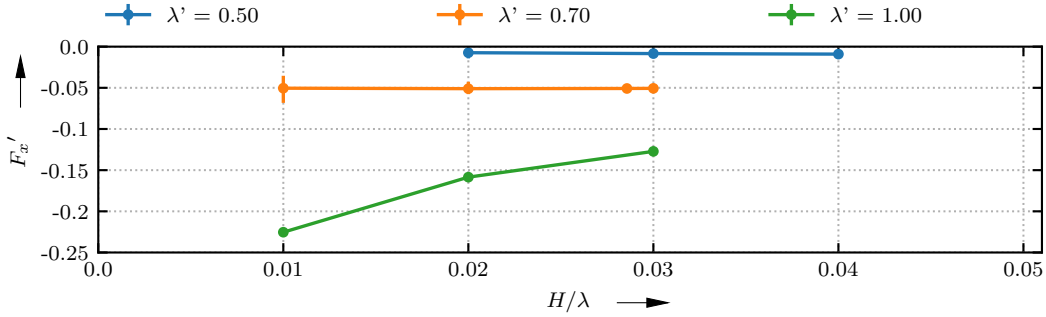

(a) $\alpha = 0°$

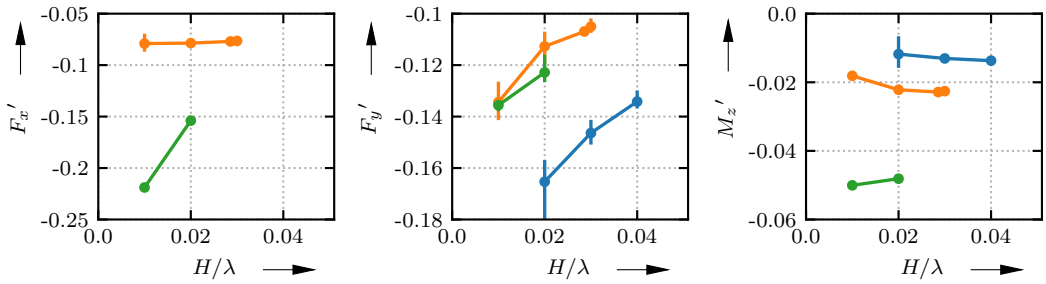

(b) $\alpha = 30°$

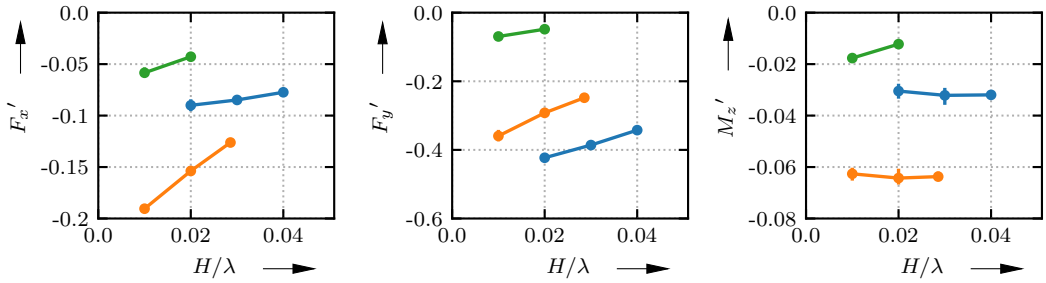

(c) $\alpha = 60°$

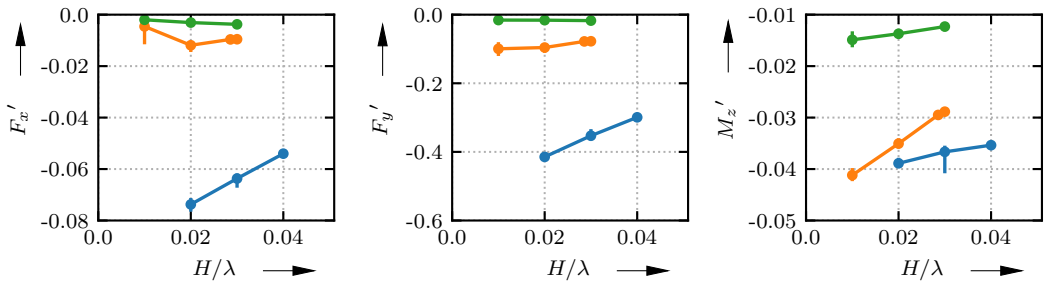

(d) $\alpha = 90°$

Figure 3.19.: Influence of wave amplitude on mean wave forces and yaw moment

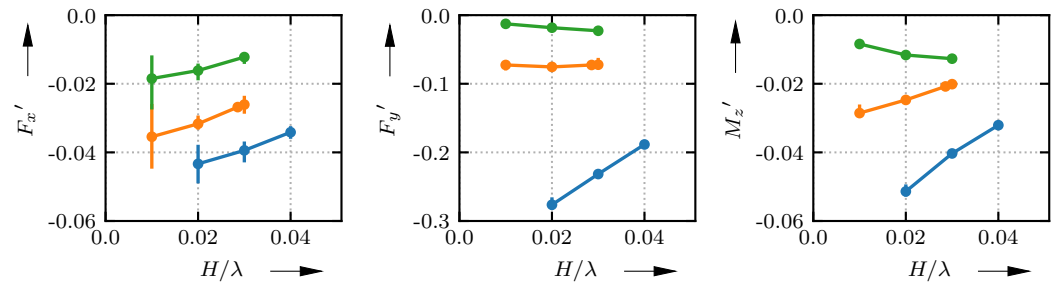

(a) $\alpha = 120°$

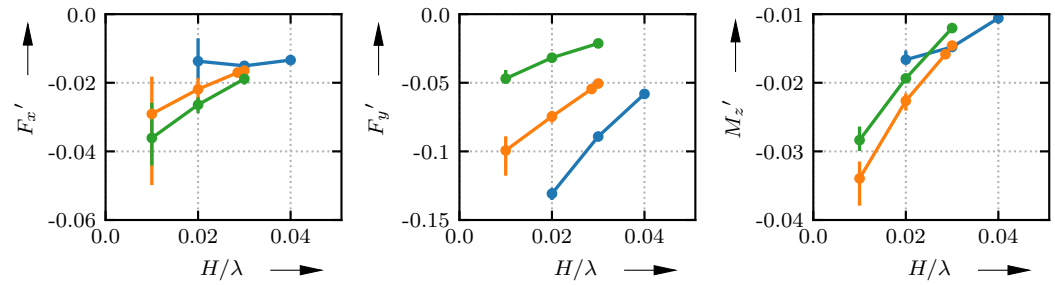

(b) $\alpha = 150°$

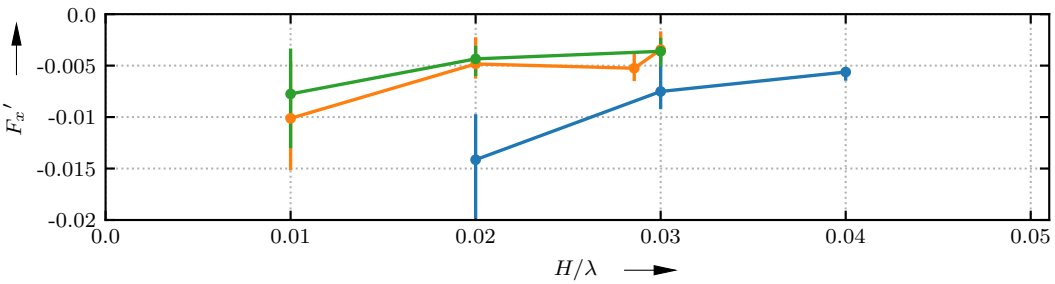

(c) $\alpha = 180°$

Figure 3.20.: Influence of wave amplitude on mean wave forces and yaw moment

3.2.4. Influence of drift motion

Computations were performed to analyse the influence of the drift angle on the mean wave forces. The simulations were performed with mean drift angles of 5° and 10° to port and starboard, see Figure 3.21. Head and beam waves with a non-dimensional wave length of $\lambda' = 0.5, 0.7$ and 1.0 were considered.

The results are shown in Figure 3.22 for head waves and 3.23 for beam waves. The black symbols are the measured values from Yasukawa and Adnan (2006) and the red symbols the computed values. The dotted grey lines show the forces in calm water and the orange line is the corrected mean wave force after subtraction of the calm water force for the given drift angle.

Ideally – in case of no interaction between calm water and mean wave forces – the orange line should be constant over β. As can be seen, this is not always the case. In beam waves a moderate coupling between wave and drift angle dependent forces is visible, but in short waves, the results deteriorate significantly, even though the effect is slightly overestimated by the numerical computations.

It can thus be stated that the current model is expected to yield slightly inaccurate results in the case of high drift angles and the introduction of drift angle dependent coefficients to the wave force model could improve this in a future work. It should be noted though that capturing these effects would increase the computational time considerably.

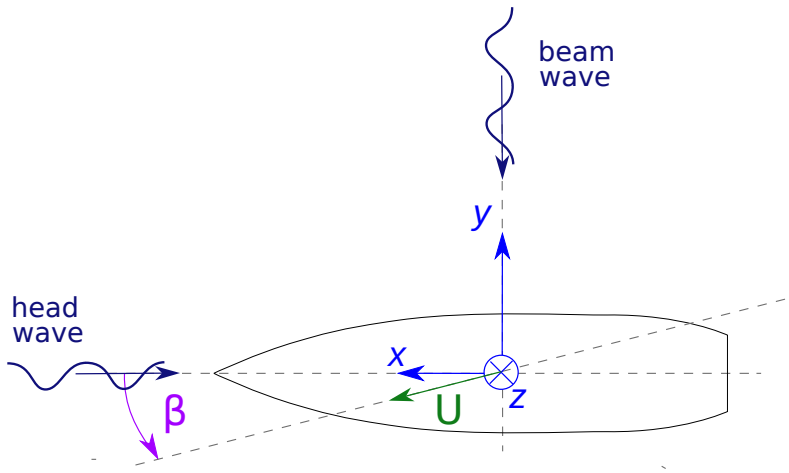

Figure 3.21.: Setup for computations in incoming waves combined with a drift motion

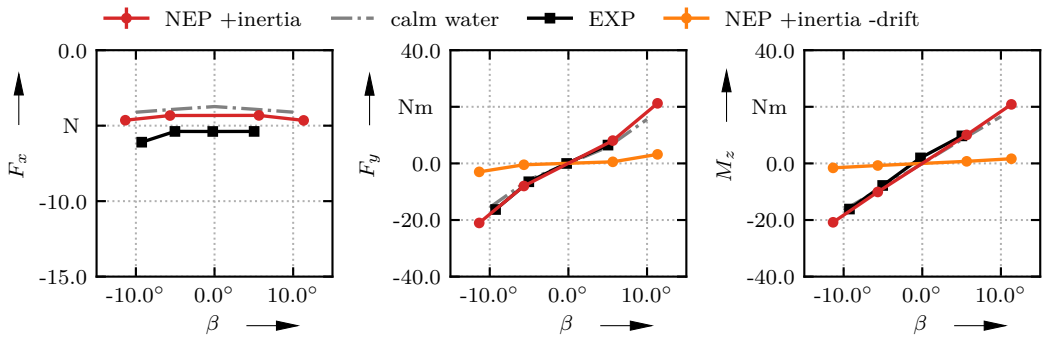

(a) $\lambda' = 0.5$

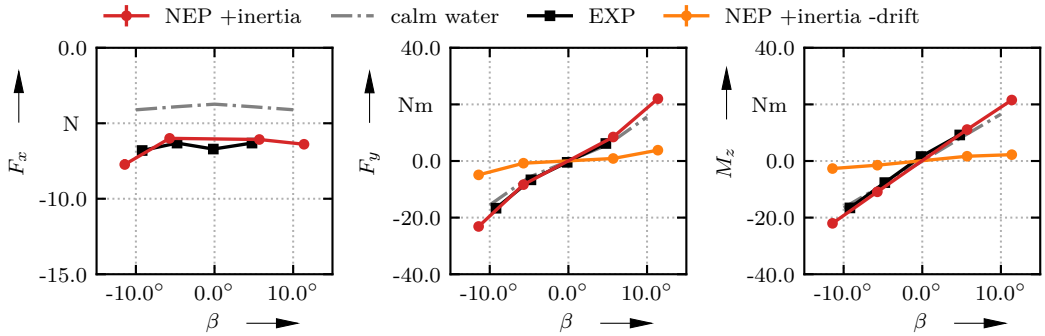

(b) $\lambda' = 0.7$

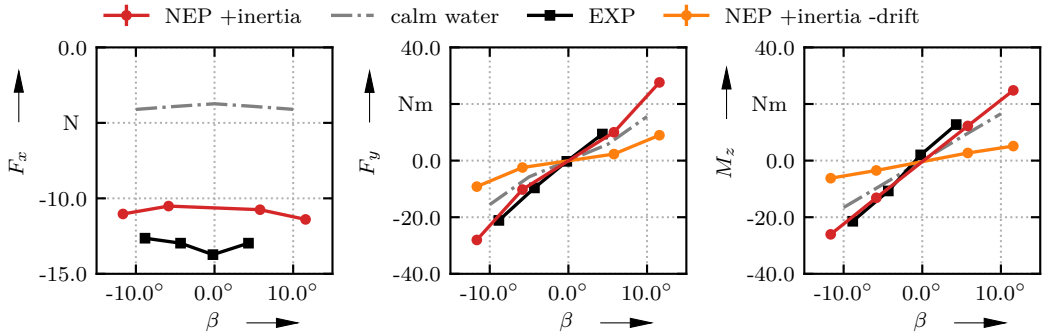

(c) $\lambda' = 1.0$

Figure 3.22.: Influence of drift angle on mean forces for head waves ($\alpha = 0°$) compared to experimental data from Yasukawa and Adnan (2006)

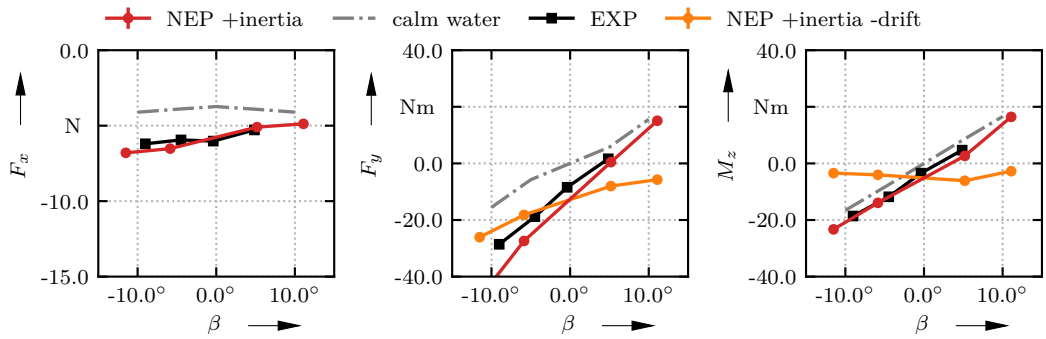

(a) $\lambda' = 0.5$

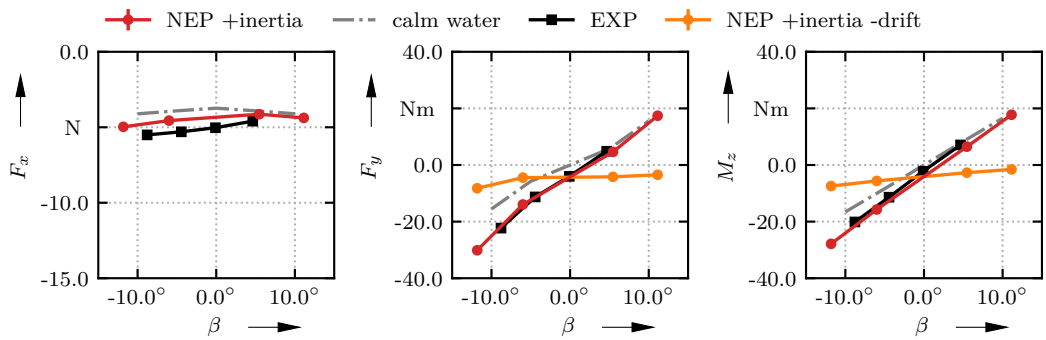

(b) $\lambda' = 0.7$

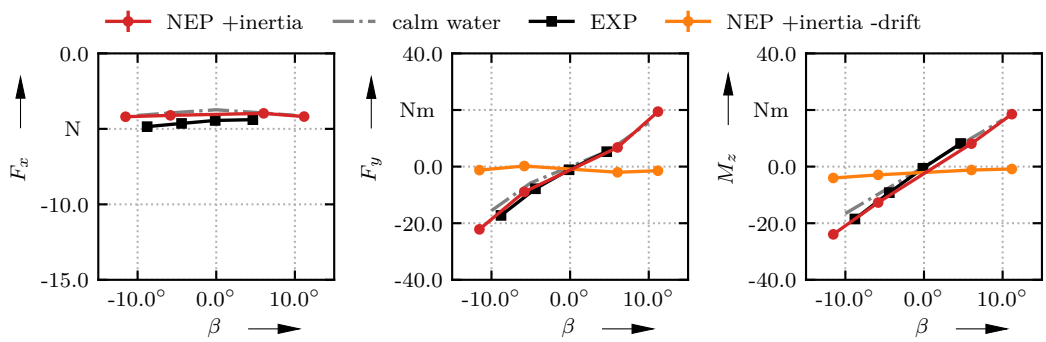

(c) $\lambda' = 1.0$

Figure 3.23.: Influence of drift angle on mean forces for beam waves ($\alpha = 90°$) compared to experimental data from Yasukawa and Adnan (2006)

3.2.5. Influence of radius of gyration

To investigate the influence of the radius of gyration r_{yy} about the transverse axis of the ship on the mean wave forces, computations with $r_{yy}/L_{PP} = 0.235, 0.258$ and 0.278 (leading to $I'_{yy} = 2.5 \cdot 10^{-4}, 3 \cdot 10^{-4}$ and $3.5 \cdot 10^{-4}$) are performed. The results are shown in Figure 3.24. The absolute values (or modulus) of the heave and pitch RAO are rather similar for all three considered values of r_{yy}, whereas the added resistance strongly varies for each value. It is clearly shown, that the accurate determination of r_{yy} is essential when performing model tests. If this strong dependency is observed for other ships as well, it could be a profitable way to significantly reduce the fuel consumption of ships in waves.

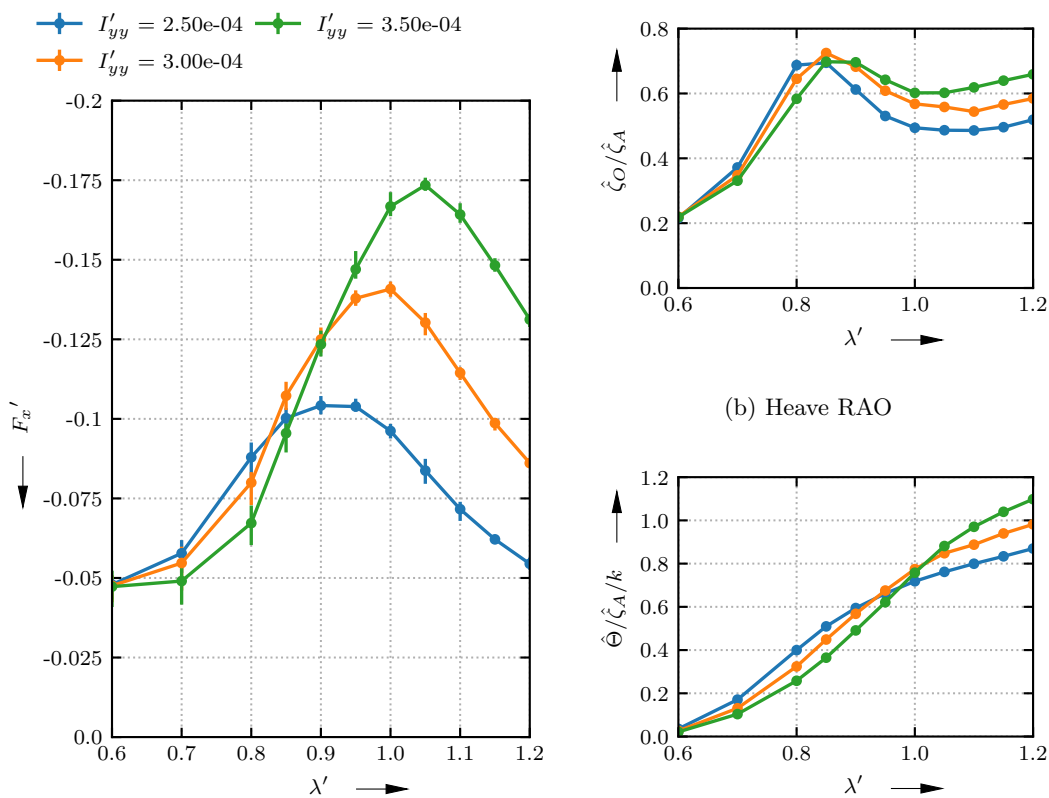

(a) Added resistance

(b) Heave RAO

(c) Pitch RAO

Figure 3.24.: Influence of gyration radius on added resistance

3.2.6. Wave force mathematical model

In order to determine the coefficients of the mathematical model for the mean wave forces as described in Section 2.2.2 a total of 228 RANS computations have been performed.

The mean wave forces have been computed for 13 wave encounter angles α ranging from $0°$ to $180°$ and three different non-dimensional wave lengths of $\lambda' = 0.5, 0.7$ and 1.0 each. The considered non-dimensional wave amplitude was $\zeta'_A = 0.01$, which is the same as the one used in the free running turning circle tests used for validation. To capture the influence of forward speed on mean wave forces, these simulations were performed for the Froude numbers 0.05, 0.075, 0.1 and 0.15. For the Froude number of 0.075 the number of computed encounter angles was increased to 37.

After all computations are evaluated, the coefficients of the mathematical model can be determined. Figures 3.25, 3.26 and 3.27 show the computed mean wave forces as symbols and the reconstructions of the mathematical model as lines for all four considered Froude numbers. As can be seen, the model is able to capture all the traces quite well with some minor deviations.

For the validation of the interpolation capabilities of the mathematical model, computations at a forward speed corresponding to a Froude number of 0.15 are performed for additional wave lengths and angles, which were chosen to be different from the ones used for the determination of the coefficients of the model. The comparison between the computed mean forces and the values obtained by the mathematical model are shown in Table 3.5. Even though for some situations relative differences of up to 30 % occur, the general agreement is quite satisfactory as can be seen in Figure 3.28. The largest discrepancies occur in the mean longitudinal force for longer waves in bow quartering waves ($\alpha = 23.8°$) and in the mean yaw moment at a slightly larger wave encounter angle of $\alpha = 49.3°$. However it should be kept in mind that these situations are the most complex for the model to handle, since interpolation is required in both wave length and direction with only three wave lengths used as input for coefficient set. The results could be further improved by considering more situations for the determination of the coefficients.

Table 3.5.: Validation of wave force model

		simulation			model			deviation		
λ'	α	F_x	F_y	M_z	F_x	F_y	M_z	F_x	F_y	M_z
	°	N	N	Nm	N	N	Nm	N	N	Nm
0.65	23.8	−1.8	−3.5	−2.2	−2.3	−3.4	−2.2	0.5	0.0	0.0
0.65	72.0	−2.5	−8.3	−7.2	−3.2	−9.8	−7.5	0.7	1.5	0.4
0.80	0.0	−2.9	−0.2	−0.2	−3.0	0.0	0.0	0.1		
0.85	0.0	−4.0	−0.1	−0.1	−3.8	0.0	0.0	−0.2		
0.85	23.8	−6.2	−3.6	−3.7	−4.6	−3.5	−4.1	−1.6	−0.1	0.4
0.85	49.3	−5.0	−7.3	−9.9	−5.3	−6.8	−7.6	0.3	−0.5	−2.4
0.90	23.8	−7.1	−4.2	−5.0	−5.3	−3.7	−4.8	−1.8	−0.5	−0.3
0.90	49.3	−7.1	−6.1	−8.5	−4.9	−5.9	−6.9	−2.2	−0.2	−1.6

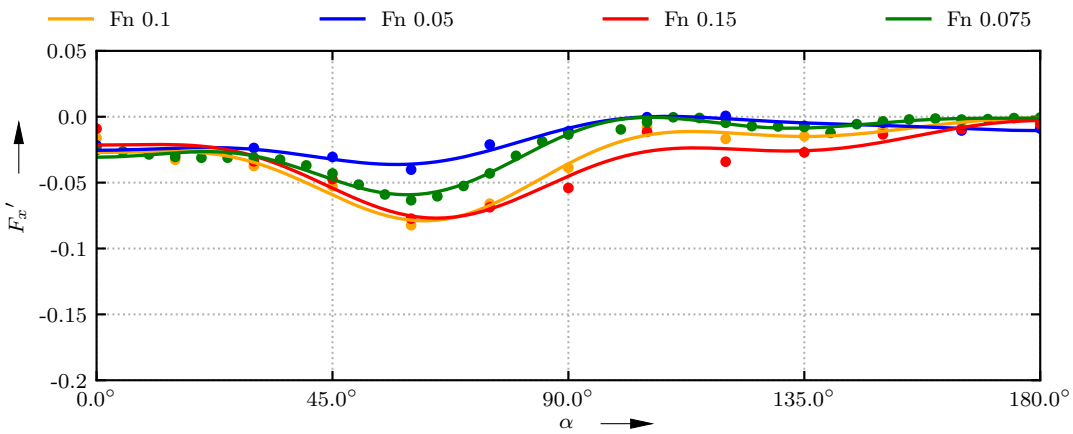

(a) $\lambda' = 0.5$

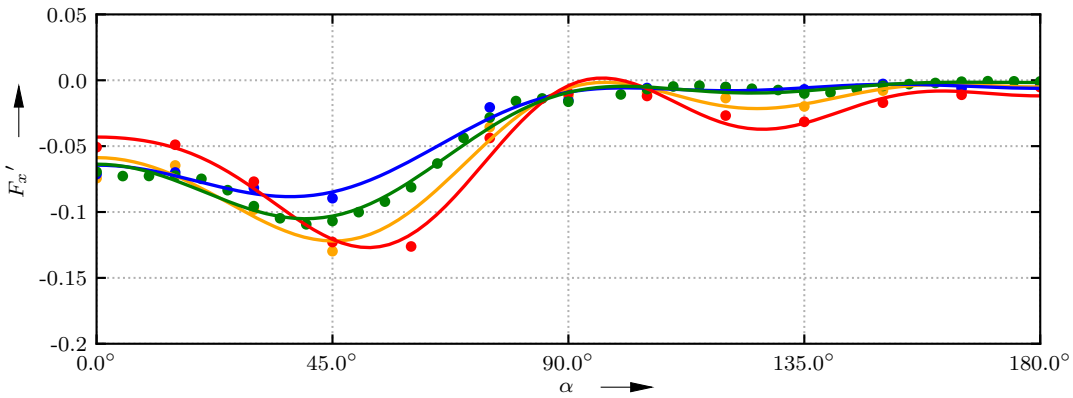

(b) $\lambda' = 0.7$

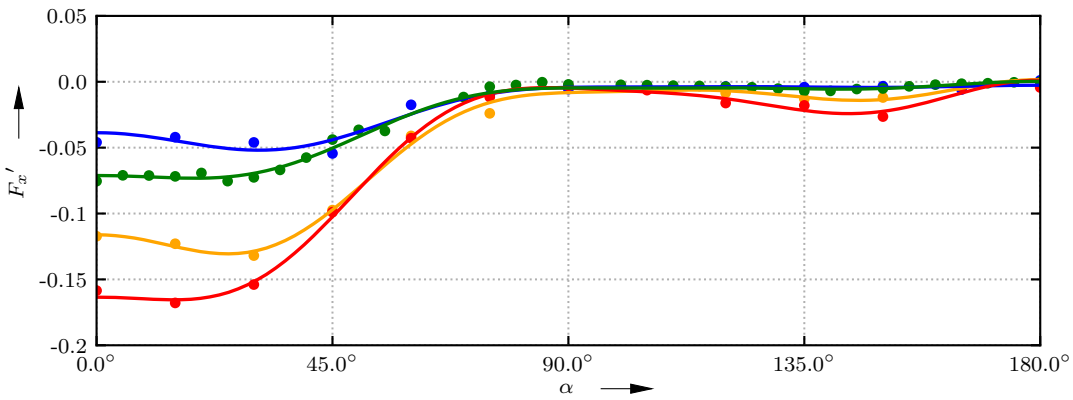

(c) $\lambda' = 1.0$

Figure 3.25.: Reconstruction of mean longitudinal force in waves

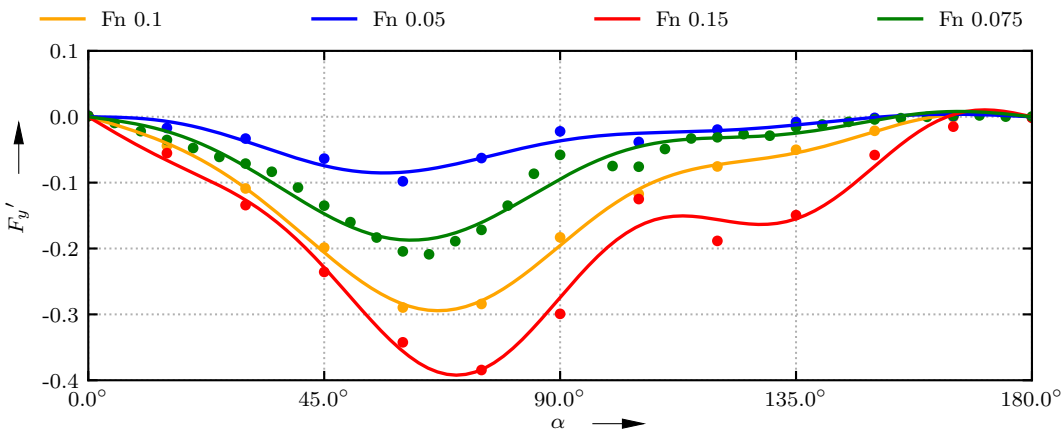

(a) $\lambda' = 0.5$

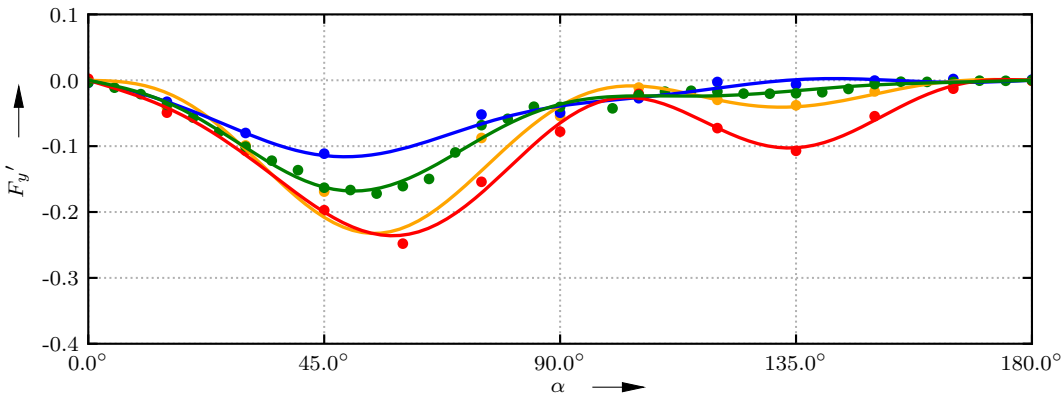

(b) $\lambda' = 0.7$

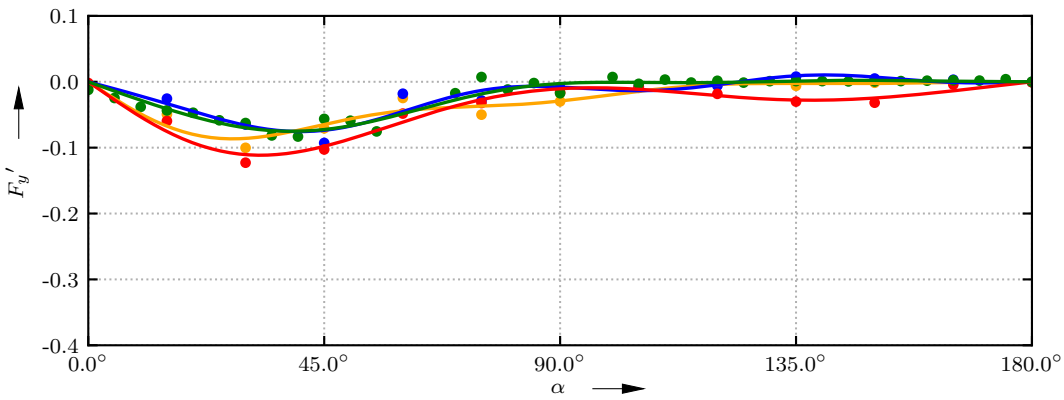

(c) $\lambda' = 1.0$

Figure 3.26.: Reconstruction of mean side forces in waves

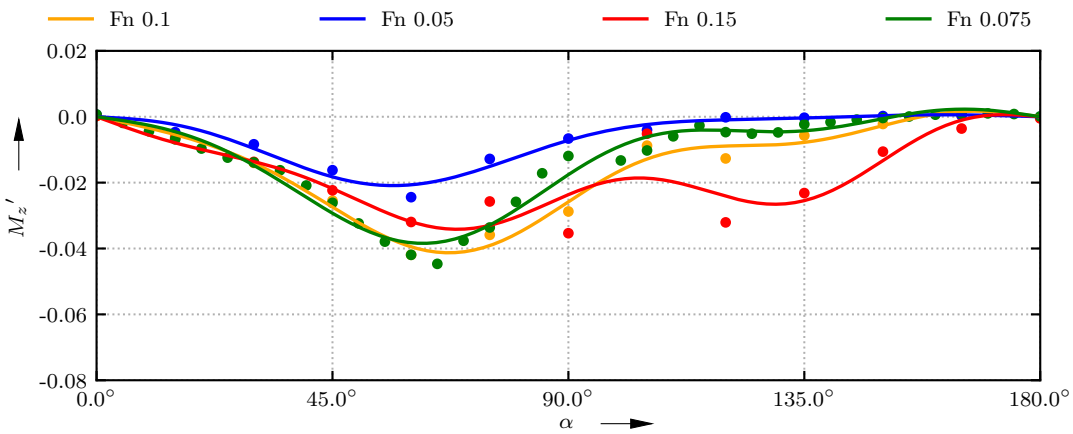

(a) $\lambda' = 0.5$

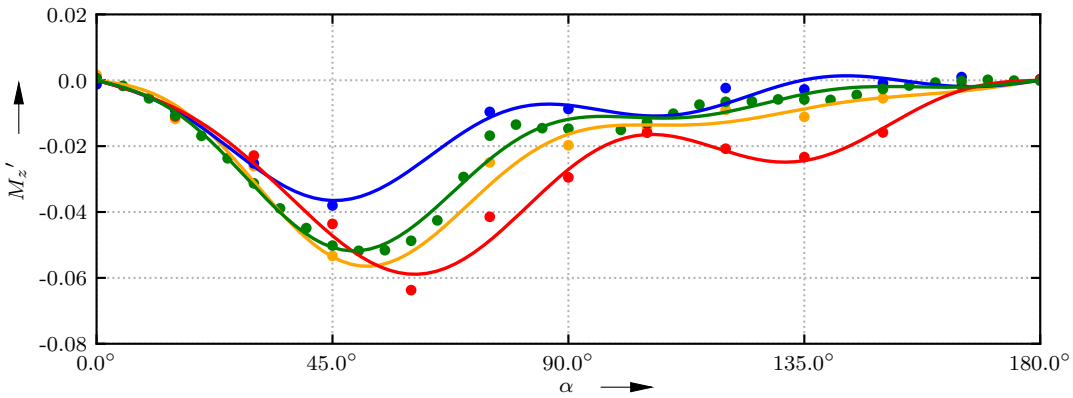

(b) $\lambda' = 0.7$

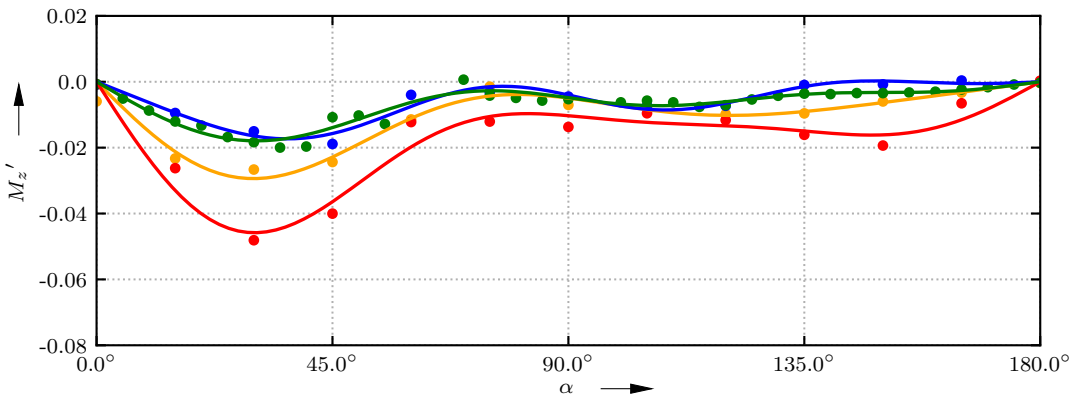

(c) $\lambda' = 1.0$

Figure 3.27.: Reconstruction of mean yaw moment in waves

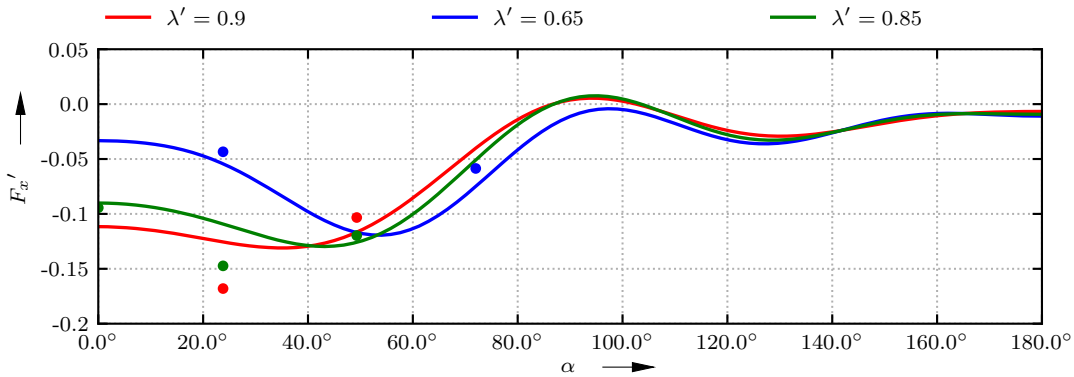

(a) Mean longitudinal force

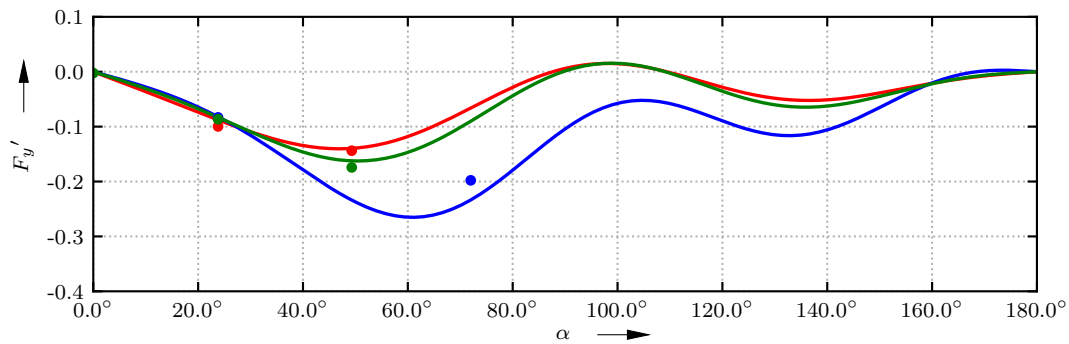

(b) Mean side force

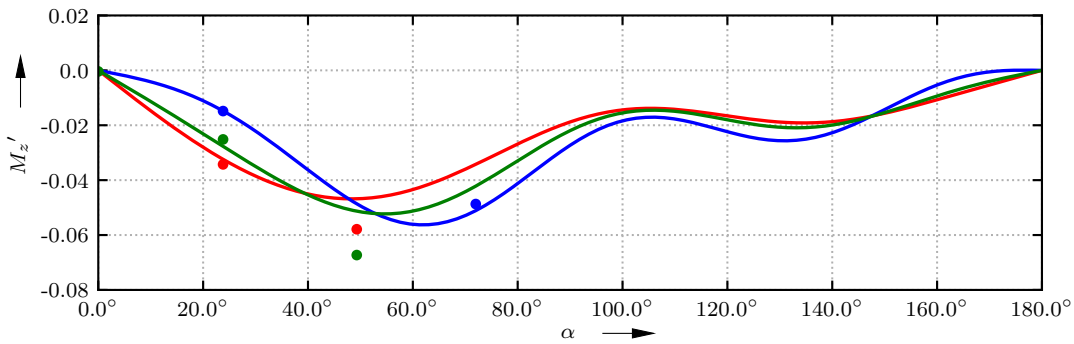

(c) Mean yaw moment

Figure 3.28.: Validation of wave force mathematical model

3.3. Manoeuvring and Power Prediction

This chapter presents the results of simulated rudder manoeuvres in calm water and waves. The results are compared to the experimental data from Yasukawa (2006); Yasukawa and Nakayama (2009). All numerical results are obtained in the scope of this work, some were are already published in Uharek and Cura Hochbaum (2018a).

3.3.1. Calm Water

Turning circle In order to check the accuracy of the determined hydrodynamic coefficients in calm water, turning circle tests with 35° rudder deflection to port and starboard are simulated, resembling the experiments from Yasukawa and Nakayama (2009). The results are shown in Figure 3.29 and Table 3.6. The first plot shows the forward speed u during the manoeuvre divided by the approach speed $u_0 = 0.879\,\mathrm{m/s}$. The results of the simulation is shown in blue, the raw data of the measurement in grey and low-pass filtered results of the measurements in red. Due to the settling time of the filter, the first seconds of the filtered data need to be disregarded. The second plot displays the drift angle β and the third plot shows the increase in the propeller torque ΔQ compared to the torque during the approach in percent. The dots on the trajectories mark a time interval of 20 s.

The evaluated parameters of the turning circle are the longitudinal and transversal displacement of the ship at the point of a 90° heading change, called advance X_{90} and transfer Y_{90}, and the transversal displacement of the ship at the point of a 180° heading change, called tactical diameter Y_{180}, as well as the corresponding times t_{90} and t_{180}, which are shown in Table 3.6.

The results are well within the limits set by the International Maritime Organisation (2002), which states that the advance should not exceed 4.5 L_{PP} and the tactical diameter is required to be less than 5 L_{PP}, although the helm rate of 12 °/s in model scale is equal to 1.7 °/s in full scale, which is less than the helm rate of 2.32 °/s required by most classification societies, see for example Det Norske Veritas (2011).

The predicted propeller torque increase during the manoeuvre is 26 % of the approach torque and is in good agreement with the experiments. Since the considered ship is a benchmark ship only, no details on the engine are available and no statements can be made if the engine power is sufficient to maintain the initial propeller revolution rate.

Son and Nomoto (1981) have performed an experimental analysis of the influence of heel on the manoeuvring derivatives for a condition with 1 m trim to the stern and a draft of 8.5 m. They also performed simulations of turning circle tests for that condition with different $\overline{GM}$ values and showed that results obtained with consideration of the roll motion are different to the ones obtained without consideration of roll motion. However, the manoeuvres were performed at a higher approach speed and for lower $\overline{GM}$ values than considered here and the good agreement with the experiments confirm the assumption, that the effect of roll is negligible in the present case.

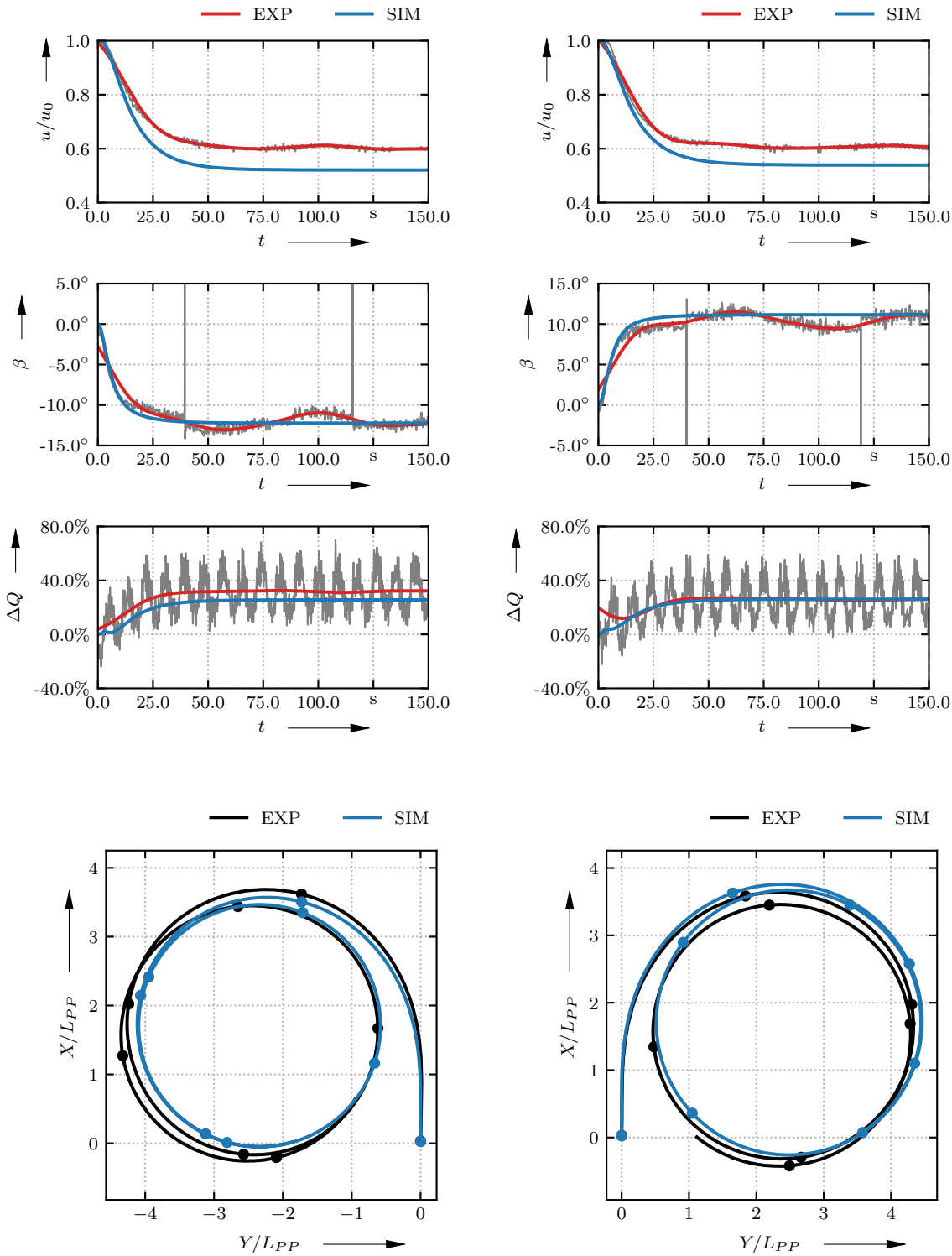

(a) Port

(b) Starboard

Figure 3.29.: Turning circle for S175 in calm water compared to experimental data from Yasukawa and Nakayama (2009)

Table 3.6.: Results of turning circle tests in calm water compared to experimental data from Yasukawa and Nakayama (2009)

	Port				Starboard		
	SIM	EXP	DIFF		SIM	EXP	DIFF
t_{90}	21 s	21 s	−1 %	t_{90}	22 s	21 s	+6 %
X_{90}	3.5 L_{PP}	3.7 L_{PP}	−3 %	X_{90}	3.7 L_{PP}	3.6 L_{PP}	+3 %
Y_{90}	-1.8 L_{PP}	-1.9 L_{PP}	−4 %	Y_{90}	2.0 L_{PP}	2.0 L_{PP}	+1 %
t_{180}	40 s	39 s	+3 %	t_{180}	44 s	40 s	+9 %
Y_{180}	-4.1 L_{PP}	-4.2 L_{PP}	−3 %	Y_{180}	4.4 L_{PP}	4.3 L_{PP}	+3 %

Zigzag test Figure 3.30 shows the results of a 10/10 and 20/20 zigzag test performed in calm water. Since no time series of experimental data was available, only a qualitative comparison was made for the 10/10 zigzag test with results shown by Yasukawa (2008), which showed similar trends. The results show that all values are well inside the IMO limits.

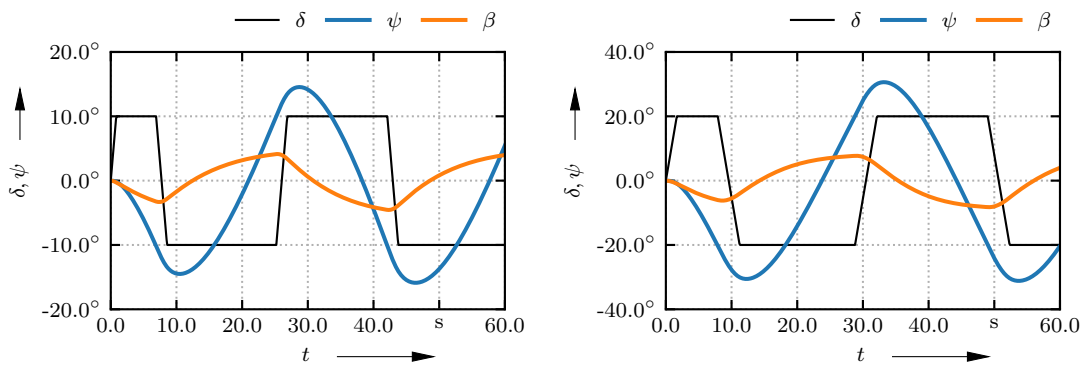

(a) ZZ 10/10

(b) ZZ 20/20

Figure 3.30.: Zigzag tests for S175 in calm water

Spiral test The results of a Dieudonné direct spiral test are shown in Figure 3.31, where $r' = rL_{PP}/u_0$ is the non-dimensional yaw rate. The result of this test shows that the S175 ship has a positive yaw stability, which is to be expected for a fast, slender container ship. The yaw stability can also be determined using the stability index (Söding, 1995):

$$s = \frac{N_r - mx_G u_0}{Y_r - mu_0} - \frac{N_v}{Y_v} \tag{3.3}$$

The resulting non-dimensional stability index of the S175 ship is $s' = 0.28$.

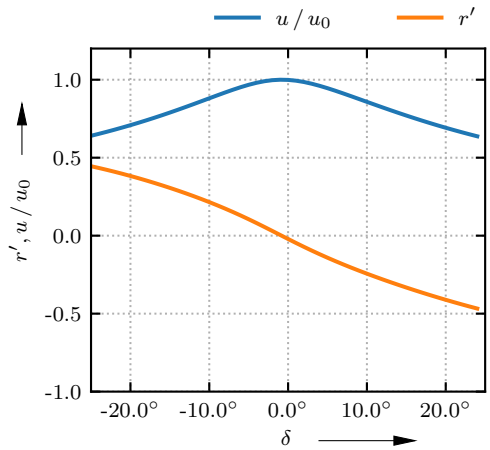

Figure 3.31.: Spiral test for S175 in calm water

3.3.2. Regular Waves

Turning circle Yasukawa and Nakayama (2009) have performed turning circle tests in regular waves to both port and starboard for non-dimensional wave lenths of $\lambda' = 0.5, 0.7, 1.0$ and 1.2. The wave amplitude of $\zeta'_A = 0.01$ was the same for all cases. All manoeuvres were started in head and beam waves, leading to a total of 16 turning circle tests in waves. Manoeuvres are only simulated and compared to experimental data for $\lambda' = 0.5, 0.7$ and 1.0, since no wave coefficients have been obtained for $\lambda' = 1.2$. For situations where the simulations were performed for a longer time as the experiments, the path of the ship is shown in dashed lines after the end of the measured time trace.

Figure 3.32 shows the turning circle test started in head waves for the shortest considered wave lenght of $\lambda' = 0.5$. The approach speed is still 90% of the approach speed in calm water, the speed loss throughout the manoeuvre with 50% of the approach speed is comparable to the calm water case. Although the simulations seem to overestimate the speed loss in following waves, the global trends are captured quite well. The predicted propeller torque shows a good agreement, but the value is with 30% just slightly higher compared to the one in calm water. There is a very good agreement for the first 20 s (first dot in the trace plot) of the manoeuvre both to port and starboard, which is right up to the time where the direction of the incoming waves change from head to following. As explained in Section 3.2.4, there is a strong dependence of the mean wave forces on the drift angle, which is not considered here. Figure 3.23 shows that especially for short beam waves the drift angle is being overestimated, which is also observed in this case. The results in Table 3.7 show that the predicted times for a 90° heading change are comparable or slightly smaller than the ones in calm water. It should be noted that the reason for the relatively large difference between experiment and simulation for the value Y_{90} is the very strong sensitivity of this value due to the steep gradient of Y/L_{PP} at this time.

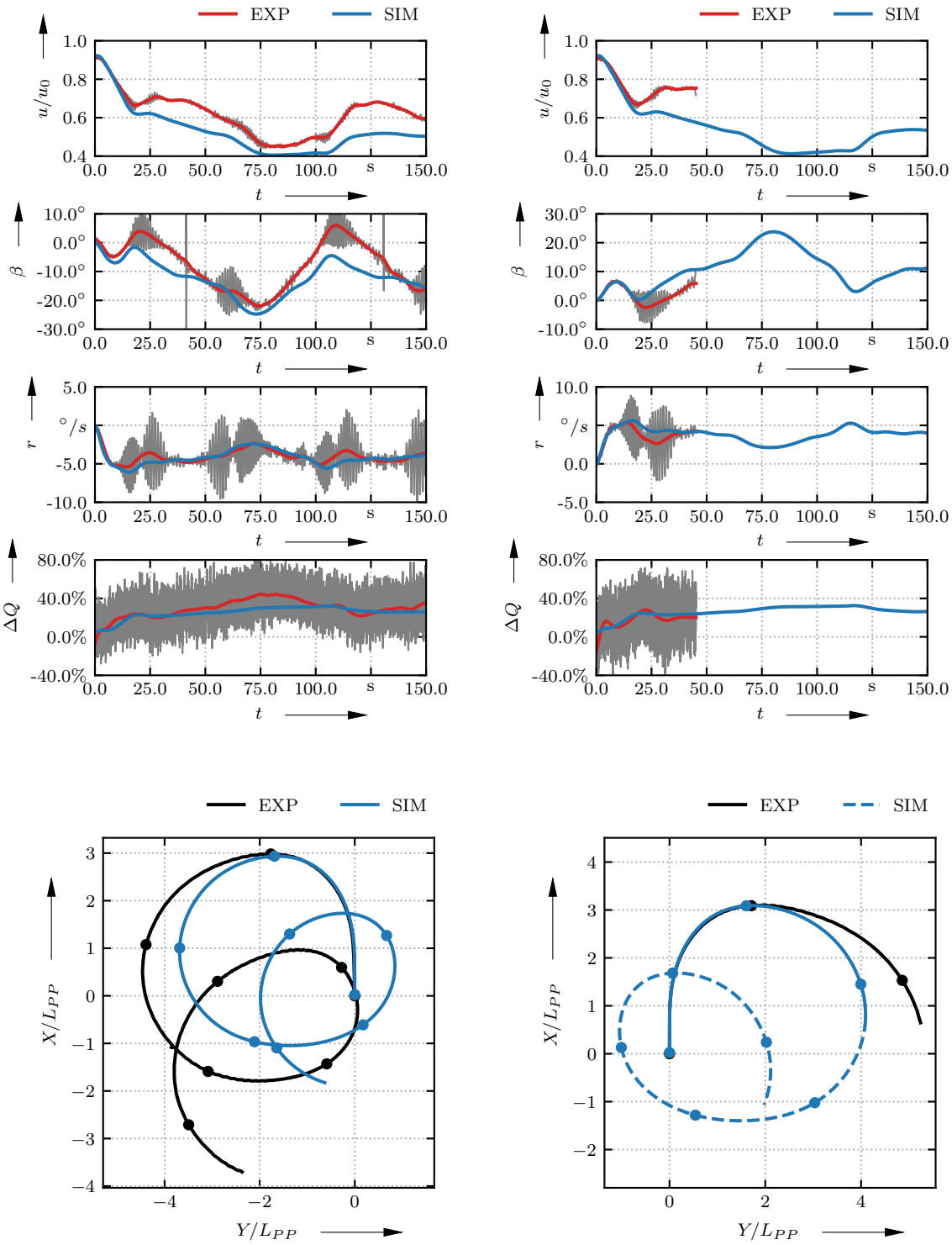

(a) Port

(b) Starboard

Figure 3.32.: Turning circle for S175 in waves with $\lambda' = 0.5, \alpha_0 = 0°$ compared to experimental data from Yasukawa and Nakayama (2009)

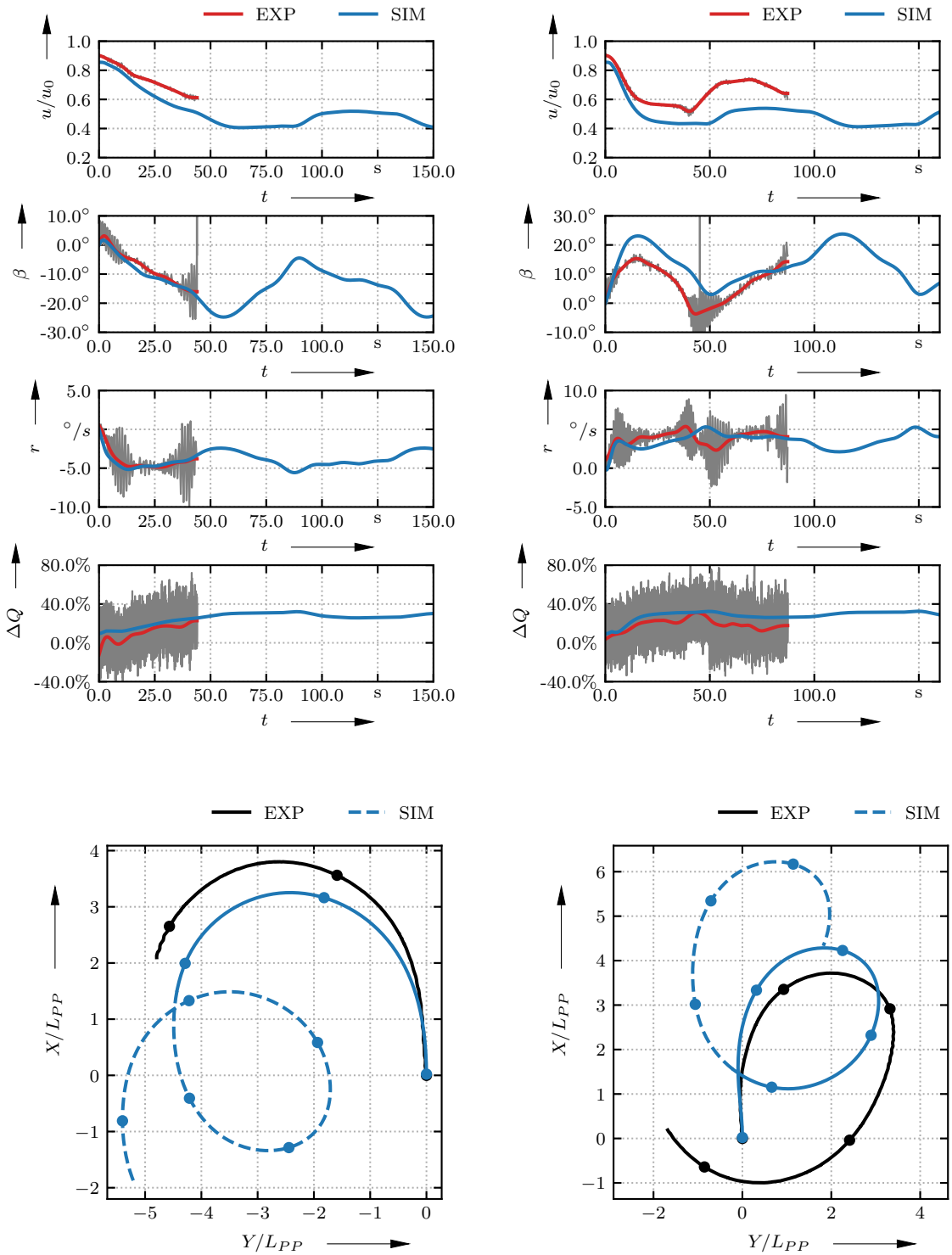

(a) Port

(b) Starboard

Figure 3.33.: Turning circle for S175 in waves with $\lambda' = 0.5, \alpha_0 = 90°$ compared to experimental data from Yasukawa and Nakayama (2009)

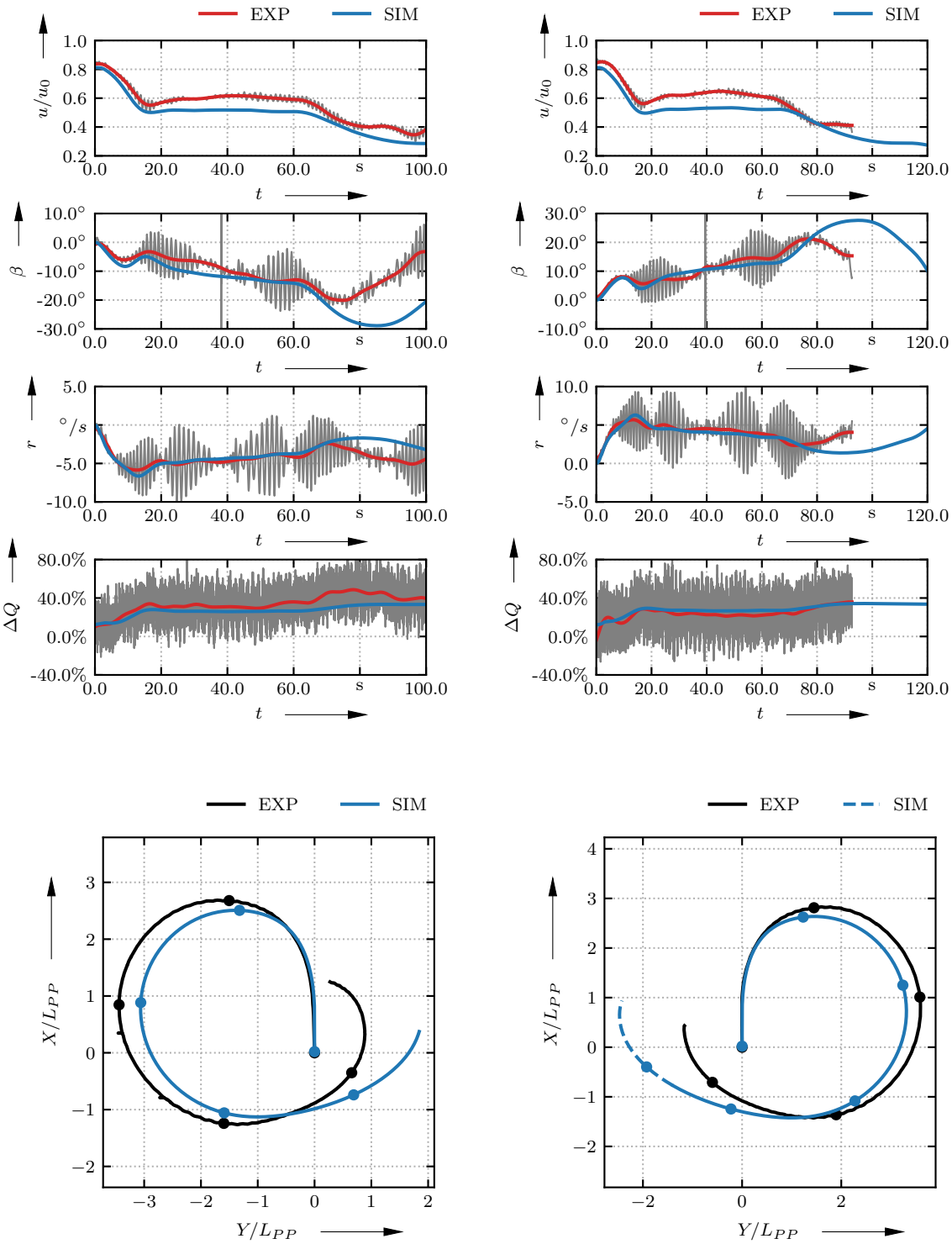

(a) Port

(b) Starboard

Figure 3.34.: Turning circle for S175 in waves with $\lambda' = 0.7, \alpha_0 = 0°$ compared to experimental data from Yasukawa and Nakayama (2009)

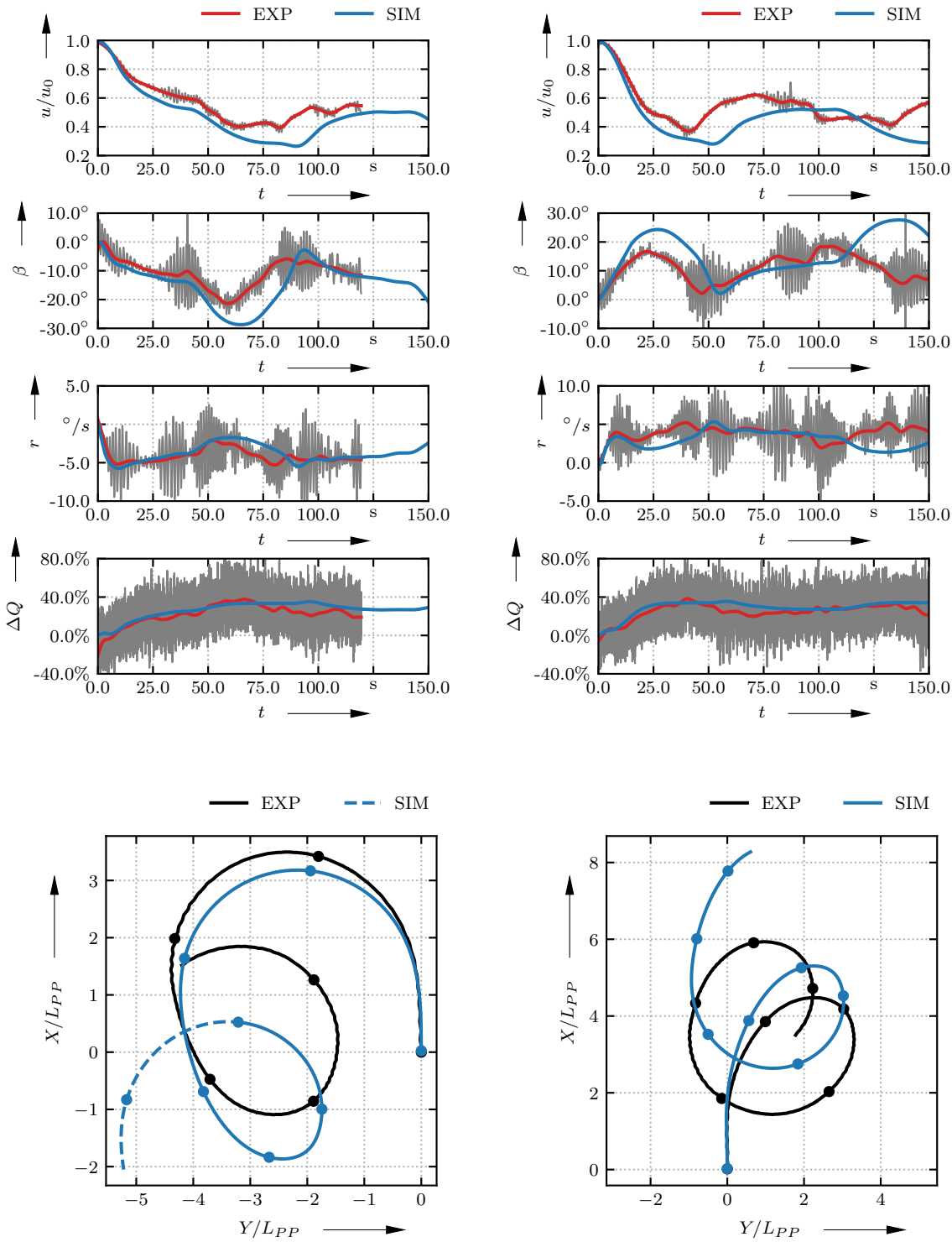

(a) Port

(b) Starboard

Figure 3.35.: Turning circle for S175 in waves with $\lambda' = 0.7, \alpha_0 = 90°$ compared to experimental data from Yasukawa and Nakayama (2009)

If the same manoeuvre is started in beam waves (Figure 3.33), the initial speed loss is again captured quite well, but discrepancies, which were observed in the previous case only after 20 seconds, are visible directly after the start of the manoeuvre. This could also be explained by the neglected coupling between mean wave forces and drift angle, especially when turning into the wave.

For waves with a length of $\lambda' = 0.7$, a very good agreement can be observed for all traces when starting the manoeuvre in head waves, see Figure 3.34. The approach speed is 80% of the approach speed in calm water and thus as expected the initial speed loss is slightly higher compared to the short wave. As expected, the advance and tactical diameter as well as the corresponding times are similar or slightly smaller than the ones in calm water due to the lower approach speed and the mean yaw moment of the wave supporting the turning motion of the ship. For this wave length, the coupling between drift angle and mean wave forces is less pronounced compared to the shorter wave.

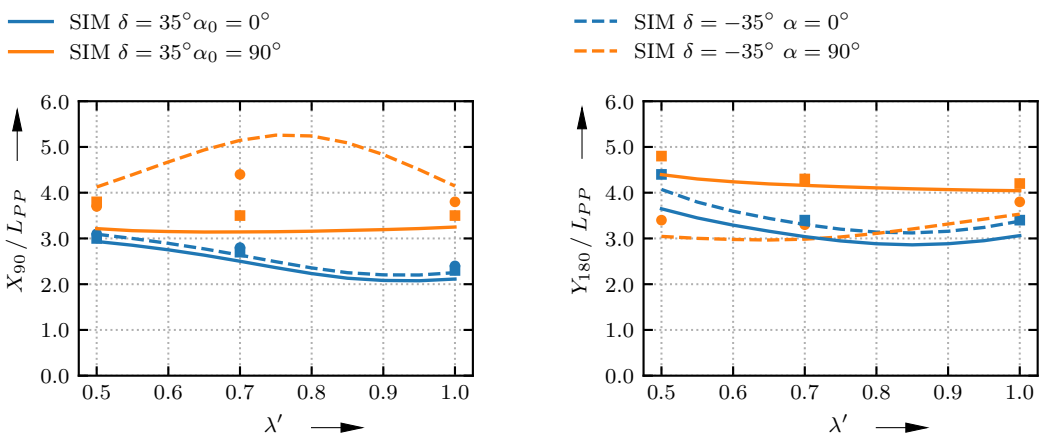

(a) Advance

(b) Tactical diameter

Figure 3.36.: Evaluated parameters for turning circle

If the manoeuvre is started in beam waves (Figure 3.35), the approach speed is almost the same as in calm water and a satisfactory agreement is obtained for the case of the ship turning away from the wave, e.g. staring to port. If the manoeuvre is started into the wave, a strong overestimation of the drift angle occurs, resulting in a significantly overestimated time of 35% for a 90° heading change. However, the simulation as well as the measurement predict a significant increase in t_{90} of 72% and 33% respectively compared to calm water. Figure 3.36 shows the dependence of the advance and tactical diameter on the wave length. The results of numerical (traces) and experimental (symbols) results show that the case of turning into the wave, especially at this wave length is one of the most demanding manoeuvres considered here.

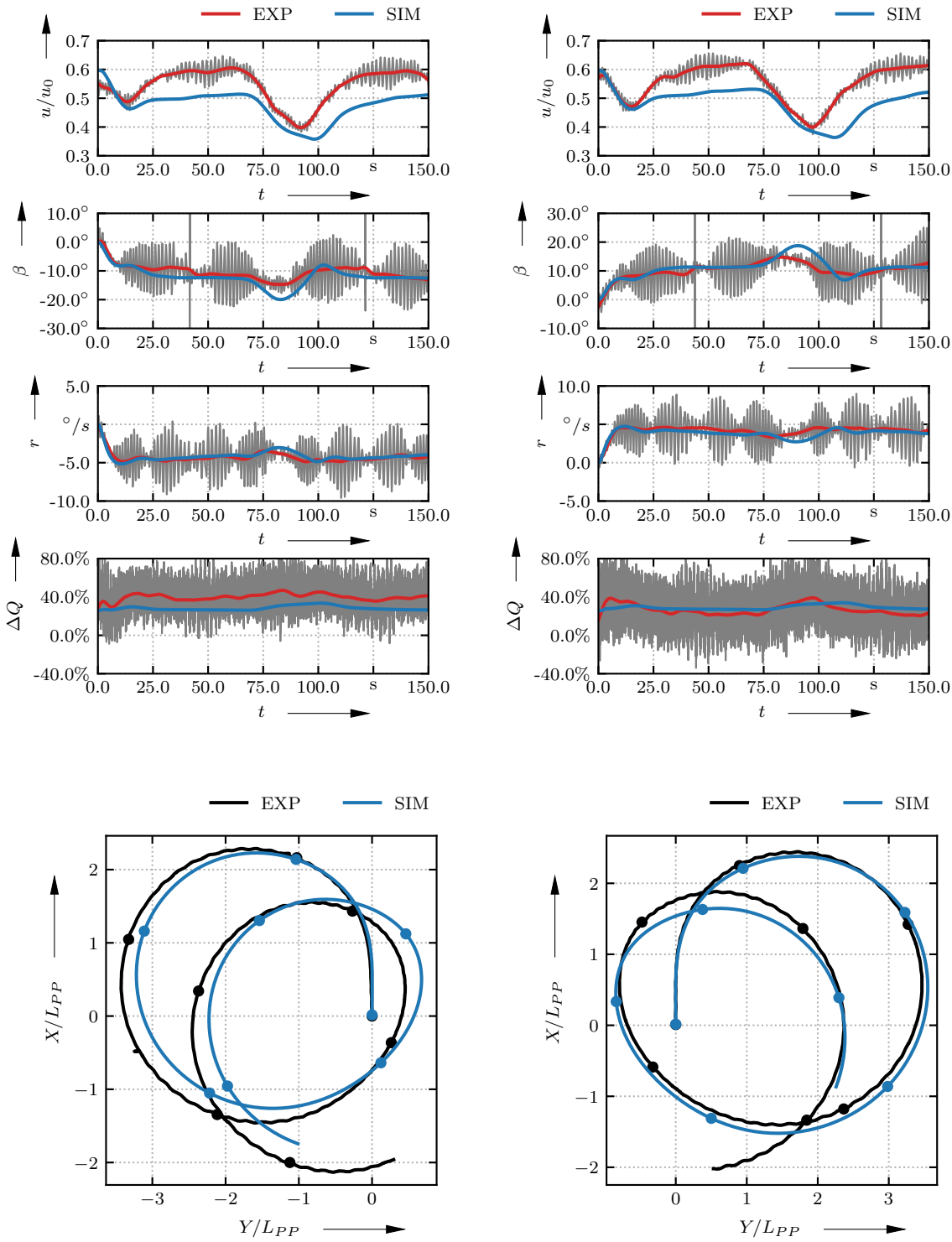

(a) Port

(b) Starboard

Figure 3.37.: Turning circle for S175 in waves with $\lambda' = 1.0, \alpha_0 = 0°$ compared to experimental data from Yasukawa and Nakayama (2009)

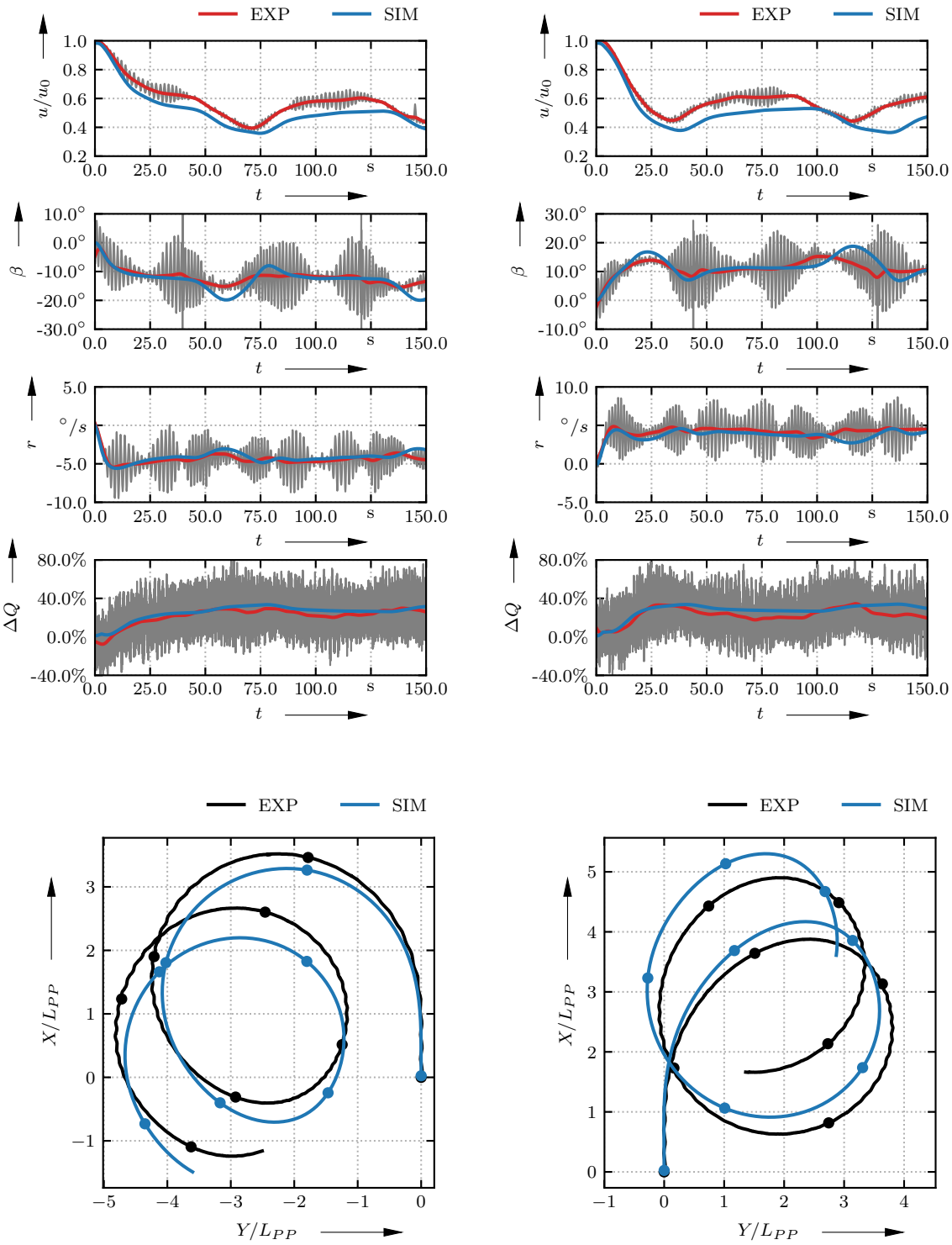

(a) Port

(b) Starboard

Figure 3.38.: Turning circle for S175 in waves with $\lambda' = 1.0, \alpha_0 = 90°$ compared to experimental data from Yasukawa and Nakayama (2009)

Figure 3.37 shows the results for the longest considered wave with $\lambda' = 1.0$. The initial speed loss is 40% compared to calm water. The experimental value for the tunring circle to starboard shows the same speed loss, but the one to port shows an even larger speed loss, although both values are expected to be the same. When looking at the required mean added power it can be seen that in contrast to the previous manoeuvres, there is a significantly increased added power of 30% during the approach phase and the maximum value of roughly 40% is also larger than the one in calm water. Figure 3.38 shows the same manoeuvre starting in beam waves with similar results.

In addition two turning circles are simulated started in following waves. The results are shown in Figure 3.39. The case of $\lambda' = 0.7$ seems to be a quite challenging manoeuvre. However, it should be considered, that the effect of the wave has been overestimated for the case of $\lambda = 0.7$ and $\alpha_0 = 90°$ and therefore might not be as significant as indicated here.

Comparison of different starting conditions One of the manoeuvres has been performed with three different starting conditions, namely starting all manoeuvres with the same propeller revolution rate as in calm water (and thus different forward speed and required power), the same forward speed as in calm water (and thus different propeller revolution rate and required power) or the same power as in calm water (and thus different speed and propeller revolution rate).

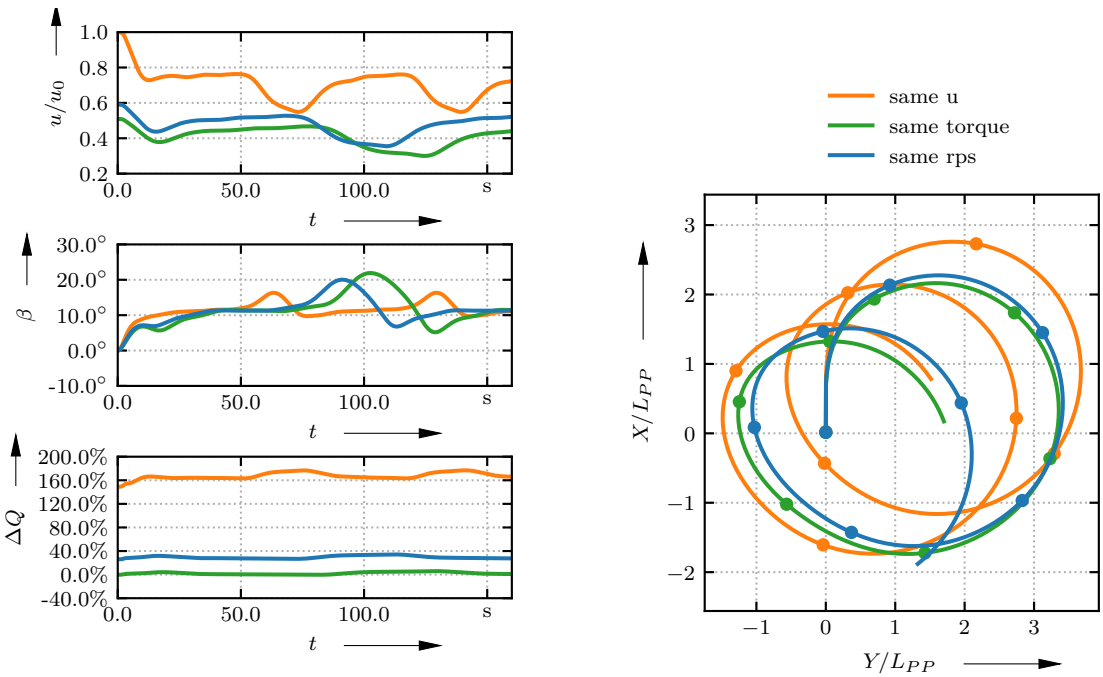

Figure 3.40.: Different starting conditions for S175 in waves with $\lambda' = 1.0, \alpha_0 = 0°$

The results are shown in Figure 3.40 and Table 3.8. It can be seen that the required

power to maintain a constant approach speed in head waves is roughly 160% compared to the required power in calm water and in the same range as the power predicted by Nakamura and Hosoda (1975). The manoeuvre shows that the times t_{90} and t_{180} decrease significantly for the higher approach speed to 17 s and 32 s, but the advance and tactical diameter increase slightly due to the higher approach speed. If the manoeuvre is started with a constant torque, it is possible to execute the whole manoeuvre with nearly no additional power and similar characteristics. Although it is unrealistic, that the manoeuvre is executed in waves at full speed, this indicates that for the development of rules regarding the required power of ships in waves, the initial condition plays an important role and the times t_{90} and t_{180} might be a more valuable indicator for manoeuvrability than the advance or tactical diameter.

Table 3.7.: Results of turning circle tests in head waves compared to experimental data from Yasukawa and Nakayama (2009)

Port						Starboard					
λ'	α_0		SIM	EXP	DIFF	λ'	α_0		SIM	EXP	DIFF
0.5	0°	t_{90}	19 s	21 s	−9 %	0.5	0°	t_{90}	21 s	22 s	−5 %
		X_{90}	2.9 L_{PP}	3.0 L_{PP}	−1 %			X_{90}	3.1 L_{PP}	3.1 L_{PP}	−0 %
		Y_{90}	-1.5 L_{PP}	-1.9 L_{PP}	−20 %			Y_{90}	1.7 L_{PP}	2.0 L_{PP}	−15 %
		t_{180}	38 s	41 s	−8 %			t_{180}	42 s	-	-
		Y_{180}	-3.6 L_{PP}	-4.4 L_{PP}	−18 %			Y_{180}	4.1 L_{PP}	-	-
0.7	0°	t_{90}	19 s	20 s	−6 %	0.7	0°	t_{90}	20 s	20 s	+1 %
		X_{90}	2.5 L_{PP}	2.7 L_{PP}	−7 %			X_{90}	2.6 L_{PP}	2.8 L_{PP}	−7 %
		Y_{90}	-1.2 L_{PP}	-1.5 L_{PP}	−22 %			Y_{90}	1.3 L_{PP}	1.5 L_{PP}	−14 %
		t_{180}	38 s	38 s	−0 %			t_{180}	41 s	40 s	+5 %
		Y_{180}	-3.0 L_{PP}	-3.4 L_{PP}	−12 %			Y_{180}	3.3 L_{PP}	3.6 L_{PP}	−8 %
1.0	0°	t_{90}	22 s	23 s	−4 %	1.0	0°	t_{90}	24 s	24 s	−0 %
		X_{90}	2.2 L_{PP}	2.3 L_{PP}	−3 %			X_{90}	2.4 L_{PP}	2.4 L_{PP}	−2 %
		Y_{90}	-1.3 L_{PP}	-1.4 L_{PP}	−10 %			Y_{90}	1.4 L_{PP}	1.4 L_{PP}	+2 %
		t_{180}	42 s	42 s	+1 %			t_{180}	46 s	44 s	+4 %
		Y_{180}	-3.2 L_{PP}	-3.4 L_{PP}	−6 %			Y_{180}	3.5 L_{PP}	3.4 L_{PP}	+2 %
0.5	90°	t_{90}	21 s	24 s	−10 %	0.5	90°	t_{90}	33 s	26 s	+28 %
		X_{90}	3.2 L_{PP}	3.8 L_{PP}	−15 %			X_{90}	4.2 L_{PP}	3.7 L_{PP}	+15 %
		Y_{90}	-2.0 L_{PP}	-2.3 L_{PP}	−10 %			Y_{90}	1.4 L_{PP}	1.7 L_{PP}	−13 %
		t_{180}	42 s	44 s	−4 %			t_{180}	53 s	45 s	+17 %
		Y_{180}	-4.4 L_{PP}	-4.8 L_{PP}	−9 %			Y_{180}	3.1 L_{PP}	3.4 L_{PP}	−10 %
0.7	90°	t_{90}	19 s	21 s	−10 %	0.7	90°	t_{90}	40 s	28 s	+39 %
		X_{90}	3.1 L_{PP}	3.5 L_{PP}	−9 %			X_{90}	5.2 L_{PP}	4.4 L_{PP}	+18 %
		Y_{90}	-1.8 L_{PP}	-2.0 L_{PP}	−12 %			Y_{90}	1.9 L_{PP}	1.9 L_{PP}	+0 %
		t_{180}	40 s	41 s	−1 %			t_{180}	60 s	48 s	+26 %
		Y_{180}	-4.2 L_{PP}	-4.3 L_{PP}	−4 %			Y_{180}	3.0 L_{PP}	3.3 L_{PP}	−8 %
1.0	90°	t_{90}	20 s	20 s	−4 %	1.0	90°	t_{90}	28 s	24 s	+16 %
		X_{90}	3.2 L_{PP}	3.5 L_{PP}	−7 %			X_{90}	4.1 L_{PP}	3.8 L_{PP}	+8 %
		Y_{90}	-1.7 L_{PP}	-1.9 L_{PP}	−8 %			Y_{90}	2.0 L_{PP}	2.0 L_{PP}	−2 %
		t_{180}	40 s	40 s	+2 %			t_{180}	49 s	44 s	+12 %
		Y_{180}	-4.0 L_{PP}	-4.2 L_{PP}	−4 %			Y_{180}	3.6 L_{PP}	3.8 L_{PP}	−5 %

Table 3.8.: Results of turning circle tests in head waves with $\lambda' = 1$ for different starting conditions

	X_{90}	t_{90}	Y_{180}	t_{180}
same rps	2.35 L_{PP}	24.1 s	3.51 L_{PP}	45.8 s
same speed	2.73 L_{PP}	16.6 s	3.64 L_{PP}	31.7 s
same torque	2.25 L_{PP}	26.6 s	3.43 L_{PP}	50.9 s

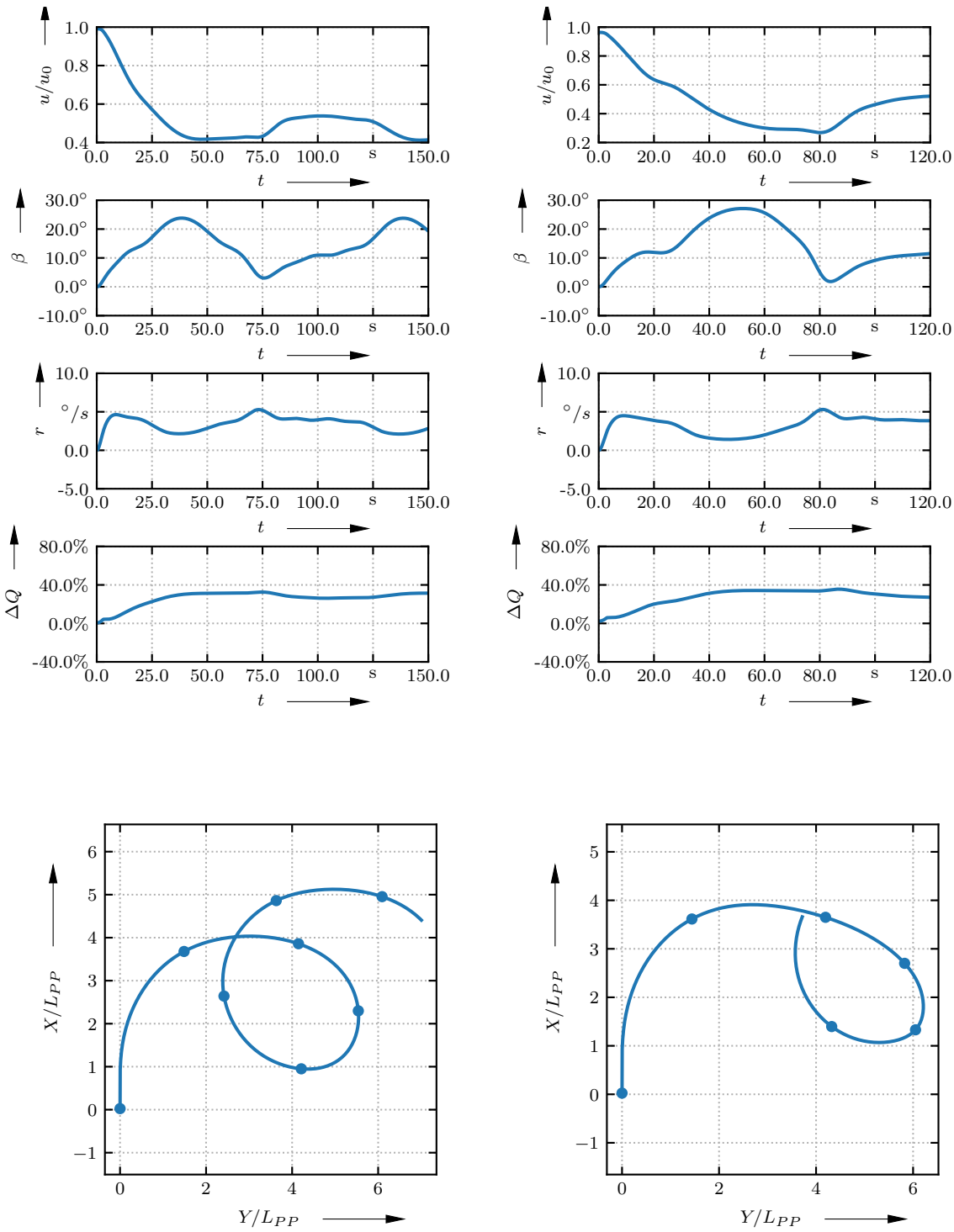

(a) $\lambda' = 0.5$

(b) $\lambda' = 0.7$

Figure 3.39.: Turning circle for S175 in following waves

4. Conclusions and Outlook

This thesis presents a numerical method for the prediction of rudder manoeuvres and the required power during these manoeuvres in harmonic waves of arbitrary length, height and direction. The method uses hydrodynamic coefficients to compute the forces and moments required for the manoeuvring prediction in every time step. An existing calm water mathematical mode of Abkowitz type has been extended to take mean forces and moments due to incoming waves into account. Further, the extended mathematical model includes the propeller torque as well, allowing a prediction of the required power during the manoeuvre. In addition an efficient method to simulate manoeuvres with different propeller revolution rates was developed. The method was applied to and validated using the S175 benchmark container ship. All hydrodynamic forces and moments needed for the determination of the hydrodynamic coefficients are computed with high accuracy using virtual captive model tests performed with the RANS code Neptuno, which has been adopted for this purpose. After all coefficients are determined, the method allows for a fast and reliable prediction of arbitrary rudder manoeuvres in waves.

A total of 377 static and five dynamic tests were computed in calm water, from which 137 were necessary for the determination of the hydrodynamic coefficient set. During the computations, the effect of the propeller on the flow was resembled using a body force model, which allowed the determination of thrust and torque depending on the current inflow condition. After all coefficients were determined, the quality of the mathematical model was evaluated by comparing the modelled and computed values, showing a satisfactory agreement in almost all cases. Additional computations with different propeller revolution rates were performed to validate the newly developed propeller revolution rate model. A good agreement was observed in this case as well.

For the determination of the hydrodynamic coefficients of the wave force model, 228 semi captive model tests were performed in incoming waves of different length, height and direction, from which only 117 are necessary to determine a coefficient set with sufficient accuracy. The motions during the virtual tests were weakly prescribed by using the virtual spring system, developed to resemble the experimental setup during the simulations. The validation of the numerical computations was done by using experimental data from Yasukawa and Adnan (2006) and Fujii and Takahashi (1975). It was shown that for the current application case the influence of mean non hydrodynamic inertial contributions is significant and cannot be neglected. For the head wave case, this contribution was observed to be up to 40% and a good agreement with the experimentally measured values was only achieved after including these effects. Further, the dependence of the mean wave forces and moments in head, oblique and following waves on wave amplitude, drift angle, forward speed and transverse radius of gyration was investigated. It was shown, that for the present application case the assumption of a quadratic dependence of mean

wave forces on the wave amplitude is not valid in all situations. The dependence of the mean wave forces on the drift angle, which was also observed in the experiments, was confirmed.

After the determination of all required hydrodynamic coefficients, manoeuvres can be simulated with negligible computational time. In calm water, a turning circle with rudder execution of 35° to port and starboard was simulated as well as a 10/10 and 20/20 Z-test. Validation data was only available for the turning circle tests and a very good agreement was observed for the traces and time series, including the predicted increase in required power during the manoeuvre of 26% compared to the required power during the approach. The turning circle tests were repeated in incoming head and beam waves for three different wave lengths. The developed model was able to accurately predict the speed loss during the approach in all situations, with values of up to 40%. The quality of the predicted manoeuvres was very satisfactory in most cases. Larger differences were observed just for the case of a non-dimensional wave length $\lambda' = 0.7$ starting in beam seas and for two cases of relatively short waves with $\lambda' = 0.5$. It is assumed that this difference could partially be caused by neglecting coupling terms between drift angle and mean wave forces and moments in the mathematical model. The discrepancy between experiment and numerical prediction for the parameters advance, tactical diameter and the corresponding times are usually about 10%, with maximum discrepancies for the cases mentioned above of up to 40%.

In general, the performed manoeuvre simulations (as well as the experimental results) indicated that for the present ship the required mean power throughout a turning circle manoeuvre in waves is not significantly higher than during the same manoeuvre in calm water. However, no clear regulations or requirements for the manoeuvrability in waves exist and thus the selected cases might not be representative. Three different starting conditions were compared for one manoeuvre, namely starting all manoeuvres with the same propeller revolution rate as in calm water, the same forward speed as in calm water or the same power as in calm water. It was shown, that for the development of rules regarding the minimum required power for manoeuvring in waves the starting condition plays an important role and the times t_{90} and t_{180} might be a more valuable indicator for manoeuvrability than the advance or tactical diameter.

It can be concluded that the presented method is able to predict manoeuvres and mean required power in waves with good accuracy. In contrast to existing potential flow method, the presented RANS approach is completely independent of external coefficients obtained experimentally as for example cross flow coefficients. The selected approach combines the advantage of high fidelity RANS simulations, which allow to determine the mean wave forces with higher accuracy than for example potential flow computations, with the possibility of quickly predicting arbitrary rudder manoeuvres once all coefficients are obtained. Additional validation and thus also further experimental investigation of this complicated case is required in order to reliably determine the accuracy that can be achieved. Combined with the ability to predict the required power and the extension of the model to capture the effect of different propeller revolution rates, this tool can be used for deriving rules regarding the minimum required power for manoeuvring.

In a future work, a more detailed investigation of the coupling between drift angle and mean wave forces should be performed and may be included in the mathematical model. However, this would considerably increase the number of required computations. Further, an extension of the proposed method to include irregular seaways and can be achieved by superposition of the mean wave forces for each elementary wave of the wave energy spectrum and would allow for the computation of more practical application cases. For a more precise prediction of the required power, an alternative approach, e.g. based on splines, should be considered for modelling the propeller torque. Since the presented method allows to perform simulations with varying propeller revolution rates, an engine model could be included for simulations without much additional effort. In addition, critical manoeuvres in waves need to be identified to allow proper judgement of manoeuvring capabilities.

Bibliography

Abkowitz, M. A. (1964). Lectures on Ship Hydrodynamics – Steering and Manoeuvrability. Technical report, Hydro- og Aerodynamisk Laboratorium.

Amini Afshar, M. (2014). *Towards Predicting the Added Resistance of Slow Ships in Waves*. PhD thesis, Technical University of Denmark.

Bai, K. J. and Yeung, R. W. (1974). Numerical Solutions of Two-Dimensional Nonlinear Wave Problems. In *Proceedings of the 10th ONR Symposium on Naval Hydrodynamics*, page 609.

Boese, P. (1970). Eine einfache Methode zur Berechnung der Widerstandserhöhung eines Schiffes im Seegang. *Schriftenreihe Schiffbau TUHH (Nr. 258)*. (in German).

Carrica, P. M., Ismail, F., Hyman, M., Bhushan, S., and Stern, F. (2012). Turn and zigzag maneuvers of a surface combatant using a URANS approach with dynamic overset grids. *Journal of Marine Science and Technology*, 18(2):166–181.

Carrica, P. M. and Stern, F. (2008). DES simulations of KVLCC1 in turn and zigzag maneuvers with moving propeller and rudder. In *Proceedings of SIMMAN 2008 Workshop*, page F10, Copenhagen.

Chang, M. S. (1977). Computations of the three-dimensional ship motions with forward speed. In *Proceedings of the 2nd International Conference on Numerical Ship Hydrodynamics*.

Clauss, G., Lehmann, E., and Östergaard, C. (1988). *Meerestechnische Konstruktionen*. Springer. (in German).

Cummins, W. (1962). The impulse response function and ship motions. *Schiffstechnik*, 9:101–109.

Cura Hochbaum, A. (1993). *Ein Finite-Volumen-Verfahren zur Berechnung turbulenter Schiffsumströmungen*. PhD thesis, Technische Universität Hamburg. (in German).

Cura Hochbaum, A. (2006). Virtual PMM tests for manoeuvring prediction. In *Proceedings of the 26th ONR Symposium on Naval Hydrodynamics*, Rome.

Cura Hochbaum, A. and Pierzynski, M. (2005). Flow Simulation for a Combatant in Head Waves. In *Proceedings of the CFD workshop Tokyo05*, pages 1–5.

Cura Hochbaum, A. and Uharek, S. (2014). Prediction of the manoeuvring behaviour of the KCS based on virtual captive tests. In *Proceedings of SIMMAN 2014 Workshop*, Copenhagen.

Cura Hochbaum, A. and Uharek, S. (2016). Prediction of Ship Manoeuvrability in Waves Based on RANS Simulations. In *Proceedings of the 31st ONR Symposium on Naval Hydrodynamics*.

Cura Hochbaum, A. and Vogt, M. (2002). Towards the simulation of seakeeping and maneuvering based on the computation of the free surface viscous ship flow. In *Proceedings of the 24th ONR Symposium on Naval Hydrodynamics*, Fukuoka.

Cura Hochbaum, A., Vogt, M., and Gatchell, S. (2008). Maneuvering prediction for two tankers based on RANS simulations. In *Proceedings of SIMMAN 2008 Workshop*, page F22, Copenhagen.

Det Norske Veritas (2011). Steering gear. *Rules for classification of ships / high speed, light craft and naval surface craft*, 4(14).

DIN (1987). Vektoren, Matrizen, Tensoren: Zeichen und Begriffe. Technical report, Deutsche Industrie Norm 1303.

el Moctar, O., Lantermann, U., Mucha, P., Höpken, J., and Schellin, T. E. (2014). RANS-Based Simulated Ship Maneuvering Accounting for Hull-Propulsor-Engine Interaction. In *Proceedings of the 30st ONR Symposium on Naval Hydrodynamics*.

Faltinsen, O. M. (1990). *Sea Loads on Ship and Offshore Structures*. Cambridge University Press.

Fujii, H. and Takahashi, T. (1975). Experimental study on the resistance increase of a ship in regular oblique waves. *Journal of the Society of Naval Architects of Japan*, 1975(137):132–137.

Gerritsma, J. and Beukelmann, W. (1972). Analysis of the resistance increase in waves of a fast cargo ship. *International Shipbuilding Progress*, 19(217):285–293.

Grim, O. (1953). Berechnung der durch Schwingungen eines Schiffskörpers erzeugten hydrodynamischen Kräfte. In *Jahrbuch der Schiffbautechnischen Gesellschaft*. (in German).

Grim, O., Oltmann, P., Sharma, S. D., and Wolff, K. (1976). CPMC – A Novel Facility for Planar Motion Testing of Ship Models. In *Proceedings of the 11st ONR Symposium on Naval Hydrodynamics*.

Hirano, M., Takashina, J., Takaishi, Y., and Saruta, T. (1980). Ship Turning Trajectory in Regular Waves. *West Japan Society of Naval Architects*, (60):17.

Hutchison, B. L. (1990). Seakeeping Studies - A Status Report. *SNAME Transactions*, 98:263–317.

International Maritime Organisation (2002). Standards for Ship Manoeuvrability. *Resolution MSC.137(76)*.

ITTC (2002). Uncertainty Analysis in CFD. In *ITTC – Recommended Procedures and Guidelines*, pages 7.5–03.

ITTC (2017). 1978 ITTC Performance Prediction Method. In *ITTC – Recommended Procedures and Guidelines*, number 7.5-02-03-01.4.

Koopmann, L., Beutel, J., and Cura Hochbaum, A. (2015). Abschlussbericht des Teilvorhabens Captivman. Technical report, Technical University Berlin. (in German).

Korvin-Kroukovski, B. V. and Jacobs, W. R. (1957). Pitching and heaving motions of a ship in regular waves. *SNAME Transactions 65*, pages 590–632.

Lengwinat, A. and Cura Hochbaum, A. (2018). The influence of inertial effects on the mean forces and moments on a ship sailing in oblique waves part A: A new measurement device for wave forces. *Ocean Engineering*, 166:1–11.

Lengwinat, A., Uharek, S., Cura Hochbaum, A., Roetting, F., and el Moctar, B. O. (2016). Validation results of numerical tools for the ROPAX ship. Delivrable D4.8, Energy Efficient Safe SHip OPERAtion.

Lewis, E. V., editor (1988). *Principles of Naval Architecture*, volume 2. The Society of Naval Architects and Marine Engineers.

Liu, S. and Papanikolaou, A. (2016). Fast approach to the estimation of the added resistance of ships in head waves. *Ocean Engineering*, 112:211–225.

Maruo, H. (1960). The drift of a body floating on waves. *Journal of Ship Research*, 4(3):1–10.

Maruo, H. (1963). Resistance in waves. *60th Anniversary Series, The Society of Naval Architects of Japan.*

Matsumoto, K. and Suemitsu, K. (1980). The prediction of manoeuvring performances by captive model tests. *Journal of the Kansai Society of Naval Architects*, 176.

Mofidi, A. and Carrica, P. M. (2014). Verification of 20/5 zigzag maneuver for a container ship with direct moving rudder and propeller. In *Proceedings of SIMMAN 2014 Workshop.*

Nakamura, S. and Hosoda, R. (1975). A method for predicting the power of ships in a seaway. In *Proceedings of the 14th ITTC.*

Nakamura, S. and Naito, S. (1977). Propulsive Performance of a Container Ship in Waves. *Journal of the Society of Naval Architects of Japan*, 15:24–48.

Noblesse, F. and Hendrix, D. (1992). On the Theory of Potential Flow About a Ship Advancing in Waves. *Journal of Ship Research*, pages 17–29.

Oberhagemann, J. (2016). *On Prediction of Wave-Induced Loads and Vibration of Ship Structures with Finite Volume Fluid Dynamic Methods.* PhD thesis, Universität Duisburg-Essen.

Oltmann, P. (1973). Auswertung von Bahnkurven freifahrender Schiffsmodelle. Technical Report 298, SFB 98. (in German).

Oltmann, P. (1978). Bestimmung der Manövriereigenschaften aus den Bahnkurven freimanövrierender Schiffsmodelle. Technical Report 364, Institut für Schiffbau der Universität Hamburg. (in German).

Osher, S. and Sethian, J. A. (1988). Fronts Propagating with Curvature-Dependent Speed: Algorithms Based on Hamilton-Jacobi Formulations. *Journal of Computational Physics*, 79:12–49.

Papanikolaou, A., Fournarakis, N., Chroni, D., Liu, S., and Plessas, T. (2016). Simulation of the Maneuvering Behavior of Ships in Adverse Weather Conditions. In *Proceedings of the 31st ONR Symposium on Naval Hydrodynamics*.

Papanikolaou, A. and Zaraphonitis, G. (2001). *Computer Program NEWDRIFT v.7*. NTUA.

Patankar, S. V. and Spalding, D. B. (1972). A Calculation Procedure for Heat, Mass and Momentum Transfer in Three-Dimensional Parabolic Flows. *International Journal of Heat and Mass Transfer*, 15.

Perić, R. and Abdel-Maksoud, M. (2016). Reliable damping of free-surface waves in numerical simulations. *Ship Technology Research*, 63(1):1–13.

Pinkster, J. and van Oortmerssen, G. (1977). Computation of the first and second order wave forces on oscillating bodies in regular waves. In *Proceedings of the second international conference on numerical ship hydrodynamics*, page 136, Berkeley, California, US.

Quadvlieg, F., Stern, F., Simonsen, C. D., and Otzen, J. F., editors (2018). *SIMMAN 2014 - Workshop an Verification and Validation of Ship Manoeuvering Simulation Methods*.

Saunders, H. E. (1965). *Hydrodynamics in Ship Design*, volume 3. The Society of Naval Architects and Marine Engineers.

Schneekluth, H. (1988). *Hydromechanik zum Schiffsentwurf*. Koehler, 3rd edition. (in German).

Schoop-Zipfel, J. (2016). *Efficient simulation of ship maneuvers in waves*. PhD thesis, Technische Universität Hamburg, Technische Universität Hamburg-Harburg.

Schumann, C. (2015). Modellierung von Wellen mit einem Finite-Volumen-Verfahren. Technical report, Ingenieurbüro Schiffsrat. private communication (in German).

Schumann, C. (2017). Manoeuv Version 1.2 – Verbesserte Berechnung der stationären Rumpfkräfte. Technical report, Ingenierbüro SchiffsRat. (in German).

Shigunov, V., el Moctar, O., Papanikolaou, A., Potthoff, R., and Liu, S. (2018). International benchmark study on numerical simulation methods for prediction of manoeuvrability of ships in waves. *Ocean Engineering*, 165:365–385.

Sibul, O. J. (1971). Measurement and Calculations of Ship Resistance in Waves. Technical Report NA-71-2, University of California, College of Engineering, Berkeley.

Sigmund, S. and el Moctar, O. (2018). Numerical and experimental investigation of added resistance of different ship types in short and long waves. *Ocean Engineering*, 147:51–67.

Skejic, R. (2013). Ships Maneuvering Simulations in a Seaway: How close are we to reality? *IWNTM13: International Workshop on Nautical Traffic*.

Skejic, R. and Faltinsen, O. M. (2008). A unified seakeeping and maneuvering analysis of ships in regular waves. *Journal of Marine Science and Technology*, 13(4):371–394.

Skejic, R. and Faltinsen, O. M. (2013). Maneuvering Behavior of Ships in Irregular Waves. In *Volume 9: Odd M. Faltinsen Honoring Symposium on Marine Hydrodynamics*. ASME.

Smitt, L. W. and Chislett, M. S. (1974). Large amplitude PMM tests and maneuvering predictions for a mariner class vessel. In *Proceedings of the 10th ONR Symposium on Naval Hydrodynamics*, pages 317–381.

Son, K. and Nomoto, K. (1981). On the Coupled Motion of Steering and Rolling of a High Speed Container Ship. *Journal of the Society of Naval Architects of Japan*, 1981(150):232–244.

Spurk, J. H. (1996). *Stömungslehre*. Springer, 4. auflage edition. (in German).

Strøm-Tejsen, J. and Chislett, M. S. (1966). A model testing technique and method of analysis for the prediction of steering and manoeuvring qualities of surface ships. In *Proceedings of the 6th ONR Symposium on Naval Hydrodynamics*, pages 131–157.

Sussman, M., Smereka, P., and Osher, S. (1994). A level set approach for computing solutions to incompressible two-phase flow. *Journal of Computational physics*, 114(1):146–159.

Söding, H. (1982). Bewegungen und Belastungen der Schiffe im Seegang. Technical report, Technische Universität Hamburg. (in German).

Söding, H. (1995). Manövrierfähigkeit von Schiffen. Technical report, Technische Universität Hamburg. (in German).

Söding, H., von Graefe, A., el Moctar, O., and Shigunov, V. (2012). Rankine Source Method for Seakeeping Predictions. In *Proceedings of the ASME 31st International Conference on Ocean, Offshore and Arctic Engineering (OMAE)*, pages 1–12.

Taniguchi, K. (1966). Study on Scale Effect of Propulsive Performance by Use of Geosims of a Tanker. Technical report, Mitsubishi Heavy Industries Ltd.

Tello Ruiz, M., Candries, M., Vantorre, M., Delefortrie, G., Peeters, D., and Mostaert, F. (2012). Ship Manoeuvring in Waves. *WL Rapporten, 00_096*, pages 1–29.

The Manoeuvring Committee (2014). Final Report and Recommendations to the 27th ITTC. Technical report, ITTC.

The Manoeuvring Committee (2017). Final Report and Recommendations to the 28th ITTC. Technical report, ITTC.

Ueno, M., Nimura, T., and Miyazaki, H. (2003). Experimental study on manoeuvring motion of a ship in waves. In *MARSIM*. Proceedings of MARSIM.

Uharek, S. (2013). Berechnung der mittleren Seegangskräfte auf ein Schiff in Abhängigkeit des Welleneinfallwinkels mit einem RANSE-Löser. Master's thesis, Technische Universität Berlin. (in German).

Uharek, S. and Cura Hochbaum, A. (2015). Modelling Mean Forces and Moments Due to Waves Based on RANS Simulations. In *Proceedings of the 25th International Ocean and Polar Engineering Conference (ISOPE)*, pages 46–51.

Uharek, S. and Cura Hochbaum, A. (2018a). Power Prediction for Safe Manoeuvring in Waves. In *Proceedings of the 32nd ONR Symposium on Naval Hydrodynamics*.

Uharek, S. and Cura Hochbaum, A. (2018b). The influence of inertial effects on the mean forces and moments on a ship sailing in oblique waves Part B: Numerical prediction using a RANS code. *Ocean Engineering*, 165:264–276.

Uharek, S., Lengwinat, A., and Cura Hochbaum, A. (2016). Abschlussbericht Teilvorhaben Promansee (Fkz.: 03SX339E). Technical report, Technische Universität Berlin. (in German).

Ursell, F. (1948). On the heaving motion of a circular cylinder on the surface of a fluid. *Journal of Mechanics and Applied Mathematics*.

Valanto, P. and Hong, Y. (2015). Experimental Investigation on Ship Wave Added Resistance in Regular Head, Oblique, Beam, and Following Waves. In *Proceedings of ISOPE*, pages 19–26. International Society of Offshore and Polar Engineers.

WAMIT (2016). *WAMIT User Manual Version 7.2*.

Weede, H. (2000). Systemidentifikation manövrierender Schiffsmodelle. *Schiff und Hafen*. (in German).

Wilcox, D. C. (1993). *Turbulence Modeling for CFD*. DCW Industries, 1st edition.

Wolff, K. (1981). Ermittlung der Manövriereigenschaften fünf repräsentativer Schiffstypen mit Hilfe von CPMC-Modellversuchen. Technical report, Technische Universität Hamburg-Harburg. (in German).

Yao, J. (2015). *On the propeller effect when predicting hydrodynamic forces for manoeuvring using RANS simulations of captive model tests*. PhD thesis, Technical University Berlin.

Yasukawa, H. (1990). A Rankine Panel Method to Calculate Unsteady Ship Hydrodynamic Forces. *Journal of The Society of Naval Architects of Japan*, 168.

Yasukawa, H. (2002). Application of a 3-D Time Domain Panel Method to Ship Seakeeping Problems. In *Proceedings of the 24th ONR Symposium on Naval Hydrodynamics*, Fukuoka.

Yasukawa, H. (2006). Simulations of Ship Maneuvering in Waves (1st report: turning motion. *Journal of the Japan Society of Naval Architects and Ocean Engineers*, 4(0):127–136.

Yasukawa, H. (2008). Simulations of Ship Maneuvering in Waves (2nd report: zig-zag and stopping maneuvers). *Journal of the Japan Society of Naval Architects and Ocean Engineers*, 7(0):163–170.

Yasukawa, H. and Adnan, F. A. (2006). Experimental Study on Wave-Induced Motions and Steady Drift Forces of an Obliquely Moving Ship. *Journal of the Japan Society of Naval Architects and Ocean Engineers*, 3:133–138.

Yasukawa, H., Adnan, F. A., and Nishi, K. (2010). Wave-Induced Motions on a Laterally Drifting Ship. *Ship Technology Research*, 57(2):84–98.

Yasukawa, H., Hirata, N., Matsumoto, A., Kuroiwa, R., and Mizokami, S. (2018). Evaluations of wave-induced steady forces and turning motion of a full hull ship in waves. *Journal of Marine Science and Technology*, 75(1):1–15.

Yasukawa, H. and Nakayama, Y. (2009). 6-DOF motion simulations of a turning ship in regular waves. In *Proceedings of the International Marine Simulator Forum (MARSIM)*. Proceedings of MARSIM.

Yasukawa, H. and Yoshimura, Y. (2014). Introduction of MMG standard method for ship maneuvering predictions. *Journal of Marine Science and Technology*, 20(1):37–52.

Zhang, W., Zou, Z.-J., and Deng, D.-H. (2017). A study on prediction of ship maneuvering in regular waves. *Ocean Engineering*, 137:367–381.

List of Abbreviations

BEM	boundary element method
CDS	central differencing scheme
CPMC	computerised planar motion carriage
DTC	Duisburg test case
HSVA	Hamburg Ship Model Basin
IMO	International Maritime Organisation
LUDS	linear upwind differencing scheme
MMG	Manoeuvring Model Group
MSPP	model self propulsion point
PMM	planar motion mechanism
RANS	Reynolds-averaged Navier-Stokes
RAO	response amplitude operator
TUB	Technical University Berlin
UDS	upwind differencing scheme

Nomenclature

Greek symbols

α		Wave encounter angle, 0° corresponds to head waves
β		Drift angle of the ship
δ		Rudder angle
ϵ_{ijk}		Levi-Civita symbol
ζ_A		Wave amplitude
λ		Wave length
μ		Dynamic viscosity
ξ, η, ζ	ξ_i	Cartesian coordinates in earth fixed coordinate system
ξ_C, η_C, ζ_C	ξ_i^C	Cartesian coordinates of virtual towing carriage origin in earth fixed coordinate system
ξ_O, η_O, ζ_O	ξ_i^O	Cartesian coordinates of ships origin in earth fixed coordinate system
$\xi_{R,l}$, $\eta_{R,l}$, $\zeta_{R,l}$	ξ_l^R	Earth fixed coordinates of endpoint of spring l
$\xi_{R0,l}$, $\eta_{R0,l}$, $\zeta_{R0,l}$	$\xi_{i,l}^{R0}$	Earth fixed coordinates of endpoint of spring l at rest
ρ		Density
φ, θ, ψ		Euler angles (roll, pitch, yaw)
ϕ		Level set function
ψ_C		Euler angle for rotation of virtual towing carriage system relative to the earth fixed coordinate system
ω		Motion period
ω_1, ω_2, ω_3	ω_i	Components of the angular velocity vector in ship fixed coordinate system
$\dot{\omega}_1$, $\dot{\omega}_2$, $\dot{\omega}_3$	$\dot{\omega}_i$	Time derivative of angular velocity vector in ship fixed coordinates

Latin symbols

a_{ni}, b_{ni}		Mean wave force coefficients of the mathematical model
b_i		Cartesian components of external body forces acting on the fluid

c_ϕ		Interpolation factor for density and viscosity
c_R	c_{ij}^R	Spring stiffness matrix (or its components) for spring l
F_x, F_y, F_z	F_i	Components of external forces in ship fixed coordinate system
F_{xH}, F_{yH}, F_{zH}	F_i^H	Components of the hydrodynamic force acting on the hull in ship fixed coordinate system
F_{xW}, F_{yW}, F_{zW}	F_i^W	Components of the weight force acting on the hull in ship fixed coordinate system
F_{xR}, F_{yR}, F_{zR}	F_i^R	Components of the restoring force acting on the hull in ship fixed coordinate system
$F_{xR,l}$, $F_{yR,l}$, $F_{zR,l}$	$F_{i,l}^R$	Components of the restoring force for spring l in ship fixed coordinate system
Fn		Froude number
g		Standard acceleration due to gravity
I_{xx}, I_{xy}, I_{xz}, I_{yy} ...	I_{ij}	Elements of inertia tensor
L_{PP}		Length between perpendiculars
L_r		Reference length for obtaining non-dimensional formulations, usually L_{PP}
m		Mass of the ship
M_x, M_y, M_z	M_i	Components of external moments in ship fixed coordinate system
n		Propeller revolution rate
n^*		Propeller revolution rate factor
n_0		Propeller revolution rate used for determination of coefficient set
p		pressure
r		yaw rate
Rn		Reynolds number
t		Time
t_{90}		Time required for a 90° change of heading during a turning circle
t_{180}		Time required for a 180° change of heading during a turning circle
T	T_{ij}	Transformation matrix (or its components) between ship fixed and earth fixed coordinates

T_C	T_{ij}^C	Transformation matrix (or its components) between carriage fixed and earth fixed coordinates
u, v, w	u_i	Cartesian components of the velocity vector of the origin O in ship fixed coordinates
$\dot{u}$, $\dot{v}$, $\dot{w}$	$\dot{u}_i$	Time derivative of u_i in ship fixed coordinates
$\hat{u}, \hat{v}_1, \hat{v}_2, \hat{r}_1, \hat{r}_2$		Motion amplitudes
u_0		Reference speed for calm water coefficient set, approach speed of the manoeuvre
u_r		Reference velocity for obtaining non-dimensional formulations
u_C, v_C, w_C	u_i^C	Constant Cartesian components of the velocity vector of the origin C of the virtual towing carriage in carriage fixed coordinates
u^*		Artificially reduced forward speed due to propeller revolution rate change
v_i		Cartesian velocity components of the fluid velocity
x, y, z	x_i	Cartesian coordinates in ship fixed coordinate system
x_G, y_G, z_G	x_i^G	Constant Cartesian components of the centre of gravity in the ship fixed coordinate system
$x_{R,l}$, $y_{R,l}$, $z_{R,l}$	$x_{i,l}^R$	Constant components of the application point of the force for spring l in ship fixed coordinate system
$\hat{x}$, $\hat{y}$, $\hat{z}$	$\hat{x}_i$	Cartesian coordinates in virtual towing carriage fixed coordinate system
X, Y, K, N		Longitudinal force, side force, roll moment and yaw moment in hybrid coordinate system
X_u, Y_v, N_{rrr}, ...		Hydrodynamic coefficients of the calm water coefficient set
X_{90}		Longitudinal displacement of a ship at the point of a 90° heading change during a turning circle test (advance)
Y_{90}		Transversal displacement of a ship at the point of a 90° heading change during a turning circle test (transfer)
Y_{180}		Transversal displacement of a ship at the point of a 180° heading change during a turning circle test (tactical diameter)

A. Overview of computations

A.1. Calm water computations without free surface

Table A.1 shows the parameters of the 377 static computations in calm water and Table A.2 contains the parameters of the dynamic tests.

Table A.1.: Overview of static calm water manoeuvring computations

Grid	δ	β	r'	u'	n	count
without bodyforces						
G1	0°, −10°, −20°, −25°, −30°, −35°	0°	0.0	1.0	-	6
G1	0°	10°, 20°	0.0	1.0	-	2
G2	0°, −10°, −20°, −25°, −30°, −35°	0°	0.0	1.0	-	6
G2	0°	10°, 20°	0.0	1.0	-	2
G3	0°, −10°, −20°, −25°, −30°, −35°	0°	0.0	1.0	-	6
G3	0°	10°, 20°	0.0	1.0	-	2
mathematical model						
G2	−35°, −30°, −25°, −20°, −10°, 0°, 10°, 20°, 25°, 30°, 35°	0°	0.0	1.0	8.135 Hz	11
G2	−35°, −30°, −25°, −20°, −10°, 0°, 10°, 20°, 25°, 30°, 35°	−20°	0.0	1.0	8.135 Hz	11
G2	−35°, −30°, −25°, −20°, −10°, 0°, 10°, 20°, 25°, 30°, 35°	−10°	0.0	1.0	8.135 Hz	11
G2	−35°, −30°, −25°, −20°, −10°, 0°, 10°, 20°, 25°, 30°, 35°	10°	0.0	1.0	8.135 Hz	11
G2	−35°, −30°, −25°, −20°, −10°, 0°, 10°, 20°, 25°, 30°, 35°	20°	0.0	1.0	8.135 Hz	11
G2	−35°, −30°, −25°, −20°, −10°, 0°, 10°, 20°, 25°, 30°, 35°	0°	−0.7	1.0	8.135 Hz	11

Grid	δ	β	r'	u'	n	count
G2	−35°, −30°, −25°, −20°, −10°, 0°, 10°, 20°, 25°, 30°, 35°	0°	−0.35	1.0	8.135 Hz	11
G2	−35°, −30°, −25°, −20°, −10°, 0°, 10°, 20°, 25°, 30°, 35°	0°	0.35	1.0	8.135 Hz	11
G2	−35°, −30°, −25°, −20°, −10°, 0°, 10°, 20°, 25°, 30°, 35°	0°	0.7	1.0	8.135 Hz	11
G2	−35°, −30°, −25°, −20°, −10°, 0°, 10°, 20°, 25°, 30°, 35°	0°	0.0	0.3	8.135 Hz	11
G2	−35°, −30°, −25°, −20°, −10°, 0°, 10°, 20°, 25°, 30°, 35°	0°	0.0	0.5	8.135 Hz	11
G2	−35°, −30°, −25°, −20°, −10°, 0°, 10°, 20°, 25°, 30°, 35°	0°	0.0	0.75	8.135 Hz	11
additional combined tests						
G2	0°	−20°, −15°, −10°, −5°, 5°, 10°, 15°, 20°	−0.7	1.0	8.135 Hz	8
G2	0°	−20°, −15°, −10°, −5°, 5°, 10°, 15°, 20°	−0.525	1.0	8.135 Hz	8
G2	0°	−20°, −15°, −10°, −5°, 5°, 10°, 15°, 20°	−0.35	1.0	8.135 Hz	8
G2	0°	−20°, −15°, −10°, −5°, 5°, 10°, 15°, 20°	−0.175	1.0	8.135 Hz	8
G2	0°	−20°, −15°, −10°, −5°, 5°, 10°, 15°, 20°	0.175	1.0	8.135 Hz	8

Grid	δ	β	r'	u'	n	count
G2	0°	−20°, −15°, −10°, −5°, 5°, 10°, 15°, 20°	0.35	1.0	8.135 Hz	8
G2	0°	−20°, −15°, −10°, −5°, 5°, 10°, 15°, 20°	0.525	1.0	8.135 Hz	8
G2	0°	−20°, −15°, −10°, −5°, 5°, 10°, 15°, 20°	0.7	1.0	8.135 Hz	8
additional pure drift / pure yaw tests						
G2	0°	−20°, −18°, −16°, −14°, −12°, −10°, −8°, −6°, −4°, −2°, 2°, 4°, 6°, 8°, 10°, 12°, 14°, 16°, 18°, 20°	0.0	1.0	8.135 Hz	10
G2	0°	0°	−0.7, −0.65, −0.6, −0.55, −0.5, −0.45, −0.4, −0.35, −0.3, −0.25, −0.2, −0.15, −0.1, −0.05, 0.05, 0.1, 0.15, 0.2, 0.25, 0.3, 0.35, 0.4, 0.45, 0.5, 0.55, 0.6, 0.65, 0.7	1.0	8.135 Hz	14
additional propeller revolution rates						
G2	0°, 10°, 20°, 25°, 30°, 35°	0°	0.0	1.0	5.5 Hz	6
G2	0°, 10°, 20°, 25°, 30°, 35°	10°	0.0	1.0	5.5 Hz	6
G2	0°, 10°, 20°, 25°, 30°, 35°	20°	0.0	1.0	5.5 Hz	6

Grid	δ	β	r'	u'	n	count
G2	0°, 10°, 20°, 25°, 30°, 35°	0°	0.0	1.0	7.0 Hz	6
G2	0°, 10°, 20°, 25°, 30°, 35°	10°	0.0	1.0	7.0 Hz	6
G2	0°, 10°, 20°, 25°, 30°, 35°	20°	0.0	1.0	7.0 Hz	6
G2	0°, 10°, 20°, 25°, 30°, 35°	0°	0.0	1.0	7.5 Hz	6
G2	0°, 10°, 20°, 25°, 30°, 35°	10°	0.0	1.0	7.5 Hz	6
G2	0°, 10°, 20°, 25°, 30°, 35°	20°	0.0	1.0	7.5 Hz	6
G2	0°, 10°, 20°, 25°, 30°, 35°	0°	0.0	1.0	8.0 Hz	6
G2	0°, 10°, 20°, 25°, 30°, 35°	10°	0.0	1.0	8.0 Hz	6
G2	0°, 10°, 20°, 25°, 30°, 35°	20°	0.0	1.0	8.0 Hz	6
G2	0°, 10°, 20°, 25°, 30°, 35°	0°	0.0	1.0	8.5 Hz	6
G2	0°, 10°, 20°, 25°, 30°, 35°	10°	0.0	1.0	8.5 Hz	6
G2	0°, 10°, 20°, 25°, 30°, 35°	20°	0.0	1.0	8.5 Hz	6
G2	0°, 10°, 20°, 25°, 30°, 35°	0°	0.0	1.0	9.5 Hz	6
G2	0°, 10°, 20°, 25°, 30°, 35°	10°	0.0	1.0	9.5 Hz	6
G2	0°, 10°, 20°, 25°, 30°, 35°	20°	0.0	1.0	9.5 Hz	6

Table A.2.: Overview of dynamic calm water manoeuvring computations

Grid	T	$\hat{u}'$	$\hat{v}'$	$\hat{r}'$	$\delta t'$
G2	25 s	0.25	-	-	0.00251
G2	25 s	-	0.5	-	0.00251
G2	25 s	-	0.7	-	0.00251
G2	25 s	-	0.4	0.4	0.00251
G2	25 s	-	-0.4	0.7	0.00251
G2	25 s	0.25	-	-	0.00502286
G2	25 s	-	0.5	-	0.00502286
G2	25 s	-	0.7	-	0.00502286
G2	25 s	-	0.4	0.4	0.00502286
G2	25 s	-	-0.4	0.7	0.00502286
G2	25 s	0.25	-	-	0.00125572
G2	25 s	-	0.5	-	0.00125572
G2	25 s	-	0.7	-	0.00125572
G2	25 s	-	0.4	0.4	0.00125572
G2	25 s	-	-0.4	0.7	0.00125572

A.2. Wave computations

Table A.3 lists all computations performed on the grid with the free surface. There are 120 computations in calm water with varying drift angle on 5 grids, 228 computations for the mathematical model and 257 additional computations.

Table A.3.: Overview of computations in incoming waves

Grid	Fn	β	λ'	α	H_W/λ	$\delta t'$	count
Computations in calm water							
G1	0.05	$-10°$, $-5°$, $0°$, $5°$, $10°$					5
G1	0.1	$-10°$, $-5°$, $0°$, $5°$, $10°$					5
G1	0.15	$-10°$, $-5°$, $0°$, $5°$, $10°$					5
G1	0.2	$-10°$, $-5°$, $0°$, $5°$, $10°$					5
G1	0.25	$-10°$, $-5°$, $0°$, $5°$, $10°$					5
G2	0.05	$-10°$, $-5°$, $0°$, $5°$, $10°$					5
G2	0.1	$-10°$, $-5°$, $0°$, $5°$, $10°$					5
G2	0.15	$-10°$, $-5°$, $0°$, $5°$, $10°$					5
G2	0.2	$-10°$, $-5°$, $0°$, $5°$, $10°$					5
G2	0.25	$-10°$, $-5°$, $0°$, $5°$, $10°$					5

Grid	Fn	β	λ'	α	H_W/λ	$\delta t'$	count
G3	0.05	$-10°$, $-5°$, $0°$, $5°$, $10°$					5
G3	0.075	$-10°$, $-5°$, $0°$, $5°$, $10°$					5
G3	0.1	$-10°$, $-5°$, $0°$, $5°$, $10°$					5
G3	0.15	$-10°$, $-5°$, $0°$, $5°$, $10°$					5
G3	0.2	$-10°$, $-5°$, $0°$, $5°$, $10°$					5
G3	0.25	$-10°$, $-5°$, $0°$, $5°$, $10°$					5
G4	0.05	$-10°$, $-5°$, $0°$, $5°$, $10°$					5
G4	0.075	$-10°$, $-5°$, $0°$, $5°$, $10°$					5
G4	0.1	$-10°$, $-5°$, $0°$, $5°$, $10°$					5
G4	0.15	$-10°$, $-5°$, $0°$, $5°$, $10°$					5
G4	0.2	$-10°$, $-5°$, $0°$, $5°$, $10°$					5
G4	0.25	$-10°$, $-5°$, $0°$, $5°$, $10°$					5

Grid	Fn	β	λ'	α	H_W/λ	$\delta t'$	count
G5	0.05	$-10°$, $-5°$, $0°$, $5°$, $10°$					5
G5	0.075	$-10°$, $-5°$, $0°$, $5°$, $10°$					5
Computations for mathematical model							
G4	0.05	$0°$	0.5	$0°$, $15°$, $30°$, $45°$, $60°$, $75°$, $90°$, $105°$, $120°$, $135°$, $150°$, $165°$, $180°$	0.040	0.003	13
G4	0.05	$0°$	0.7	$0°$, $15°$, $30°$, $45°$, $60°$, $75°$, $90°$, $105°$, $120°$, $135°$, $150°$, $165°$, $180°$	0.029	0.003	13
G4	0.05	$0°$	1.0	$0°$, $15°$, $30°$, $45°$, $60°$, $75°$, $90°$, $105°$, $120°$, $135°$, $150°$, $165°$, $180°$	0.020	0.003	13
G4	0.075	$0°$	0.5	$0°$, $5°$, $10°$, $15°$, $20°$, $25°$, $30°$, $35°$, $40°$, $45°$, $50°$, $55°$, $60°$, $65°$, $70°$, $75°$, $80°$, $85°$, $90°$, $95°$, $100°$, $105°$, $110°$, $115°$, $120°$, $125°$, $130°$, $135°$, $140°$, $145°$, $150°$, $155°$, $160°$, $165°$, $170°$, $175°$, $180°$	0.040	0.002	37
G4	0.075	$0°$	0.7	$0°$, $5°$, $10°$, $15°$, $20°$, $25°$, $30°$, $35°$, $40°$, $45°$, $50°$, $55°$, $60°$, $65°$, $70°$, $75°$, $80°$, $85°$, $90°$, $95°$, $100°$, $105°$, $110°$, $115°$, $120°$, $125°$, $130°$, $135°$, $140°$, $145°$, $150°$, $155°$, $160°$, $165°$, $170°$, $175°$, $180°$	0.029	0.002	37

Grid	Fn	β	λ'	α	H_W/λ	$\delta t'$	count
G4	0.075	0°	1.0	0°, 5°, 10°, 15°, 20°, 25°, 30°, 35°, 40°, 45°, 50°, 55°, 60°, 65°, 70°, 75°, 80°, 85°, 90°, 95°, 100°, 105°, 110°, 115°, 120°, 125°, 130°, 135°, 140°, 145°, 150°, 155°, 160°, 165°, 170°, 175°, 180°	0.020	0.002	37
G4	0.10	0°	0.5	0°, 15°, 30°, 45°, 60°, 75°, 90°, 105°, 120°, 135°, 150°, 165°, 180°	0.040	0.008	13
G4	0.10	0°	0.7	0°, 15°, 30°, 45°, 60°, 75°, 90°, 105°, 120°, 135°, 150°, 165°, 180°	0.029	0.008	13
G4	0.10	0°	1.0	0°, 15°, 30°, 45°, 60°, 75°, 90°, 105°, 120°, 135°, 150°, 165°, 180°	0.020	0.008	13
G4	0.15	0°	0.5	0°, 15°, 30°, 45°, 60°, 75°, 90°, 105°, 120°, 135°, 150°, 165°, 180°	0.040	0.008	13
G4	0.15	0°	0.7	0°, 15°, 30°, 45°, 60°, 75°, 90°, 105°, 120°, 135°, 150°, 165°, 180°	0.029	0.008	13
G4	0.15	0°	1.0	0°, 15°, 30°, 45°, 60°, 75°, 90°, 105°, 120°, 135°, 150°, 165°, 180°	0.020	0.008	13
Computations with varying wave steepness							
G4	0.15	0°	1.0	0°, 30°, 60°, 90°, 120°, 150°, 180°	0.01	0.008	7
G4	0.15	0°	0.5	0°, 15°, 30°, 45°, 60°, 75°, 90°, 105°, 120°, 135°, 150°, 165°, 180°	0.02	0.008	13
G4	0.15	0°	0.7	0°, 15°, 30°, 45°, 60°, 75°, 90°, 105°, 120°, 135°, 150°, 165°, 180°	0.02	0.008	13

Grid	Fn	β	λ'	α	H_W/λ	$\delta t'$	count
G4	0.15	0°	0.5	0°, 30°, 60°, 90°, 120°, 150°, 180°	0.03	0.008	7
G4	0.15	0°	0.7	0°, 30°, 60°, 90°, 120°, 150°, 180°	0.03	0.008	7
G4	0.15	0°	1.0	0°, 30°, 60°, 90°, 120°, 150°, 180°	0.03	0.008	7
Computations with varying drift angle							
G4	0.15	−10°	0.5	0°, 30°, 60°, 90°, 120°, 150°, 180°	0.040	0.008	7
G4	0.15	−10°	0.7	0°, 30°, 60°, 90°, 120°, 150°, 180°	0.029	0.008	7
G4	0.15	−10°	1.0	0°, 30°, 60°, 90°, 120°, 150°, 180°	0.020	0.008	7
G4	0.15	−5°	0.5	0°, 30°, 60°, 90°, 120°, 150°, 180°	0.040	0.008	7
G4	0.15	−5°	0.7	0°, 30°, 60°, 90°, 120°, 150°, 180°	0.029	0.008	7
G4	0.15	−5°	1.0	0°, 30°, 60°, 90°, 120°, 150°, 180°	0.020	0.008	7
G4	0.15	5°	0.5	0°, 30°, 60°, 90°, 120°, 150°, 180°	0.040	0.008	7
G4	0.15	5°	0.7	0°, 30°, 60°, 90°, 120°, 150°, 180°	0.029	0.008	7
G4	0.15	5°	1.0	0°, 30°, 60°, 90°, 120°, 150°, 180°	0.020	0.008	7
G4	0.15	10°	0.5	0°, 30°, 60°, 90°, 120°, 150°, 180°	0.040	0.008	7
G4	0.15	10°	0.7	0°, 30°, 60°, 90°, 120°, 150°, 180°	0.029	0.008	7
G4	0.15	10°	1.0	0°, 30°, 60°, 90°, 120°, 150°, 180°	0.020	0.008	7
Computations for validation with experiments from Yasukawa							
G4	0.15	0°	0.6, 0.7, 0.8, 0.85, 0.9, 0.95, 1.0, 1.05, 1.1, 1.15, 1.2, 1.4, 1.5	0°	0.02	0.008	13

Grid	Fn	β	λ'	α	H_W/λ	$\delta t'$	count
Computations with $k'_{yy} = 0.25$							
G4	0.15	0°	0.6, 0.7, 0.8, 0.85, 0.9, 0.95, 1.0, 1.05, 1.1, 1.15, 1.2, 1.4, 1.5	0°	0.02	0.008	13
Computations with $k'_{yy} = 0.3$							
G4	0.15	0°	0.6, 0.7, 0.8, 0.85, 0.9, 0.95, 1.0, 1.05, 1.1, 1.15, 1.2, 1.4, 1.5	0°	0.02	0.008	13
Computations with $k'_{yy} = 0.35$							
G4	0.15	0°	0.6, 0.7, 0.8, 0.85, 0.9, 0.95, 1.0, 1.05, 1.1, 1.15, 1.2, 1.4, 1.5	0°	0.02	0.008	13
Computations for validation with experiments from Fujii							
G4	0.15	0°	0.7	0°, 30°, 60°, 90°, 120°, 150°, 180°	0.02	0.008	7
G4	0.15	0°	0.85	0°, 30°, 60°, 90°, 120°, 150°, 180°	0.02	0.008	7
G4	0.15	0°	1.0	0°, 30°, 60°, 90°, 120°, 150°, 180°	0.02	0.008	7
G4	0.15	0°	1.15	0°, 30°, 60°, 90°, 120°, 150°, 180°	0.02	0.008	7
G4	0.15	0°	1.3	0°, 30°, 60°, 90°, 120°, 150°, 180°	0.02	0.008	7
G4	0.15	0°	1.5	0°, 30°, 60°, 90°, 120°, 150°, 180°	0.02	0.008	7
Computations for validation of mathematical model							

Grid	Fn	β	λ'	α	H_W/λ	$\delta t'$	count
G4	0.15	0°	0.65	23.8°, 72°	0.031	0.0008	2
G4	0.15	0°	0.8	0.0°	0.025	0.0008	1
G4	0.15	0°	0.85	0.0°, 23.8°, 49.3°	0.024	0.0008	3
G4	0.15	0°	0.9	23.8°, 49.3°	0.022	0.0008	2
Computations for grid dependence study							
G1	0.15	0°	0.5, 1.0	0.0°	0.02	0.0008	2
G2	0.15	0°	0.5, 1.0	0.0°	0.02	0.0008	2
G3	0.15	0°	0.5, 1.0	0.0°	0.02	0.0008	2
G4	0.15	0°	0.5, 1.0	0.0°	0.02	0.0008	2
G5	0.15	0°	0.5, 1.0	0.0°	0.02	0.0008	2
G2	0.15	0°	0.5	45.0°	0.02	0.0008	1
G3	0.15	0°	0.5	45.0°	0.02	0.0008	1
G4	0.15	0°	0.5	45.0°	0.02	0.0008	1
G5	0.15	0°	0.5	45.0°	0.02	0.0008	1
Computations for timestep dependence study							
G2	0.15	0°	1.0	0.0°	0.02	0.001, 0.0014, 0.0016	3

B. Additional Verification

B.1. Convergence analysis

A verification study as proposed by ITTC (2002) is used to compute the uncertainties U_g and U_t due to the spacial and temporal resolution. For transient computations it should be noted that according to Oberhagemann (2016), the individual uncertainties U_g and U_t cannot be seen as independent from each other and thus it is not possible to determine the accuracy of the computation without a combined temporal and spacial approach. For the static cases the approach still seems valid and since no quantitative assessment of the uncertainty of the computation is to be given, the evaluation is still performed in the same way as proposed by ITTC (2002).

In the following section the procedure will be shown for the spacial uncertainty, it can be applied for the temporal uncertainty as well. The convergence ratio R_G is:

$$R_G = \epsilon_{21}/\epsilon_{32} \tag{B.1}$$

with $\epsilon_{ik} = S_i - S_k$. There is a monotonic convergence for $0 < R_G < 1$ and an oscillatory for $-1 < R_G < 0$. In case of a monotonic convergence, the order of accuracy p_{RE} can be computed using the refinement ratio r:

$$p_{\mathrm{RE}} = \frac{\ln(\epsilon_{32}/\epsilon_{21})}{\ln(r)} \tag{B.2}$$

The error estimate δ_{RE} is computed using a Richardson Extrapolation:

$$\delta_{\mathrm{RE}} = \frac{\epsilon_{21}}{r^{p_{\mathrm{RE}}} - 1} \tag{B.3}$$

Using this error estimate, the generalised Richardson Extrapolated solution S_{RE} can be computed:

$$S_{\mathrm{RE}} = S_1 - \delta_{\mathrm{RE}} \tag{B.4}$$

Following ITTC (2002), a factor of safety $F_{\mathrm{S}} = 1.25$ is used to compute the uncertainty of the solution:

$$U_G = F_{\mathrm{S}}|\delta_{\mathrm{RE}}| \tag{B.5}$$

B.2. Calm water computations without free surface

B.2.1. Grid convergence

In order to check the grid convergence of the computations for the calm water coefficient set, selected computations have been performed on three different grids. The finest grid has 2.7 Million cells, the medium one 1.2 Million and the coarse grid 360.000 cells. The resulting (average) refinement factor r between these grids is 1.42.

The computations selected for the grid dependence study consider a steady straight and steady oblique towing test as well as a steady straight towing test with the rudder deflected $-35°$ to starboard. The results are shown in Figures B.1, B.2 and B.3 respectively. Table B.1 shows the computed results for all considered cases on the coarse (S_3), medium (S_2) and fine grid (S_1).

Table B.1.: Results of grid dependence study for calm water grid

	S3	S2	S1	R_g	U_g
Resistance					
F_F	-2.958 N	-3.157 N	-3.202 N	0.229	0.52 %
F_P	-0.613 N	-0.454 N	-0.414 N	0.256	4.38 %
F_T	-3.571 N	-3.611 N	-3.616 N	0.119	0.02 %
Oblique towing ($\beta = 20°$)					
F_y	15.295 N	14.027 N	13.506 N	0.410	3.45 %
M_z	15.881 Nm	14.970 Nm	14.553 Nm	0.458	3.11 %
Rudder deflection ($\delta = -35°$)					
F_y	-2.537 N	-2.603 N	-2.622 N	0.286	0.36 %
M_z	4.260 Nm	4.356 Nm	4.377 Nm	0.219	0.17 %

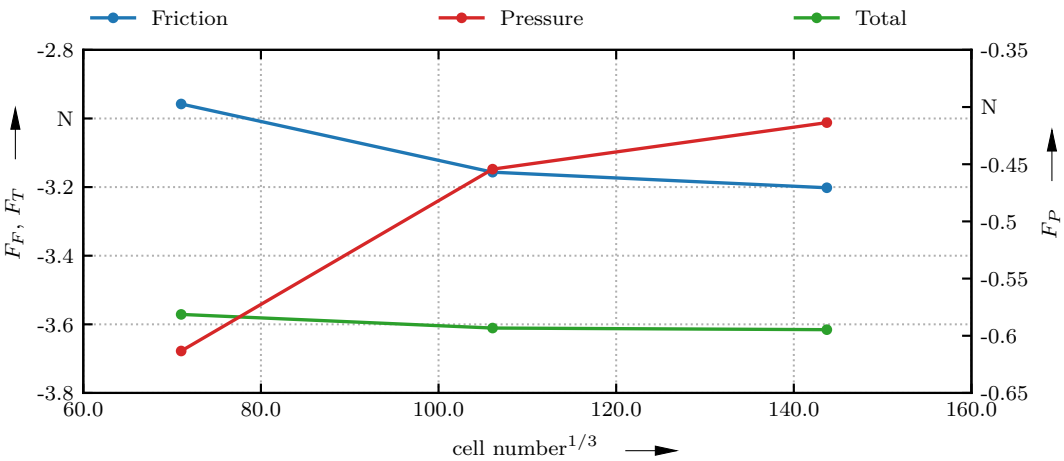

(a) Side force

Figure B.1.: Grid convergence study for resistance

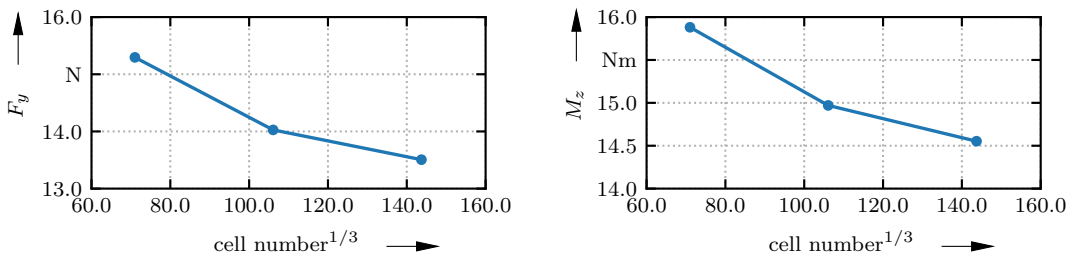

(a) Side force

(b) Yaw moment

Figure B.2.: Grid convergence study for case with $\beta = 20°$

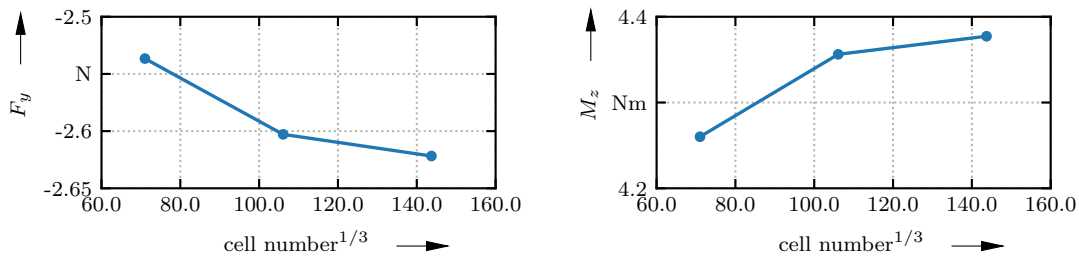

(a) Side force

(b) Yaw moment

Figure B.3.: Grid convergence study for case with $\delta = -35°$

B.2.2. Iterative convergence

An exemplary verification of the iterative convergence of each computation is shown in Figure B.4. It can be seen that the global forces converge towards a constant value, while the residuals keep dropping. This behaviour was observed in most cases. For some situations no stationary solution was obtained due to oscillating forces of the body force model and thus the residuals were stagnating, see Figure B.5. It should be noted however, that also in this case the residuals already dropped 5 orders of magnitude and keep dropping after the side force is converged already and the oscillation in the longitudinal force and thrust is negligible.

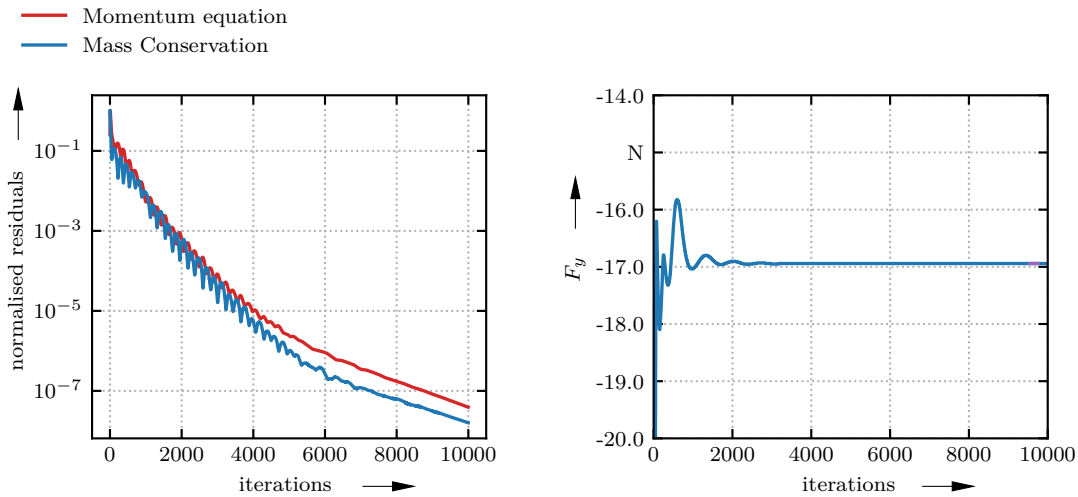

Figure B.4.: Iterative convergence of calm water case with $\delta = -10°$ and $\beta = -10°$

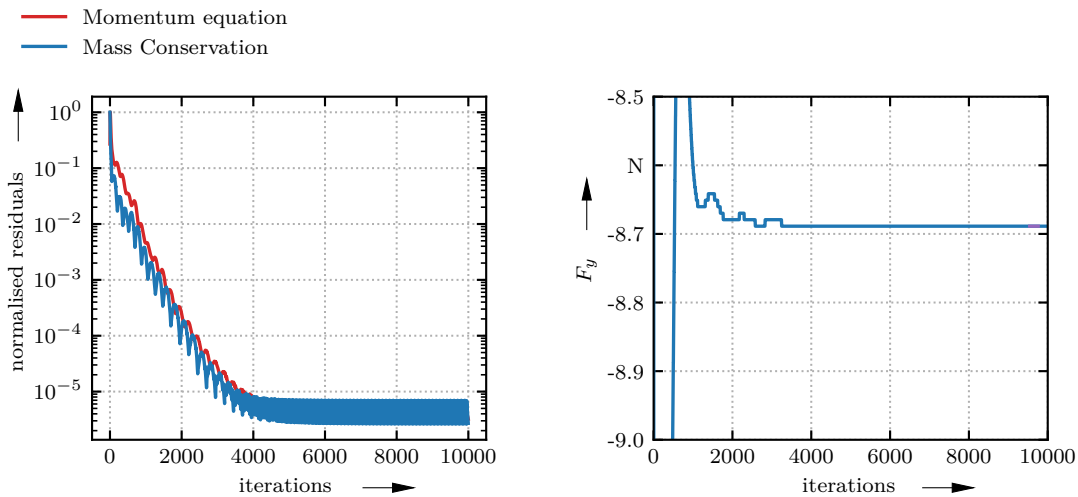

Figure B.5.: Iterative convergence of calm water case with $\delta = -10°$ and $r' = -0.35°$

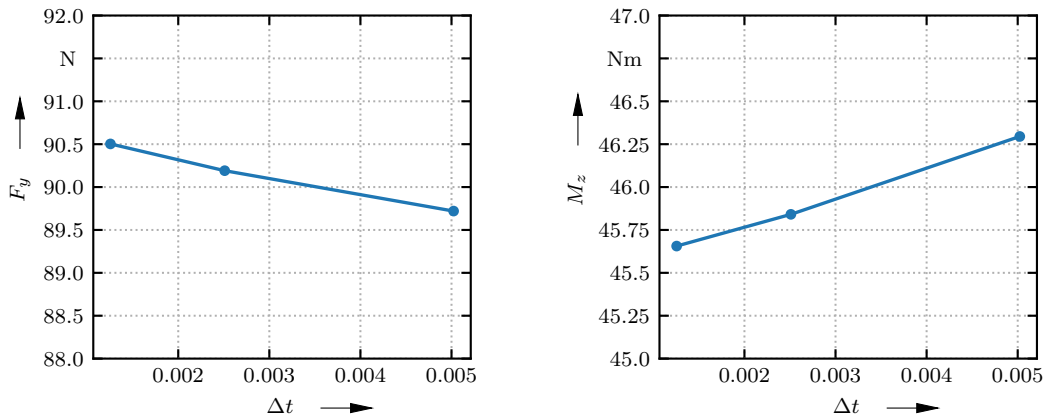

Figure B.6.: Results of timestep dependence study for pure sway test on calm water grid

B.2.3. Time step convergence

The timestep convergence study for the calm water case was performed on the medium grid with 1.2 Million cells for all five dynamic tests. In order to check the timestep convergence, the side force and yaw moment was evaluated at the time of maximum negative sway velocity. The results are shown in Table B.2 and Figure B.6. Please remember that the uncertainty is only to indicate a range and cannot be used to determine the total uncertainty of the combined spacial and temporal uncertainty as explained in Section B.1.

Table B.2.: Results of timestep dependence study for pure sway test on calm water grid

	S3	S2	S1	R_t	U_t
F_y	89.720 N	90.191 N	90.503 N	0.662	0.84 N
M_z	46.295 Nm	45.841 Nm	45.656 Nm	0.407	0.35 N

B.2.4. Verification y+

To check that the y^+ value lies inside the valid range, the distribtion on the ship hull is displayed in Figure B.7. As can be seen, the chosen spacing of the first cell on the wall is sufficient.

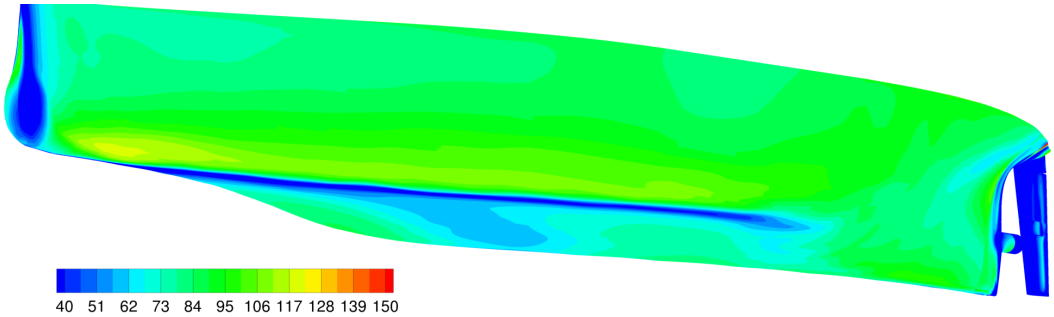

(a) Fine grid

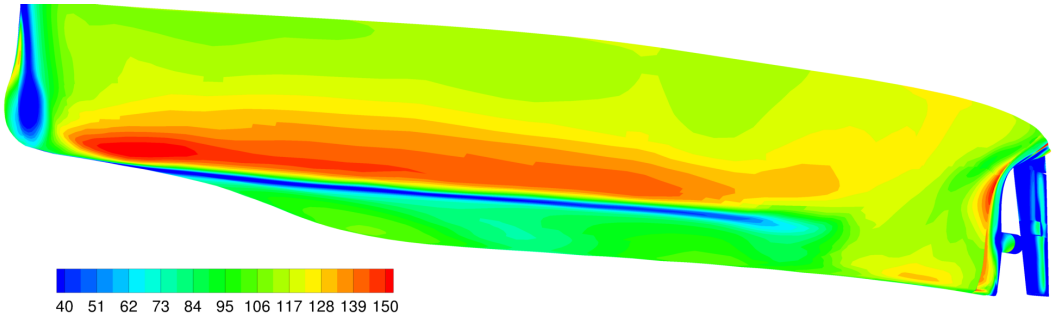

(b) Medium grid

Figure B.7.: y^+ distribution on the ship hull for oblique inflow condition with $\beta = 20°$

B.3. Calm water computations with free surface

B.3.1. Grid convergence without waves

The grid convergence analysis for the calm water case is performed in the fixed conditions for different grid refinement levels ranging from 360.000, 1.2 Million, 2.9 Million, 4.2 Million to 5.9 Million. Figure B.8 shows dependence of the pressure, viscous and total longituninal force on the grid resolution. For analysing the uncertainty, only the three finest grids were used, having an average refinement ratio of $r_G = 0.14$. The results are shown in Table B.3.

Table B.3.: Results of grid dependence study for wave grid

	S3	S2	S1	R_g	U_g
F_F	-3.030 N	-3.087 N	-3.116 N	0.503	1.14 %
F_P	-0.704 N	-0.659 N	-0.650 N	0.199	0.43 %
F_T	-3.735 N	-3.746 N	-3.766 N	1.741	

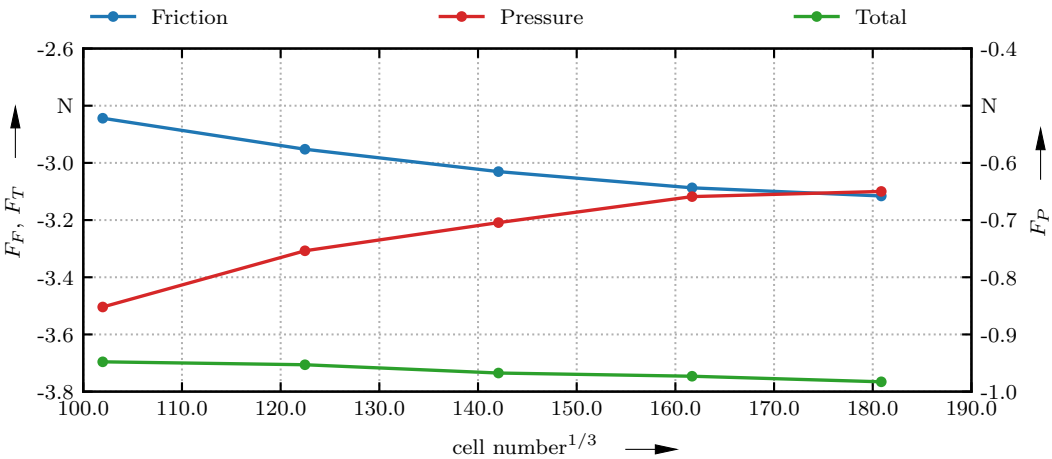

Figure B.8.: Grid convergence study in calm water (wave grid)

B.3.2. Grid convergence with wave

Some cases with incoming waves have been computed on five different grid refinement levels for two head wave cases with $\lambda' = 0.5$ and $\lambda' = 1.0$ and on four grid refinement levels for two oblique incoming wave with $\lambda' = 0.5$ and $\alpha = 45°$ and $\lambda' = 1.0, \alpha = 135°$. It should be noted that for transient cases, the evaluation of uncertainties should not be performed due to the coupling between spacial and temporal resolution (Oberhagemann, 2016). When looking at the results shown in Figure B.9, no monotonic convergence can be observed for any case. It should be noted however, that the differences between the grids are relatively small (e.g. 2% for $\lambda' = 0.5$, $\alpha = 0°$) and the error introduced by averaging is relatively large (error bars).

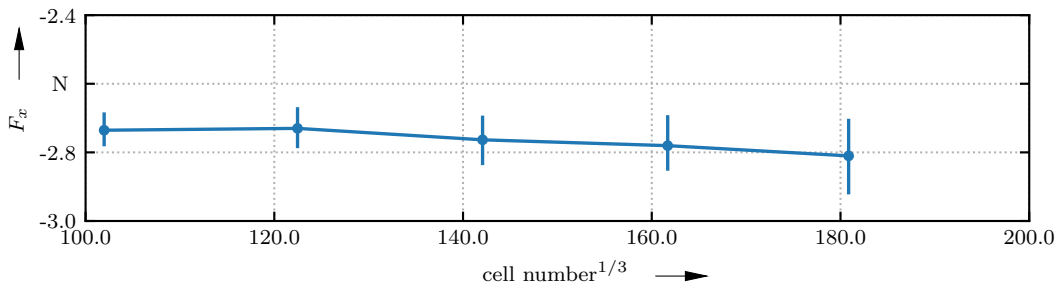

(a) Added resistance for $\lambda' = 0.5, \alpha = 0°$

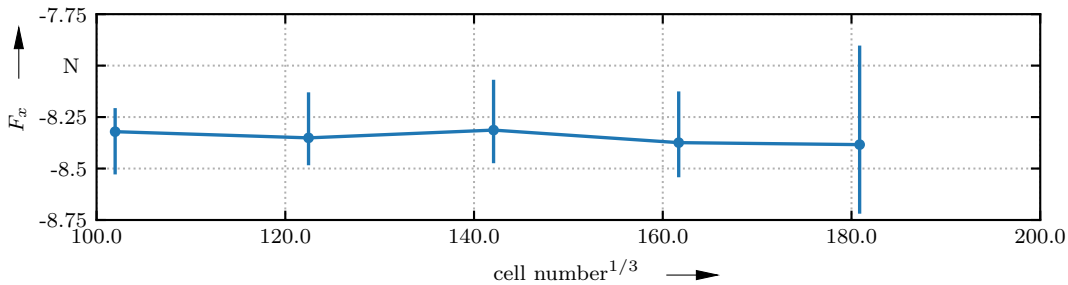

(b) Added resistance for $\lambda' = 1.0, \alpha = 0°$

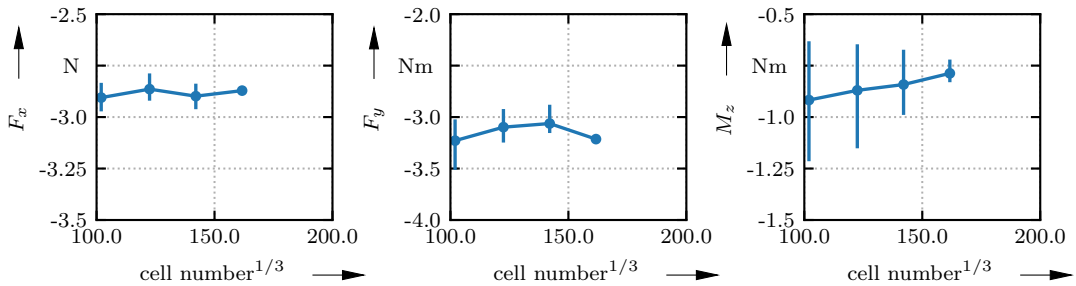

(c) Mean wave forces for $\lambda' = 0.5, \alpha = 45°$

Figure B.9.: Grid convergence study in waves

B.3.3. Time step convergence

In order to check the timestep convergence, selected computations have been repeated with varying timesteps. The results are shown in Figure B.10. As explained before, no uncertainty evaluation should be performed for transient computations due to the coupling between spatial and temporal resolution (Oberhagemann, 2016). It should be noted that like for other codes, an influence of the time step size on the results can be observed, if the time step is chosen too small. The range covered in this study was therefore selected by experience.

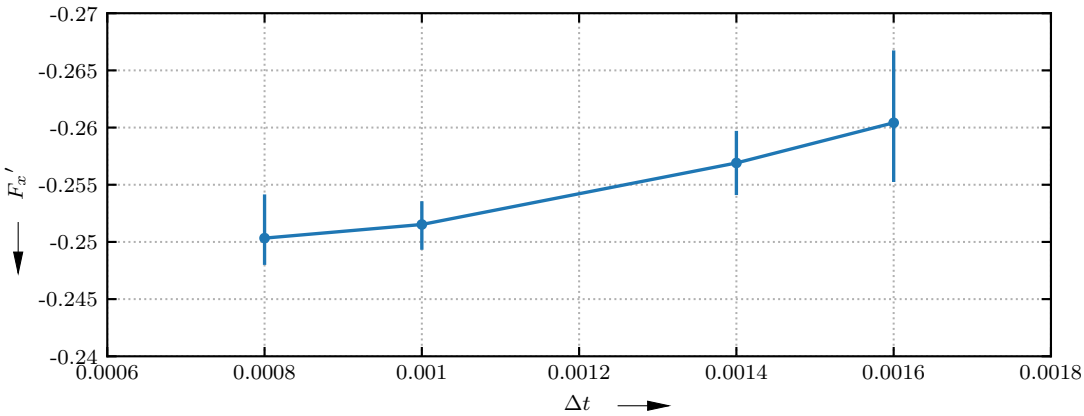

Figure B.10.: Analysis of the influence of the time step size for case with $\lambda' = 1.0$, $\zeta' = 0.01$, $\alpha = 0°$, Fn=0.15

B.3.4. Iterative convergence

Figure B.11 shows as an example the iterative convergence for a computation with an incoming head and beam wave with $\lambda' = 1.0°$ and $\zeta' = 0.01$. As can be seen for both cases there is a quite good iterative convergence obtained. This was also the case for all other computations.

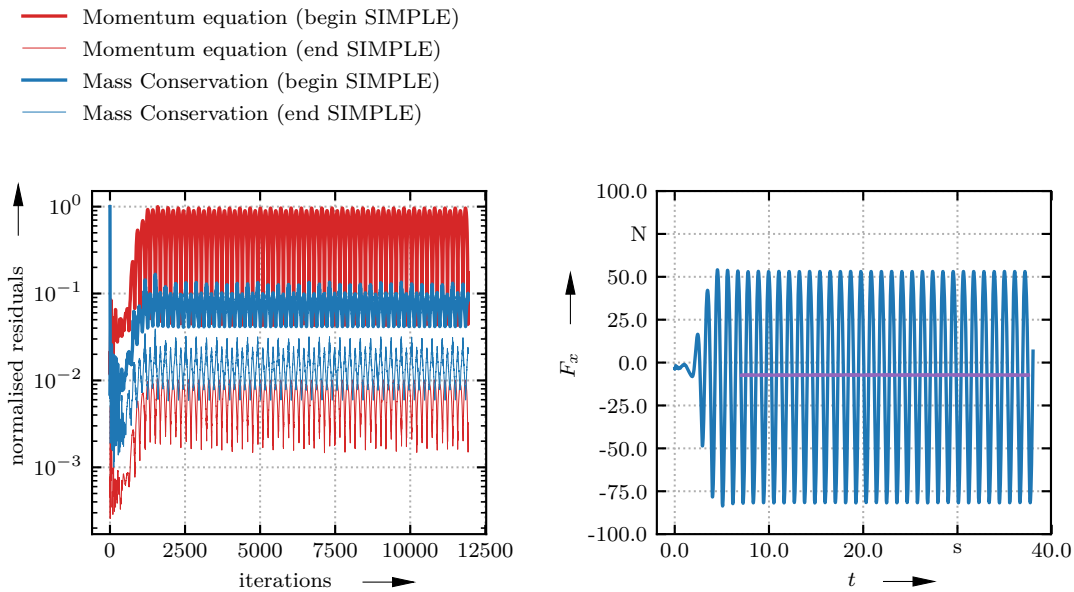

(a) head wave with $\lambda' = 1.0°$ and $\zeta' = 0.01$

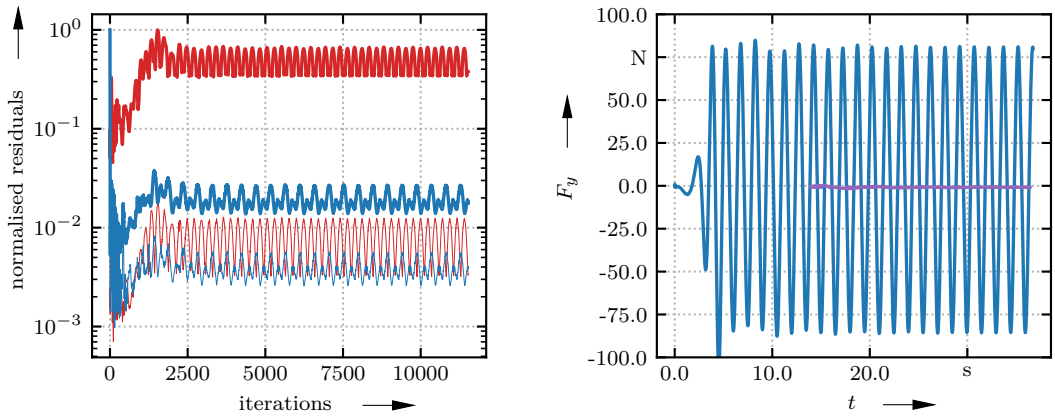

(b) beam wave with $\lambda' = 1.0°$ and $\zeta' = 0.01$

Figure B.11.: Iterative convergence of computation with incoming head wave with $\lambda' = 1.0°$ and $\zeta' = 0.01$

B.3.5. Verification y+

Figure B.12 shows the y^+ distribution on the ship hull for the fine (G1) and medium (G4) grid. As can be seen, the values lies within an acceptable range on both grids.

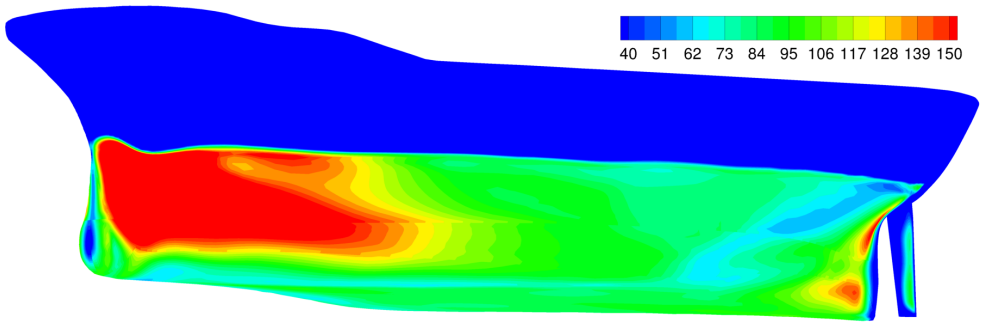

(a) Fine grid (G1)

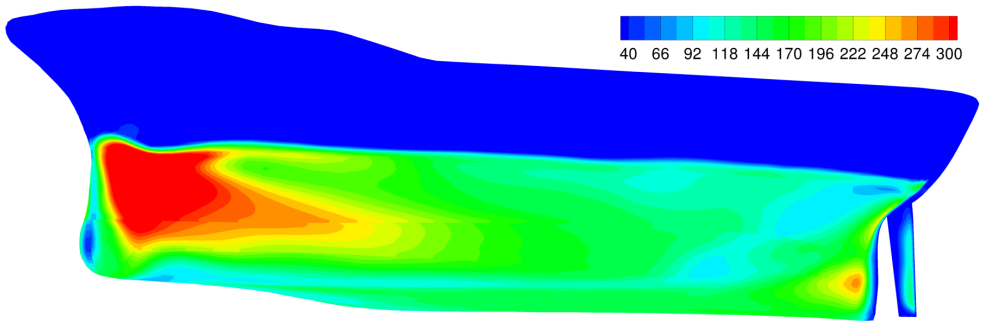

(b) Medium grid (G4)

Figure B.12.: y^+ distribution on the ship hull for straight ahead motion with free surface

B.3.6. Check of level set reinitialisation

The reinitialisation of the level set function was checked for some representative cases. The result for a case with an incoming head wave with $\lambda' = 1.0$ and $\zeta' = 0.01$ is shown in Figure B.13. Since the width of the transition region (α) is determined dynamically throughout the simulations depending on the maximum cell height in the free surface, the maximal width of the transition region is shown in addition to its normal width (white region). The spreading of the level set function was in such an acceptable range for all evaluated computations.

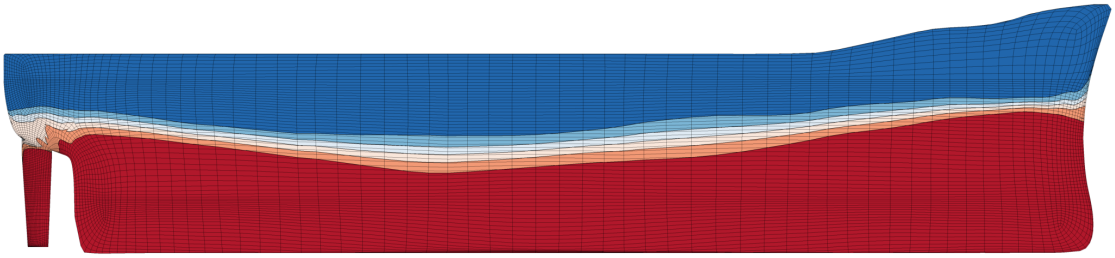

(a) Fine grid

Figure B.13.: Spreading of free surface on the ship hull for incoming head wave with $\lambda' = 1.0$ and $\zeta' = 0.01$

B.3.7. Verification of wave quality

In order to check, if the wave in the numerical domain holds all desired physical properties (e.g. amplitude, frequency and length), a slice is extracted from the domain at 0.7 ship length toward the incoming wave. It should be noted however, that in many cases it is hard to draw conclusions from this data. Especially in long waves at low speed, the disturbance of the wave field due to the presence of the ship is propagated upstream and thus no undisturbed wave field is to be expected. This is also the case of oblique incoming waves, where the reflections from the ship can also be seen in the region of the incoming wave, see Section 3.2.1.

Therefore the verification is seen most significant for the case of higher forward speeds during which the reflections are transported out of the domain. From these simulations it can be concluded that the selected grid is sufficient for the accurate simulation of the chosen waves. Another approach would be to perform simulations without the ship on a grid with similar properties. However, since the free surface moves in the computational domain due to the heave and pitch motion of the ship, the results from these simulations would be seen as less accurate than the approach selected here.

Figure B.14 shows as an example the evaluated slices for three different wave length, amplitudes and encounter angles. As can be seen, a good quality was obtained in all situations.

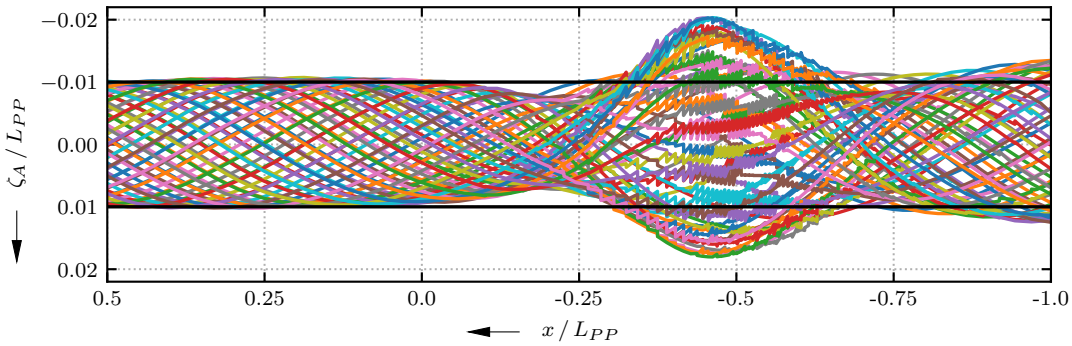

(a) $\lambda' = 1.0$, $\alpha = 0°$, $\zeta' = 0.01$, Fn $= 0.15$

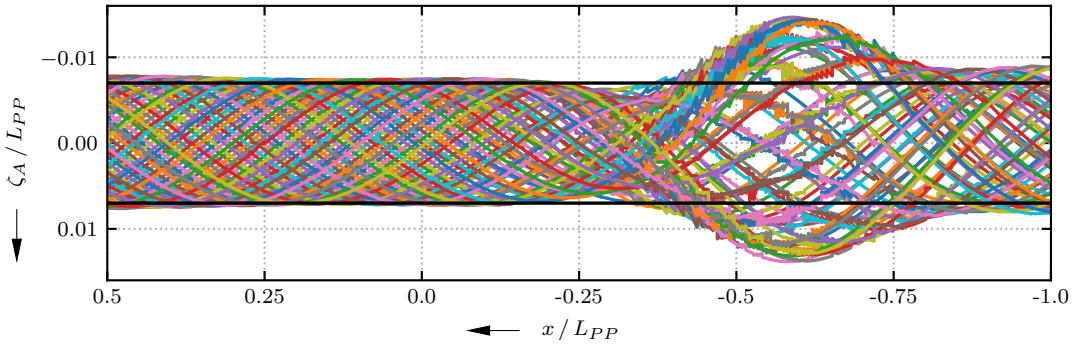

(b) $\lambda' = 0.7$, $\alpha = 30°$, $\zeta' = 0.007$, Fn $= 0.15$

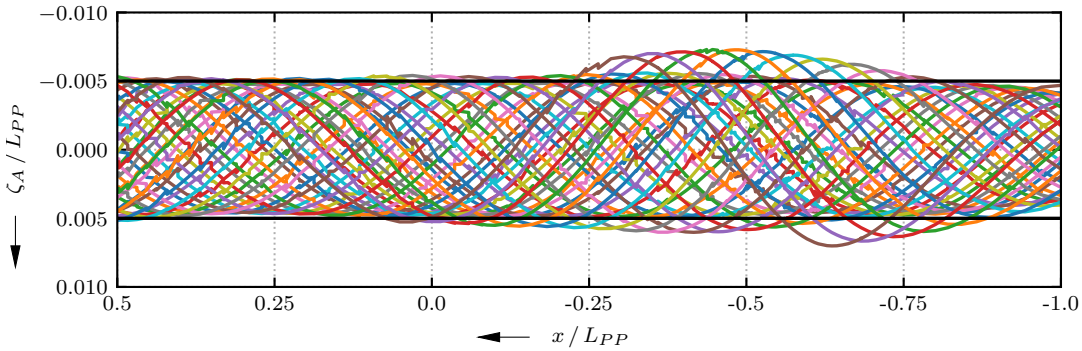

(c) $\lambda' = 0.5$, $\alpha = 135°$, $\zeta' = 0.005$, Fn $= 0.15$

Figure B.14.: Wavequality evaluated at $y / L_{PP} = 0.7$

C. Additional results

C.1. Reconstruction calm water

Figures C.1, C.2 and C.3 show the reconstructions of the computed traces for the static pure δ, r and Δu tests respectively. Figures C.4, C.5 and C.6 show the reconstructions of the combined v-δ, r-δ and Δu-δ tests. The reconstructions of the dyanmic surge, yaw, sway-yaw and yaw-sway tests can be found in figure C.7, C.8, C.9, C.10. All tests are performed on the medium grid, the details (motion period, amplitudes) are described in section 3.1.1.

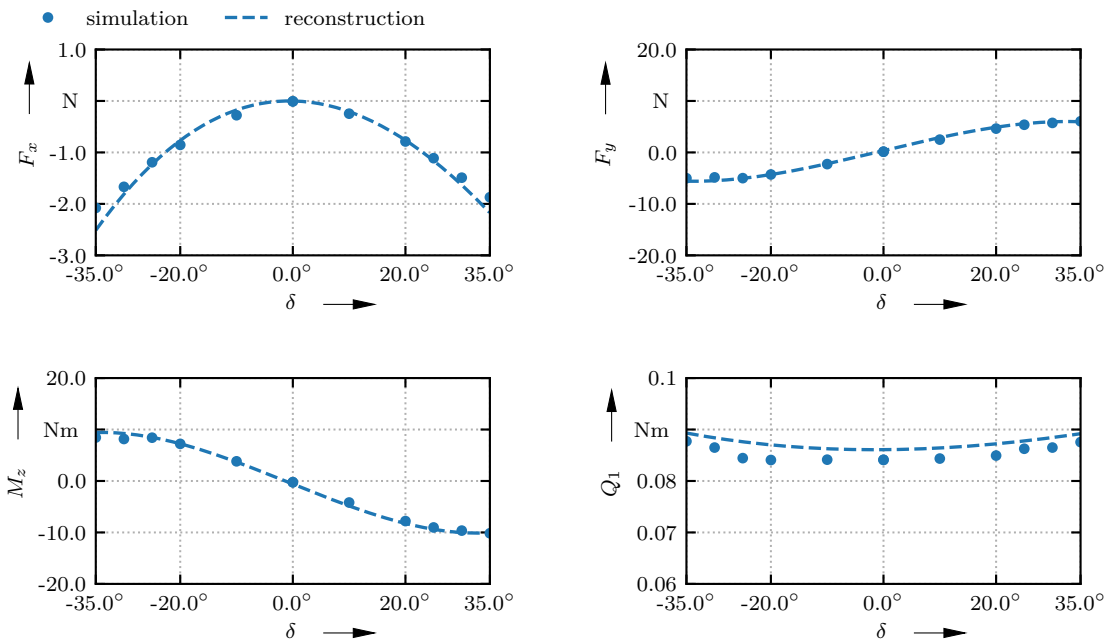

Figure C.1.: Reconstruction of static δ tests

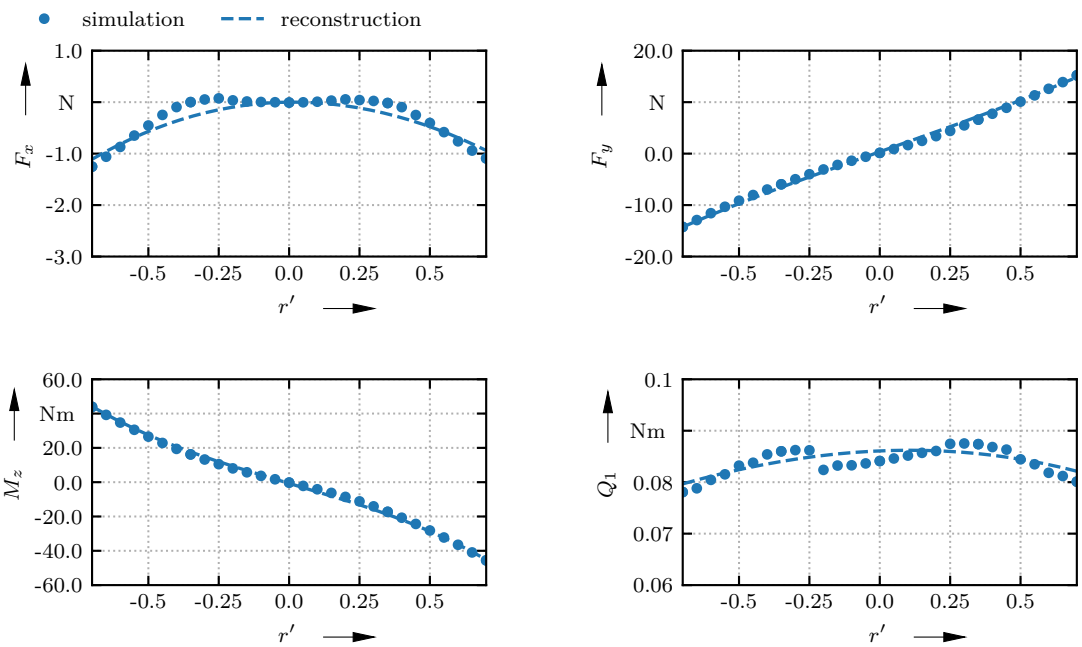

Figure C.2.: Reconstruction of static r tests

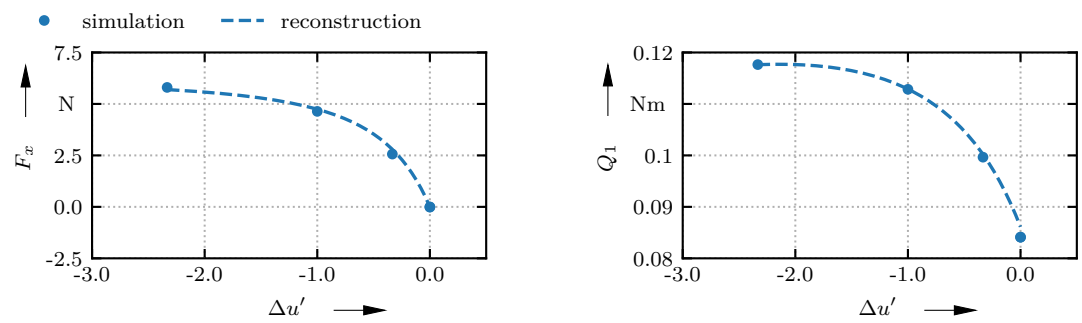

Figure C.3.: Reconstruction of static Δu tests

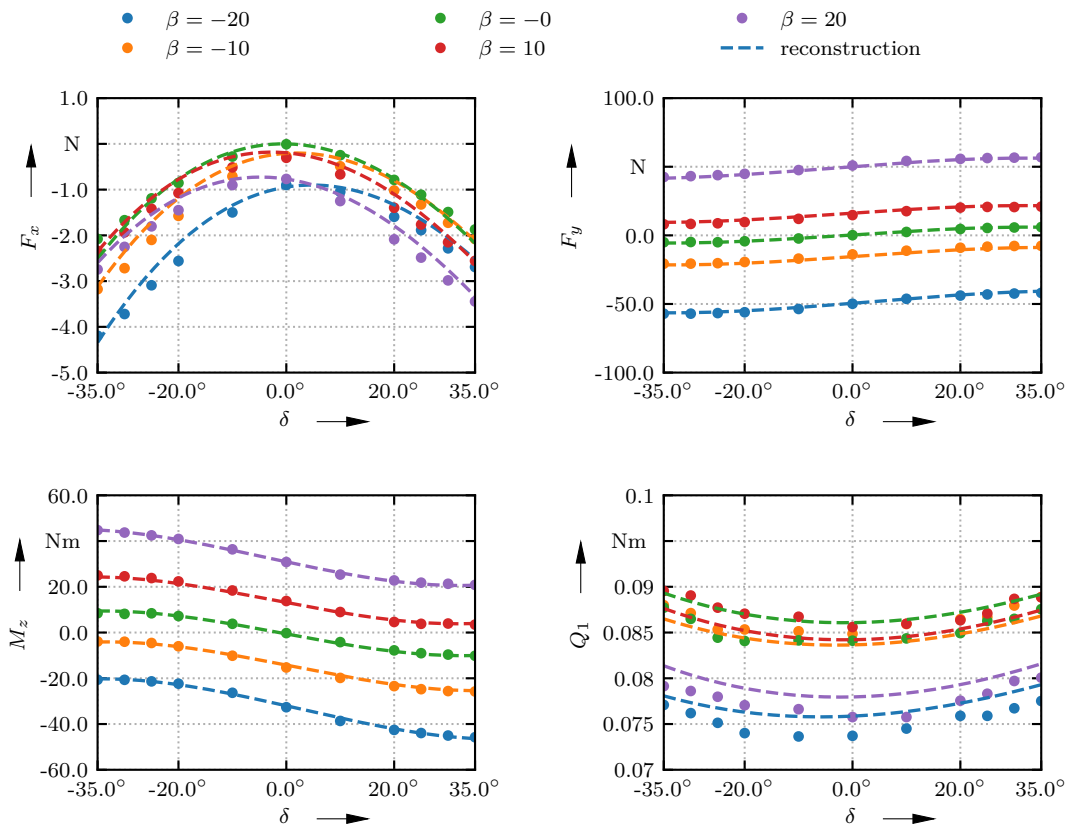

Figure C.4.: Reconstruction of static combined δ-v tests

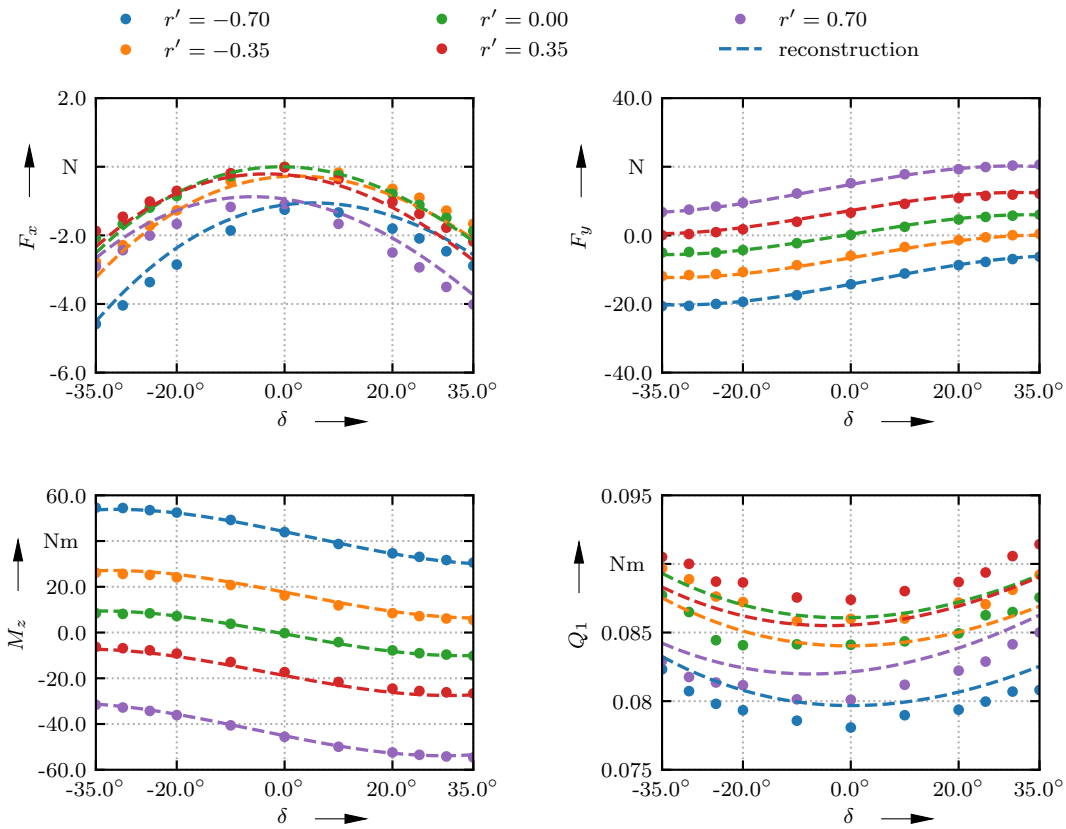

Figure C.5.: Reconstruction of static combined δ-r tests

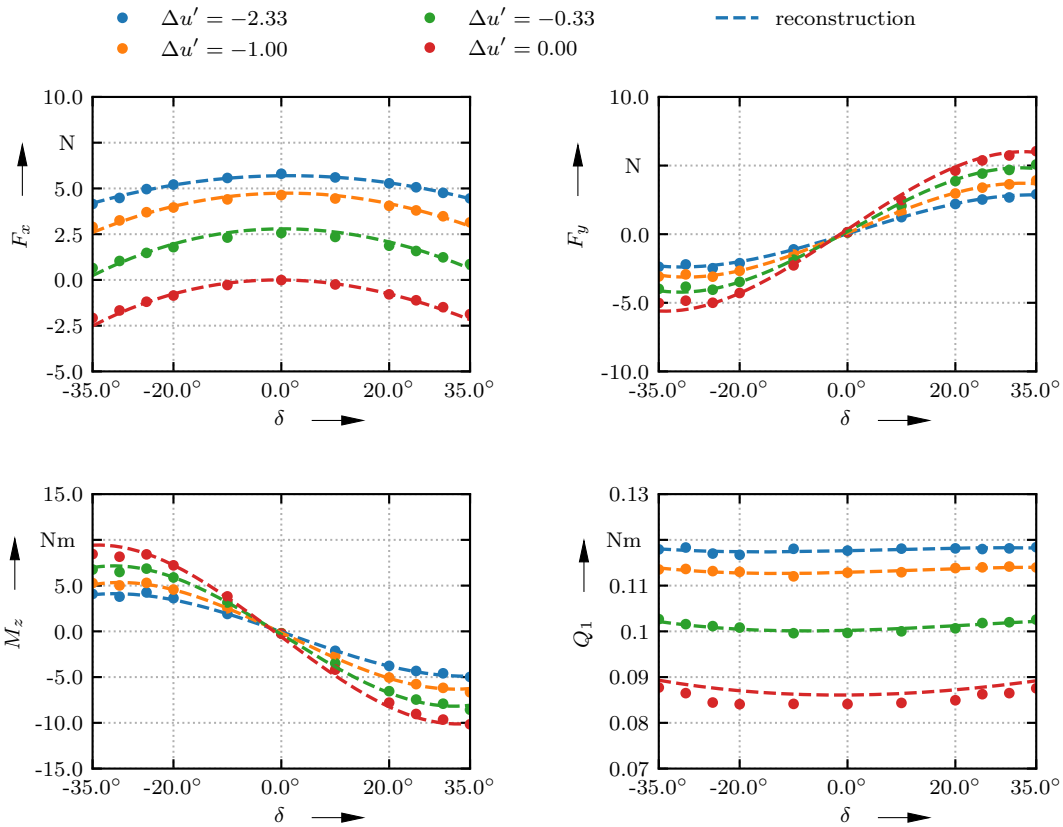

Figure C.6.: Reconstruction of static combined δ-Δu tests

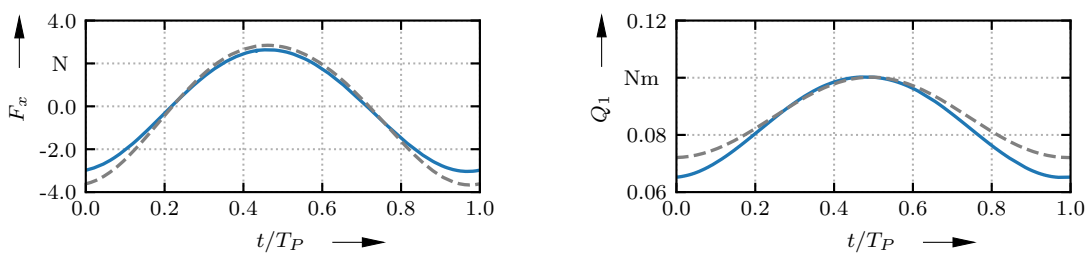

Figure C.7.: Reconstruction of dynamic pure surge test

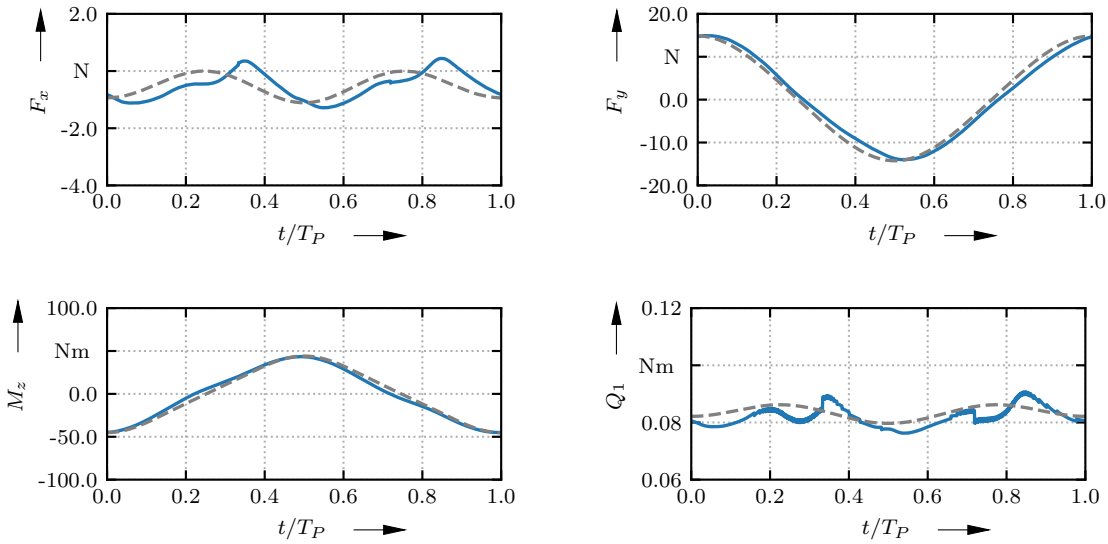

Figure C.8.: Reconstruction of dynamic pure yaw test

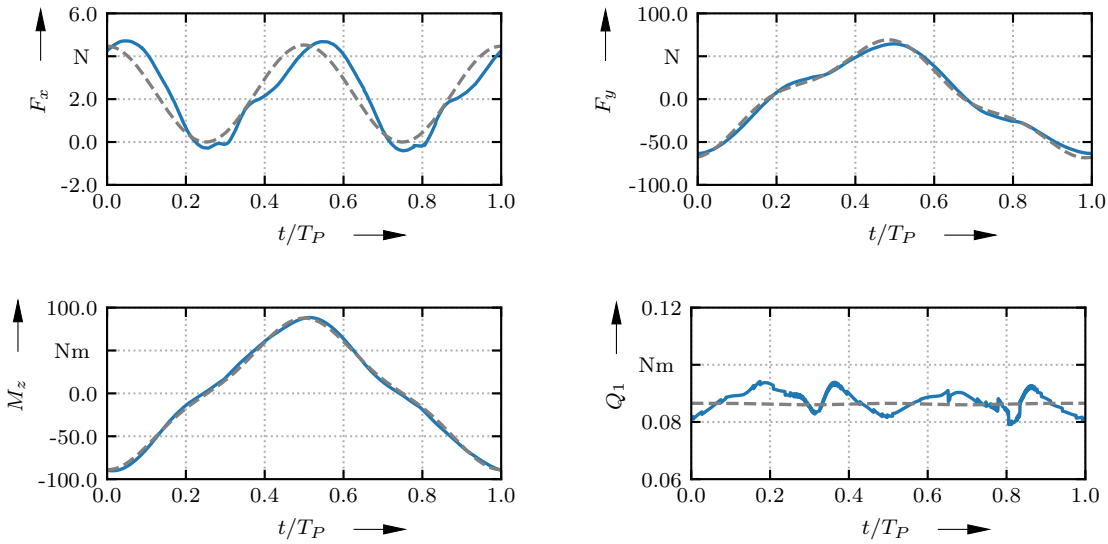

Figure C.9.: Reconstruction of dynamic sway-yaw test

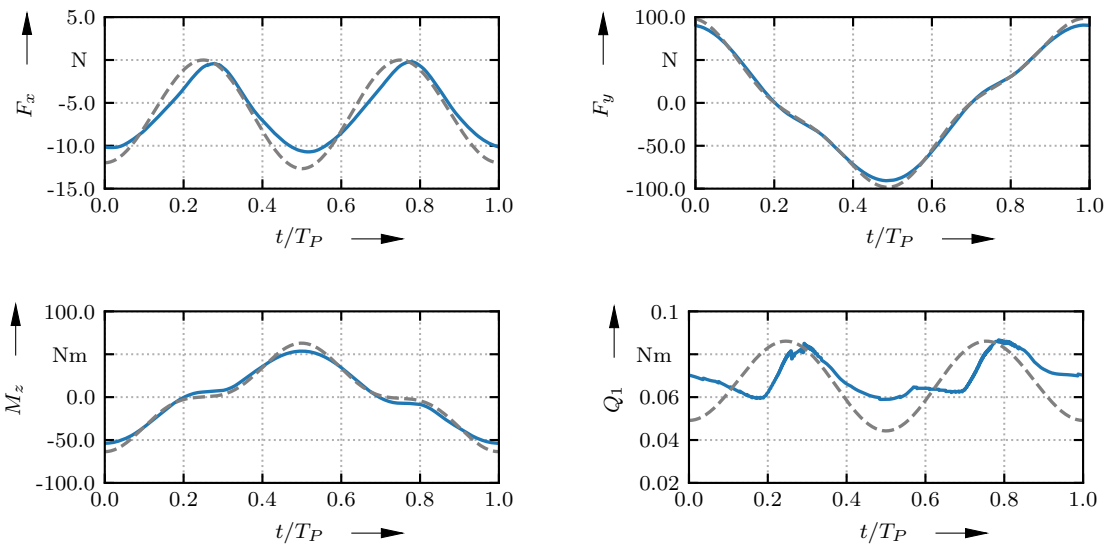

Figure C.10.: Reconstruction of dynamic yaw-sway test